FIELD AND FREQUENCY DEPENDENCE OF THE SURFACE RESISTANCE OF SUPERCONDUCTING MICROWAVE RESONATORS FOR PARTICLE ACCELERATORS

A Dissertation

Presented to the Faculty of the Graduate School

of Cornell University

in Partial Fulfillment of the Requirements for the Degree of

Doctor of Philosophy

by

Peter Nicholas Koufalis

May 2022

FIELD AND FREQUENCY DEPENDENCE OF THE SURFACE RESISTANCE OF SUPERCONDUCTING MICROWAVE RESONATORS FOR PARTICLE ACCELERATORS

Peter Nicholas Koufalis, Ph.D.

Cornell University 2022

For decades, the cutting-edge of niobium superconducting radio-frequency cavities for use in charged particle acceleration was limited to operating frequencies up to 1.5 GHz resulting from the strong frequency dependence of the surface resistance which limited achievable accelerating fields and increased cryogenic power costs to unreasonable levels. Recent advancements such as nitrogen-doping, nitrogen-infusion, and niobium(III)-tin coating of niobium cavities have created an opportunity for the use of smaller, higher frequency cavities by decreasing surface resistance and, therefore, reducing cryogenic costs. Nitrogen-doping and infusion surface treatments introduced an astounding effect called 'Q-rise' where the cavity quality factor increases with increasing accelerating field allowing quality factors to be achieved that were not previously possible. This dissertation will discuss the field dependence of the surface resistance of impurity-infused cavities at fixed frequency (1.3 GHz), the design and commissioning of apparatus to perform electropolishing, high pressure rinsing, and radio-frequency testing of high frequency cavities (3.9 and 5.2 GHz), a model that uses data of the field and frequency dependence of the surface resistance to find the optimal operating field, frequency, and temperature that minimizes cryogenic power load per unit beam energy for accelerator design.

BIOGRAPHICAL SKETCH

Peter Nicholas Koufalis was born and raised in Bethlehem, Pennsylvania. He was first exposed to physics during his last semester attending Liberty High School and instantly became enamored with it. It was at that point that he decided – without hesitation or reserve – to become a physicist. He began this pursuit by studying physics at Kutztown University where he did computational work on the behavior of low-dimensional Bose-Einstein condensates in time-varying potentials, graduating in May 2013. He then moved on to Cornell to start his graduate studies in accelerator physics, completing his Ph.D. in May 2022.

To my parents, Lori and Nick, and my sister and brother-in-law, Kristina and Kyle, who have always supported me. I also dedicate this dissertation to my niece Sophia who made my last year of graduate school particularly special.

ACKNOWLEDGEMENTS

I would like to give thanks to my advisor Matthias Liepe for his constant encouragement, advice, and understanding of the struggles a graduate student goes through during their time as a PhD student. I could not have asked for a better advisor. I would also like to thank my mentors in the SRF group, Dan Gonnella and Daniel Hall, who showed me the ropes in the lab and how to be a practical physicist. I would also like to acknowledge my fellow graduate students James Maniscalco, Ryan Porter, Thomas Oseroff, Neil Stilin, Gabriel Gaitan, Nicole Verboncoeur, and Liana Shpani. Special thanks also goes to the chemists Terri Gruber-Hine and Holly Conklin for the extra-mile help they provided when I needed it, the engineers James Sears for his seemingly limitless knowledge of the lab and Adam Holic for his help and collabaration on the high frequency insert design and many off-topic, after hours discussions, the technicians Greg Kulina and Paul Bishop for always seeming to know a much simpler way of solving problems than I could come up with on my own, John Kaufmann for his skill and knowledge of our vacuum furnace without which would have made my research much more difficult to complete, and all the members of the Newman Lab machine shop, Gregory Abbott, Neal Alexander, Shawn Clark, Randy Miller, and Terry Neiss, for their above-and-beyond knowledge and willingness to help even though I constantly gave them rush jobs. I would also like to acknowledge the support of Tim O'Connell, Peter Quigley, Jessica Turco, Mike Roman, Katerina Malysheva, Monica Wesley, and Kacey Acquilano.

On a personal note, I would also like to give special thanks to my closest friends and acquaintances Nick Maritch, Kailie Tsihlis, Josh Hayes, Hollei Hayes, Alex Kramer, Dana Kramer, Tommy Lyster, Rose Lyster, Kyle Troxell, Dimitris Hoimes, Drew Clark, Brian Banderas, Clinton Watton, Cameron

Lawrence, Juliana Lawrence, Alec Smith, and John Kuan for making the long, frigid Ithaca winters tolerable.

Finally, I would like to mention my undergraduate advisors Kunal Das, Sudarshan Fernando, and Anke Walz for their constant encouragement and inspiring me to become a physicist.

The work shown in this dissertation was supported by:

U.S. NSF Awards PHYS 1416318, PHYS 1734189, and PHYS 1549132

TABLE OF CONTENTS

LIST OF TABLES

LIST OF FIGURES

CHAPTER 1

INTRODUCTION

1.1 Introduction to Accelerators

Particle accelerators are a wonderful invention. They are used to accelerate charged particles such as electrons, protons, or ions to very high energies for a myriad of purposes. Among these are studying the nature and structure of subatomic matter, destroying cancer cells in proton therapy, and transmutation of spent nuclear waste, to name a few [Wan08, YZQ19].

Accelerators use either static or alternating electric fields to accelerate charged particles. The latter case is referred to as a radio-frequency (RF) accelerator. This type of accelerator uses electromagnetic resonant cavities that operate at microwave or radio frequencies to impart energy to the beam [PKH08, Wan08]. Almost all modern high-energy accelerators use RF rather than electrostatic acceleration. This is because electrostatic accelerators, such as the cathode ray tubes found in old television sets, are limited to small energies due to electric breakdown [Wan08]. Radio frequency accelerators do no have this limitation [Wan08, Wie15] and, in theory, can be constructed to produce any beam energy desired given enough time, space, and money.

Essentially, RF accelerators come only in two geometries: linear and circular. The primary difference between a linear accelerator (linac) and a circular accelerator (e.g., synchrotrons) is that a charged particle beam only passes once through the linac but can circulate indefinitely around the latter. This fact is an advantage for circular accelerators since the beam can be accelerated each dur-

ing each orbit. However, they also have the disadvantage of energy loss due to the beam emitting synchrotron radiation as a result of their curved path [Wie15]. This ultimately limits the beam energy as an equilibrium is reached between the energy gained from acceleration and the energy lost to radiation. At the time of publication, the most famous and powerful circular accelerator in the world is the Large Hadron Collider, at which, in 2012, the Higgs boson was discovered [ATL12].

To complicate the matter further, an accelerator may be normal or superconducting. Normal conducting accelerators typically use copper resonant cavities to achieve acceleration whereas superconducting accelerators typically use superconducting niobium cavities, as the name suggests. As the temperature is decreased, a superconductor will suddenly and discontinuously loose all electrical resistance below a specific material-dependent critical temperature for static fields [Tin96]. However, under the presence of RF fields superconductors do have a very small, yet finite resistance. Despite this, the resistance of a typical superconducting cavity is several orders of magnitude smaller than that of an equivalent copper cavity [PKH08]. Because of this, superconducting cavities dissipate far less power than copper cavities and are able to operate continuously at higher accelerating fields which leads to higher beam currents and repetition rates. Furthermore, because of the lower resistance, and therefore, higher quality factor, superconducting cavities require less power to operate at a given accelerating field. A detailed discussion of the advantages of superconducting cavities is given in [PKH08]. The rest of this dissertation concerns itself only with superconducting radio frequency (SRF) cavities and their performance with respect to operating frequency, accelerating field, and surface treatment.

1.2 Organization of this Dissertation

This thesis will introduce the basic theory of superconductivity with a historical approach in Chapter 1 followed by the fundamentals of RF superconductivity required for the remainder of the text in Chapter 2. Cavity fabrication, preparation, and testing will be discussed in Chapter 4. The results of research will be discussed in Chapter 5, 6, and 7. Chapter 5 will cover the field dependence of the surface resistance of low temperature impurity infused 1.3 GHz cavities and associated concentration profiles of impurities obtained through secondary ion mass spectroscopy measurements. Chapter 6 will discuss the design and implementation of the electropolishing, high pressure ringing, and test insert for high frequency cavities (3.9 and 5.2 GHz) as well as the design and electromagnetic simulation results of the forward power coupler for these cavities. Finally, Chapter 7 will contain the discuss a model that optimizes the accelerating field, resonant frequency, and cryogenic bath temperature to minimize the cryogenic power load. This model is based on the experimental data on field and frequency dependence of the surface resistance of cavities ranging in frequency from 650 MHz to 4 GHz.

CHAPTER 2

INTRODUCTION TO SUPERCONDUCTIVITY

In this chapter, the theoretical fundamentals of RF superconductivity will be outlined and summarized. These fundamentals are essential for the understanding of all that follows in this dissertation. First, the two most astounding properties of superconductors will be discussed: perfect conductivity [Onn11] and the Meissner effect [MO33]. The London equations [LL35], the two-fluid model, Ginzburg-Landau theory [GL50], and BCS theory will be discussed next [BCS57, MB58].

2.1 Perfect Conductivity and the Meissner Effect

It was discovered by H. Kamerlingh Onnes in 1911 that mercury, when passing through a critical temperature T_c, suddenly and discontinuously lost all electrical resistance [Onn11]. The implication of this discovery is quite profound: once a constant electric current is set into motion, it will flow indefinitely without an external power source. This is in stark contrast to ordinary metals – such as copper, silver, and gold – which when cooled down to the same temperature will still have a small, finite resistance requiring a voltage bias to maintain steady current [Mat79].

The critical temperatures at which these special metals undergo a phase transition from normal to superconducting is dependent on the metal and its composition. For example, high purity niobium (Nb) will transition at 9.2 K whereas niobium(III)-tin (Nb_3Sn) transitions at 18 K [PKH08].

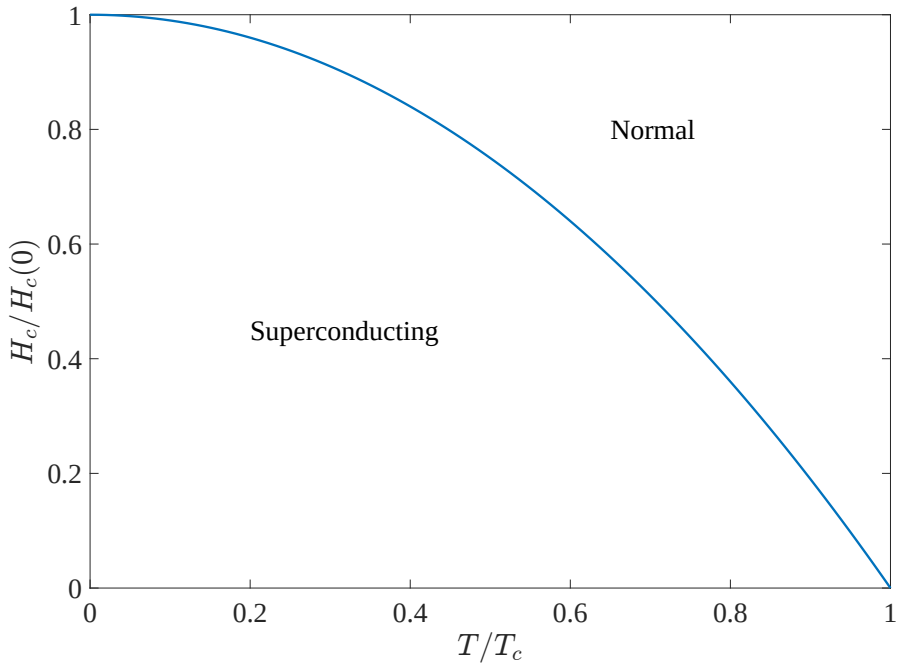

Figure 2.1: The critical magnetic field H_c as a function of temperature in the range $T \leq T_c$ for a type I superconductor. In the region $H < H_c$ the metal is in the superconducting state and for $H > H_c$ the metal is in the normal state. In the case $H = H_c$ the superconducting and normal state are in equilibrium.

When a metal undergoes the transition from normal to superconducting, it actively expels external magnetic fields. Furthermore, if an external magnetic field is applied after the transition, a screening supercurrent is created on the superconducting surface to exactly cancel out the external field within its interior [Tin96]. This behavior is referred to as the Meissner effect after its discovery by Meissner and Ochsenfeld in 1933 [MO33].

There is an energy associated with expelling an external field from the interior of a superconductor due to the external magnetic pressure on the surface of the superconductor. Because of this, there exists a critical field value at which the energy of the normal state is lower than the superconducting state. Above this critical value, the metal transitions to the normal state and the external field enters the volume of the metal [Tin96]. The critical field H_c has a temperature

dependence that is quite accurately describe by the empirical formula [Tin96]

$$H_c(T) = H_c(0)\left[1 - \left(\frac{T}{T_c}\right)^2\right]. \tag{2.1}$$

This temperature dependence is shown in Figure 2.1. This illustrates the two conditions required for the superconducting state to exist: (1) the temperature must be below the critical temperature of the metal and (2) the external magnetic field must not exceed the critical field. Critical magnetic fields are discussed in more detail in the context of the Ginzburg-Landau theory in Section 2.4.

2.2 The London Equations and the Two-Fluid Model

In 1935, F. and H. London proposed a simple model to describe the electric and magnetic fields within a superconductor [LL35]. According to the London model, the electric field and the magnetic flux density are governed by the relations:

$$\mathbf{E} = \left(\frac{m}{n_s e^2}\right)\frac{\partial \mathbf{J}_s}{\partial t} \tag{2.2}$$

$$\mathbf{B} = -\left(\frac{m}{n_s e^2}\right)\nabla \times \mathbf{J}_s \tag{2.3}$$

where n_s is loosely taken to be the superconducting electron density, m the mass of an electron, e the electron charge, and $\mathbf{J}_s$ the supercurrent density. Equation 2.2 dictates that a constant electric field will cause the supercurrent to increase with time. In other words, the presence of an electric field accelerates the superconducting electrons. This is in contrast to a normal metal where a constant electric field will result in a constant current and, therefore, the average electron velocity is also constant. Thus, Equation 2.2 describes the property of perfect conductivity.

The second of the London equations describes the Meissner effect. To see why this is so, a substitution of Ampere's law ($\nabla \times \mathbf{B} = \mu_0 \mathbf{J}$) into Equation 2.3 and a clever use of vector identities can be used to arrive at the following relation

$$\nabla^2 \mathbf{B} = \frac{1}{\lambda_{\mathrm{L}}^2} \mathbf{B} \tag{2.4}$$

where $\lambda_{\mathrm{L}} = (m/\mu_0 n_s e^2)^{1/2}$ is known as the London penetration depth [Tin96]. Equation 2.4 shows that the magnetic field decays exponentially, with characteristic length λ_{L}, into the bulk. The temperature dependence of the penetration depth is found to closely follow the empirical expression [Tin96]

$$\lambda_{\mathrm{L}}(T) = \lambda_L(0) \left[1 - \left(\frac{T}{T_c} \right)^4 \right]^{-1/2} . \tag{2.5}$$

Both London equations can be combined into a single relation to describe the dependence of the supercurrent density on the vector potential $\mathbf{A}$ instead of the electric and magnetic fields:

$$\mathbf{J}_s = -\frac{n_s e^2}{m} \mathbf{A} = -\frac{1}{\mu_0 \lambda_{\mathrm{L}}^2} \mathbf{A}. \tag{2.6}$$

To uniquely determine the potential, the London gauge ($\nabla \cdot \mathbf{A} = 0$) is used, $\mathbf{A} \to 0$ in the bulk, and $\mathbf{A} \cdot \mathbf{n} = 0$ where $\mathbf{n}$ is the unit vector normal to the surface of the superconductor [Tin96].

It should be noted that the London model employs local electrodynamics (i.e. the current density depends only on the value of the potential at that point). It should also be noted that λ_{L} is used to denote the theoretical limiting value of a pure superconductor in the case of local electrodynamics whereas λ is used to denote the empirically determined value for imperfect, real-world superconductors where the assumption of material purity and local dynamics is not applicable. The case of nonlocal electrodynamics is discussed in the next section.

2.3 Pippard's Nonlocal Electrodynamics

A. B. Pippard constructed a theory of nonlocal electrodynamics to generalize the London model in 1953 [Pip53]. The justification behind the modification is based on Heisenberg's uncertainty principle [Pip53, Tin96]. He argued that electrons near the Fermi surface in the vicinity of T_c (i.e., energies within $\sim k_B T_c$ of E_F) have momenta spread $\Delta p \sim k_B T_c / v_F$ where E_F and v_F are the Fermi energy and velocity, respectively. According to the uncertainty principle, $\Delta x \sim \hbar/\Delta p \sim \hbar v_F / k_B T_c$. Thus, the spatial extent of the superconducting wavefunction must be on the order of $\xi_0 \sim \hbar v_F / k_B T_c$ where ξ_0 is referred to as the Pippard coherence length. Sometimes the coherence length is written in the form:

$$\xi_0 = a \frac{\hbar v_F}{k_B T_c} \tag{2.7}$$

where a is a numerical constant close to unity [Tin96].

Pippard took this coherence length and proposed an integral expression for the supercurrent density

$$\mathbf{J}_s(\mathbf{r}) = -\frac{3}{4\pi\mu_0 \lambda_L^2 \xi_0} \int \frac{\mathbf{R}[\mathbf{R} \cdot \mathbf{A}(\mathbf{r}')]}{R^4} e^{-R/\xi} \, d^3\mathbf{r}' \tag{2.8}$$

where $\mathbf{R} = \mathbf{r} - \mathbf{r}'$ and the (un)primed coordinate is the (observation) source point. Simply put, the current density at a point $\mathbf{r}$ depends on the potential at all points $\mathbf{r}'$ within a small sphere of radius ξ centered about $\mathbf{r}$. Note that this equation intrinsically includes normal conducting electron scattering in the exponential term. This is because ξ is taken to be the effective coherence length due to scattering (i.e., the electron mean free path ℓ is finite). In the case of a perfect crystal with no imperfections or scattering sites, ξ_0 would be used instead of ξ. The 'dirty' coherence length is related to the 'clean' coherence length by

[Pip53]

$$\frac{1}{\xi} = \frac{1}{\xi_0} + \frac{1}{\ell}. \tag{2.9}$$

Similary, the effective penetration depth is also altered by scattering and is well approximated by the expression [Tin96]

$$\lambda = \lambda_{\mathrm{L}} \left(1 + \frac{\xi_0}{\ell}\right)^{1/2}. \tag{2.10}$$

With the mean free path ℓ, coherence length ξ, and penetration depth λ now defined, it is important to mention two important regimes. In the clean limit ($\ell \gg \xi_0$), ξ and λ reduce to ξ_0 and λ_{L}, respectively. In the dirty limit ($\ell \ll \xi_0$), $\ell \ll \lambda$ and $\xi \approx \ell$. These regimes will be relevant later on.

2.4 The Ginzburg-Landau Theory

The next step in the development of the understanding of superconductivity came from V. L. Ginzburg and L. D. Landau in 1950 in the form of their phenomenological theory of superconductivity [GL50]. The success of the GL theory was its ability to describe macroscopic properties of superconductors using intuitive thermodynamic arguments.

The theory begins with a complex order parameter $\psi(\mathbf{r})$ which can be interpreted to be proportional to the superconducting electron density, $n_s \propto |\psi(\mathbf{r})|^2$. Assuming $\psi(\mathbf{r})$ is small and varies slowly in space, Ginzburg and Landau showed that the free energy density f_s of a superconductor in the vicinity of T_c could be approximated via a series expansion

$$f_s = f_n + \alpha|\psi|^2 + \frac{1}{2}\beta|\psi|^2 + \frac{1}{2m}|(-i\hbar\nabla - 2e\mathbf{A})\psi|^2 + \frac{\mu_0 H_a^2}{2} \tag{2.11}$$

where f_n is the normal state free energy density, α and β are dimensionless parameters, and H_a is the externally applied magnetic field. In the absence of external fields and ignoring the kinetic term, the free energy difference takes the form

$$f_s - f_n = \alpha|\psi|^2 + \frac{1}{2}\beta|\psi|^4. \tag{2.12}$$

This approximate form only remains valid for small $|\psi|$ (i.e., $T \sim T_c$) and, therefore, β must be positive (otherwise the parabolic shape of $f_s - f_n$ would open downwards and the minima of the free energy would be undefined). Consequently, when $T \rightarrow T_c$ from above, α must switch from positive to negative (i.e., from the normal conducting to superconducting state). When $\alpha < 0$, the minimum in the free energy occurs at the value

$$|\psi|^2 = |\psi_\infty|^2 = -\frac{\alpha}{\beta} \tag{2.13}$$

where ψ_∞ is the value deep in the bulk where all external fields are effectively screened out. Substitution of Equation 2.13 into Equation 2.12 and the definition of the thermodynamic critical magnetic field H_c [Tin96] yields an expression for the minimum value of the free energy

$$(f_s - f_n)_{min} = -\frac{\alpha^2}{2\beta} = -\frac{\mu_0 H_c^2}{2}. \tag{2.14}$$

From the Ginzburg-Landau theory, expressions for the penetration depth λ_{GL} and coherence length ξ_{GL} can be derived [Tin96] although the explicit derivation will be omitted here. The subscripts are present to differentiate them from the values derived from the London's two-fluid model and, later, the BCS theory. The Ginzburg-Landau penetration depth and coherence length in terms of the dimensionless parameters α and β are given by [GL50, Tin96]

$$\lambda_{\mathrm{GL}} = \sqrt{\frac{m\beta}{2\mu_0 e^2|\alpha|}} \tag{2.15}$$

and

$$\xi_{\mathrm{GL}} = \sqrt{\frac{\hbar^2}{4m|\alpha|}}, \tag{2.16}$$

respectively, where m is the electron mass. The coherence length can be expressed in a more explicit form involving the flux quantum $\Phi_0 = h/2e$, H_c and λ_{GL} as shown below:

$$\xi_{\mathrm{GL}} = \frac{\Phi_0}{2\sqrt{2}\pi\mu_0 H_c \lambda_{\mathrm{GL}}}. \tag{2.17}$$

It is here that the famous Ginzburg-Landau parameter κ is introduced. This dimensionless parameter is defined as

$$\kappa \equiv \frac{\lambda_{\mathrm{GL}}}{\xi_{\mathrm{GL}}} = \frac{2\sqrt{2}\pi\mu_0 H_c \lambda_{\mathrm{GL}}^2}{\Phi_0} \tag{2.18}$$

This parameter defines two distinct types of superconductors separated by the value $\kappa = 1/\sqrt{2}$. Superconductors for which $\kappa < 1/\sqrt{2}$ are known as type I and for $\kappa > 1/\sqrt{2}$ they are known as type II.

2.4.1 Type I and II Superconductors

Type I superconductors have a positive surface energy at the boundary between superconducting and normal conducting regions [Tin96, PKH08]. This means that no magnetic flux can enter the superconducting regions until the applied field $H_a = H_c$. In general, the geometry of the superconductor is important and can cause enhancements of the field in certain regions. For example, consider a spherical superconductor in a uniformly applied magnetic field pointing in the z-direction. Because of the way the sphere expels the magnetic flux, the field at the equator of the sphere will be $H_{\mathrm{eq}} = (3/2)H_a$ [Tin96]. Thus, when $H_a = (2/3)H_c$, the field at the equator $H_{\mathrm{eq}} = H_c$. As the applied field strength increases further, the field at the equator grows in strength and more of the

sphere becomes normal conducting. However, the superconducting state won't be completely destroyed until $H = H_c$ everywhere inside the sphere. Type I superconductors will not be mentioned beyond this point since this dissertation concerns itself only with the type II category.

Type II superconductors, on the other hand, have a negative surface energy at the normal-superconducting boundary resulting in dramatically different behavior [Tin96, PKH08]. Superconductors of this variety have two critical fields H_{c1} and H_{c2}. The former is the field at which it is more energetically favorable for magnetic flux to coexist within the superconductor rather than being expelled [Tin96, PKH08]. However, for magnetic flux lines that exist entirely outside the superconductor there is an energy barrier that it must first overcome to enter the superconductor. This is known as the superheating field H_{sh} above which magnetic vortices can enter the superconductor from its exterior. As the field strength increases and evenetually exceeds H_{c2}, the superconducting state is completely destroyed. This point is known as the upper critical field H_{c2} [Tin96, PKH08].

In the context of the Ginzburg-Landau theory, the lower and upper critical fields are given by [GL50]

$$H_{c1} = \frac{\Phi_0}{4\pi\mu_0\lambda_{GL}^2}\ln\kappa = \frac{H_c}{\sqrt{2}\kappa}\ln\kappa \tag{2.19}$$

and

$$H_{c2} = \frac{\Phi_0}{2\pi\mu_0\xi_{GL}^2} = \sqrt{2}\kappa H_c. \tag{2.20}$$

It should be clear from Equation 2.20 that for $\kappa > 1/\sqrt{2}$ the upper critical field $H_{c2} > H_c$ and the superconductor is type II. Otherwise, the nonphysical result $H_{c1} > H_c > H_{c2}$ arises and, therefore, the superconductor must be type I with only one critical field, H_c.

2.5 The BCS Theory

In 1957, Bardeen, Cooper, and Schrieffer presented the first microscopic theory of superconductivity [BCS57]. The theory introduced the concept of Cooper pairs where two electrons of equal and opposite momenta and spin ($\mathbf{k}\uparrow, -\mathbf{k}\downarrow$) would form a single composite boson via a weak attractive potential mediated by electron-phonon interactions [BCS57, Tin96, PKH08]. Cooper pairs obey Bose-Einstein statistics allowing them to occupy the ground state simultaneously leading to the observed macroscopic superconducting state.

A consequence of the BCS theory is the alteration of the electron density of states such that an energy gap appears at the Fermi level as the conductor passes through the superconducting transition. The BCS theory predicts an energy gap E_g at $T = 0$ that is on the order of $k_B T_c$

$$E_g = 2\Delta(0) = 3.528 k_B T_c \tag{2.21}$$

where k_B is Boltzmann's constant [BCS57]. Rewriting the above in terms of the gap parameter $\Delta(0)$ yields

$$\frac{\Delta(0)}{k_B T_c} = 1.764 \tag{2.22}$$

Notice that this value is independent of material in the theory but in practice may depend on factors such as material, impurity composition, and field strength. The gap parameter approximately follows the temperature dependence given by [BCS57, Tin96]

$$\frac{\Delta(T)}{\Delta(0)} \approx \left[\cos\left(\frac{\pi t^2}{2}\right)\right]^{1/2} \tag{2.23}$$

where $t = T/T_c$ and remains relatively constant (i.e., $\Delta(T) \approx \Delta(0)$) for $T < 0.5T_c$ but drops rapidly to zero at as $T \to T_c$. Physically, the energy gap 2Δ is the

energy required to break a Cooper pair. The density of electrons above the gap (i.e., quasiparticles excitations) follows an exponential dependence on the energy gap [Tin96]

$$n_n \propto \exp\left(-\frac{\Delta(T)}{k_B T_c}\right). \tag{2.24}$$

Thus, as $T \to T_c$ the energy gap $\Delta(T) \to 0$, $n_s \to 0$, and $n_n \to n$ where n is the electron density of the normal state.

CHAPTER 3

RADIO FREQUENCY SUPERCONDUCTIVITY

The field of RF superconductivity concerns itself with oscillating electric and magnetic fields in superconducting resonant cavities. An illustrative example is the cylindrical pillbox cavity since the fields can be solved for analytically. For more complicated cavities geometries, such as the elliptical design used throughout this dissertation, the fields must be calculated numerically with electromagnetic simulation software. This chapter will discuss the fundamentals of radio-frequency superconductivity relevant for superconducting accelerator cavities.

3.1 The Cylindrical Pillbox Cavity

Consider a cylindrical cavity of radius R and length L. For the fundamental transverse magnetic mode TM_{010} (i.e., the mode used in accelerator cavities), the electric field is purely in the longitudinal z-direction and the magnetic field

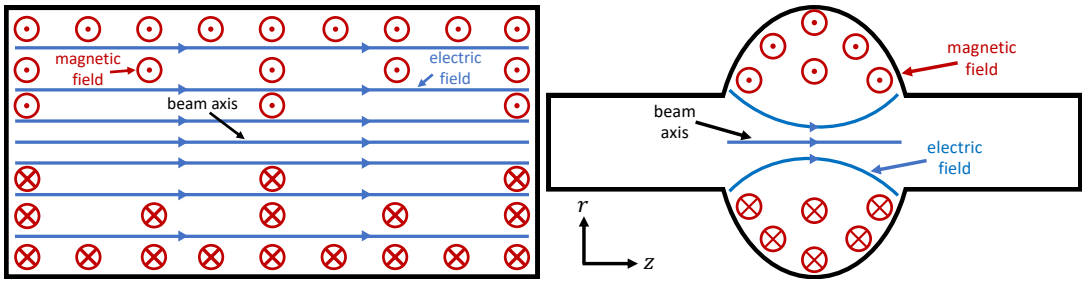

Figure 3.1: Electric and magnetic field configuration for the TM_{010} for a cylindrical pillbox cavity (left) and and elliptical cavity (right). The circle and dot points out of the page and the circle and cross points into the page.

entirely in the azimuthal ϕ-direction with fields given by

$$E_z = E_0 J_0\left(\frac{2.405r}{R}\right)e^{-i\omega t} \quad \text{and} \quad H_\phi = -i\frac{E_0}{\eta}J_1\left(\frac{2.405r}{R}\right)e^{-i\omega t} \tag{3.1}$$

where E_0 is the amplitude of the electric field, J_0 and J_1 are the zeroth and first order Bessel functions of the first kind, respectively, r is the radial distance from the origin, ω is the angular resonant frequency of the fields, and $\eta = \sqrt{\epsilon_0/\mu_0}$ is the impedance of free space [PKH08]. The field configuration for a pillbox and an elliptical cavity is shown in Figure 3.1

The TM_{010} mode is preferable for accelerator cavities because it maximizes the electric field along the beam axis ($r = 0$). Charged particles moving along the beam axis gain energy from the electric field as they pass through the cavity. Most higher-order modes typically do not have an electric field along the beam axis or, if they do, have a higher resonant frequency making them less desirable for use in an accelerators [PKH08].

The elliptical cavity geometries used through this dissertation are similar enough to a cylindrical pillbox cavity that qualitative features of the fields are the same. That is, along the beam axis, the electric field points only in the direction of the beam and the magnetic field is entirely transverse. This leads directly to the concept of accelerating gradient which is proportional to the amount of energy a charged particle will gain as it passes through a cavity.

3.2 Accelerating Gradient

The accelerating gradient E_{acc} is the highest possible average electric field that a charged particle would 'see' as it travels through the cell of a cavity over a half

RF period. In other words, E_{acc} can be expressed in terms of the average voltage across the cavity cell, V_{acc}, along the beam axis and the length of the cell, d, as [PKH08]

$$E_{\text{acc}} = \frac{V_{\text{acc}}}{d}. \tag{3.2}$$

The accelerating voltage is calculated by integrating the longitudinal component of the electric field as seen by the particle over the cell length [PKH08]:

$$V_{\text{acc}} = \left| \int_0^d E_z(r = 0, z) e^{i\omega z/c} \, dz \right|. \tag{3.3}$$

Thus, the maximum possible energy gained, $\mathcal{E}_{\text{max}}$, by a particle of charge e, is the product of the charge and voltage:

$$\mathcal{E}_{\text{max}} = eV_{\text{acc}} = eE_{\text{acc}}d. \tag{3.4}$$

The accelerating gradient tells only a part of the story. One must also know the performance of the cavity to evaluate the quality of its geometrical design and surface preparation method. This leads to the discussion of surface impedance and quality factor.

3.3 Surface Impedance

The surface impedance Z of a cavity's walls in terms of the normal and superconducting components of the conductivity, σ_n and σ_s, respectively, is

$$Z = \sqrt{\frac{i\mu_0\omega}{\sigma_n - i\sigma_s}} \tag{3.5}$$

where ω is the frequency of the applied field and μ_0 is the permeability of free space [MB58, THS91, Gur17]. Breaking this into real and imaginary components

yields a complicated expression which can be simplified by the assumption that $\sigma_n \ll \sigma_s$ and a clever use of a series expansion to arrive at [Gur17]

$$Z = \frac{\mu_0 \omega \sigma_n}{2\sigma_s^2} \sqrt{\frac{\sigma_s}{\mu_0 \omega}} + i \sqrt{\frac{\mu_0 \omega}{\sigma_s}}. \tag{3.6}$$

The conductivity of the superconducting state can be derived from the first London equation [THS91, PKH08, Gur17]:

$$\sigma_s = \frac{1}{\mu_0 \omega \lambda_{\mathrm{L}}^2}. \tag{3.7}$$

Substituting this expression back into Equation 3.6 yields

$$Z = \frac{1}{2} \mu_0^2 \omega^2 \lambda_{\mathrm{L}}^3 \sigma_n + i \mu_0 \omega \lambda_{\mathrm{L}}. \tag{3.8}$$

The real component of Z is the dissipative surface resistance, R_S, and the imaginary component is the non-dissipative reactance, X_S. The dissipative nature of R_S arises from losses due to the normal component of the current in the superconductor. The reactance is due to the motion of the supercurrent that screens out external fields.

To find a more useful form for R_S, an explicit expression for $\sigma_n(\omega, T)$ must be derived. A nice discussion of this derivation is given in the work of Gurevich [Gur17] and the result is reproduced below:

$$\frac{\sigma_n}{\sigma_{n,0}} = \frac{4\Delta}{\hbar\omega} \sinh\left[\frac{\hbar\omega}{2k_B T}\right] K_0\left[\frac{\hbar\omega}{2k_B T}\right] e^{-\Delta/k_B T}. \tag{3.9}$$

Here, $\sigma_{n,0}$ is the residual conductivity of the normal state at $T \approx 0$, and K_0 is the zeroth order modified Bessel function of the second kind. Since $\hbar\omega/2k_B T \ll 1$ for the frequencies ($f < 8$ GHz) and temperatures ($T < 0.5T_c$) of interest, the Bessel function in Equation 3.9 can be approximated by

$$K_0\left[\frac{\hbar\omega}{2k_B T}\right] \approx \ln\left[\frac{4k_B T}{\hbar\omega}\right] - C \tag{3.10}$$

where C is Euler's constant [Gur17]. The small angle approximation $\sinh(x) \approx x$ allows for further simplification and, upon substitution into the formula for the surface resistance, results in

$$R_S = \frac{\mu_0^2 \omega^2 \lambda_{\mathrm{L}}^3 \Delta}{\rho_{n,0} k_B T} \ln\left[\frac{C_1 k_B T}{\hbar \omega}\right] e^{-\Delta/k_B T} \tag{3.11}$$

where $C_1 = 4/e^C$ and $\rho_{n,0} = 1/\sigma_{n,0}$ [Gur17]. Grouping of terms to simplify the expression further yields

$$R_S = A\left(\frac{1}{T}\right)\omega^2 e^{-\Delta/k_B T} \tag{3.12}$$

where the prefactor A is given by

$$A = \frac{\mu_0^2 \lambda_L^3 \Delta}{\rho_{n,0} k_B} \ln\left[\frac{C_1 k_B T}{\hbar \omega}\right]. \tag{3.13}$$

Empirically, the surface resistance is often written in terms of the temperature-dependent BCS component, R_{BCS}, and the temperature-independent residual resistance, R_{res}, as

$$R_S(E_{\mathrm{acc}}, T) = R_{\mathrm{BCS}}(E_{\mathrm{acc}}, T) + R_{\mathrm{res}}(E_{\mathrm{acc}}) \tag{3.14}$$

where R_{BCS} is given by Equation 3.12 and R_{res} is dependent on intrinsic properties of the superconducting material such as losses due to motion of trapped magnetic flux vortices, lossy oxides, or metallic hydrides within the penetration layer of the superconductor [PKH08, Gur17]. Once R_S is known, the power dissipated by the cavity can be calculated and, from that, the quality factor can be defined. This is discussed in the following section.

3.4 Quality Factor

One of the most important quantities when it comes to accelerator cavities is the intrinsic quality factor Q_0 [PKH08]. The quality factor is related to the power

dissipated by the cavity P_{diss}, the cavity resonance frequency ω_0, and the energy stored in the fields U. Qualitatively, Q_0 is proportional to the number of RF cycles it takes for the cavity to dissipate the energy stored in the fields and is a measure of cavity efficiency. Surface treatments are typically designed around increasing Q_0 to the highest achievable values. By definition, Q_0 is given by [PKH08]

$$Q_0 = \frac{\omega_0 U}{P_{\text{diss}}}. \tag{3.15}$$

The dissipated power depends only on the surface resistance and the amplitude of the applied field

$$P_{\text{diss}} = \frac{1}{2} R_S \int |\mathbf{H}|^2 \, dA \tag{3.16}$$

where it has been assumed that R_S is field-independent and constant over the interior cavity surface and the integral is taken over the surface area of the cavity [PKH08]. The electromagnetic energy stored in the cavity fields is given by

$$U = \frac{1}{2} \mu_0 \int |\mathbf{H}|^2 \, dV \tag{3.17}$$

where the integral is taken over the cavity vacuum volume [PKH08]. Substitution of Equation 3.16 and 3.17 into the expression for the Q_0 yields

$$Q_0 = \frac{\omega_0 \mu_0 \int |\mathbf{H}|^2 \, dV}{R_S \int |\mathbf{H}|^2 \, dA}. \tag{3.18}$$

This can be simplified further by writing

$$Q_0 = \frac{G}{R_S} \tag{3.19}$$

where G is known as the geometry factor and is defined as

$$G = \frac{\omega_0 \mu_0 \int |\mathbf{H}|^2 \, dV}{\int |\mathbf{H}|^2 \, dA}. \tag{3.20}$$

The geometry factor depends only on cavity geometry but not its size, hence the name. Therefore, the linear dimensions of a specific cavity geometry can be scaled by a constant factor and G will remain unchanged.

Table 3.1: Figures of Merit for Cavity Geometries Used in this Dissertation

Parameter	**LTE**	**STE**	**CTE**	**QTE**	**FLC**[1]
f [GHz]	1.3	2.6	3.9	5.2	1.3
G [Ω]	278	278	278	278	278
E_{pk}/E_{acc}	1.86	1.86	1.86	1.86	1.88
B_{pk}/E_{acc} [mT/MVm^{-}1]	4.23	4.23	4.23	4.23	4.28
$E_{pk}/\sqrt{U}$ [MVm^{-1}/J$^{1/2}$]	15.1	42.3	78.5	123.7	15.1
R_{sh}/Q_0 [Ω]	105	105	105	105	105

[1] The FLC cavities are the only ones listed in the table with a slightly different geometry. The TE series of cavities differ only in their linear dimensions.

3.5 Figures of Merit

There are other figures of merit besides G that are important for characterizing different cavity geometries. Among them are the ratio of the peak surface electric field to the accelerating field $E_{\mathrm{pk}}/E_{\mathrm{acc}}$, the peak surface magnetic field to the accelerating field $B_{\mathrm{pk}}/E_{\mathrm{acc}}$, the ratio of the shunt impedance to the quality factor R_{sh}/Q_0, and finally the ratio of the peak surface electric field to the energy stored in the cavity field $E_{pk}/\sqrt{U}$. These values are dependent only on cavity geometry and are determined through computational finite element analysis methods. These parameters are used when calculating E_{acc}, R_S, and Q_0 from raw RF power measurements. The values of the figures of merit for the cavity geometries used in this dissertation are summarized in Table 3.1. All cavities listed in the table are single-cell elliptical cavities of the slightly modified TESLA geometry [ABB^{+}00].

In accelerator physics, the shunt impedance is defined as the ratio of accel-

Table 3.2: Typical Material Parameters for Pure Niobium and Stoichiometric Nb_3Sn

Material Parameter[1]	**Niobium**[2]	**Nb_3Sn**[3]
Critical Temperature, T_c [K]	9.2	18
Normalized Energy Gap, Δ/k_BT_c	1.8	2.2
Penetration Depth, λ [nm]	39	89
Coherence Length, ξ [nm]	38	11
Superheating Field, B_{sh} [mT]	220	420

[1] These are typical values and estimates shown primarily to highlight the differences between Nb and Nb_3Sn and will depend on material purity and surface preparation
[2] Sources: [NM75, Kit05, Lia17]
[3] Sources: [Kit05, God06, Lia17]

erating voltage to the power dissipated by the cavity [PKH08]

$$R_{sh} = \frac{V_{\text{acc}}^2}{P_{\text{diss}}}. \tag{3.21}$$

Cavities are typically designed with a geometry that maximizes R_{sh} so that for a given V_{acc} the dissipated power is minimized. Rearrangement and substitution of Equation 3.15 into the above expression yields an expression for the shunt impedance that does not depend on surface resistance (i.e., material independent) but only on geometry like the other figures of merit mentioned so far:

$$\frac{R_{sh}}{Q_0} = \frac{V_{\text{acc}}^2}{\omega_0 U}. \tag{3.22}$$

This follows from the fact that the voltage scales linearly with the cavity cell length, frequency scales inversely with the cavity's linear dimensions, and the stored energy is proportional to the the cavity volume [PKH08].

Lastly, it is important to mention the relevant material properties for niobium and their typical values and the values for niobium(III)-tin for comparison. The relevant material parameters include the critical temperature T_c, nor-

malized energy gap $\Delta(0)/k_B T_c$, penetration depth λ, coherence length ξ, and superheating field B_{sh}. These values are summarized in Table 3.2. The values of λ and ξ for niobium shown in Table 3.2 are for clean niobium (i.e., $\lambda = \lambda_L$ and $\xi = \xi_0$). All other parameters listed are generally dependent on surface preparation and material purity.

CHAPTER 4

CAVITY FABRICATION, PREPARATION, AND TESTING

This chapter will discuss the life-cycle of the niobium cavities used throughout this dissertation beginning with cavity fabrication, followed by chemical etching and polishing of the cavity post fabrication, surface treatments achieved through baking in an ultra-high vacuum furnace, cleaning of the cavity vacuum surface and assembly onto a test insert used to run RF experiments, and finally the RF measurement process.

4.1 Cavity Fabrication

The single-cell cavities start out as 3 mm thick niobium sheets. Cavity half cells and beam tubes are deep drawn from high purity (RRR = 300) niobium. Beam tube flanges are machined from reactor grade niobium. After the machining of the individual components is complete, the parts are taken to the chemistry room where they receive a light (1 to 2 min) buffer chemical polish (BCP) using a 1:1:2 volume ratio of 48% HF, 70% HNO_3, and 85% H_3PO_4 acid solution. The half cells, beam tubes, and flanges are then welded together via electron beam welding. Finally, an optional round of additional BCP is done, followed by a heavy electropolish (EP) of the interior surface of the cavity to remove approximately 100 to 150 μm from the surface to remove any imperfections and inclusions introduced by the fabrication process.

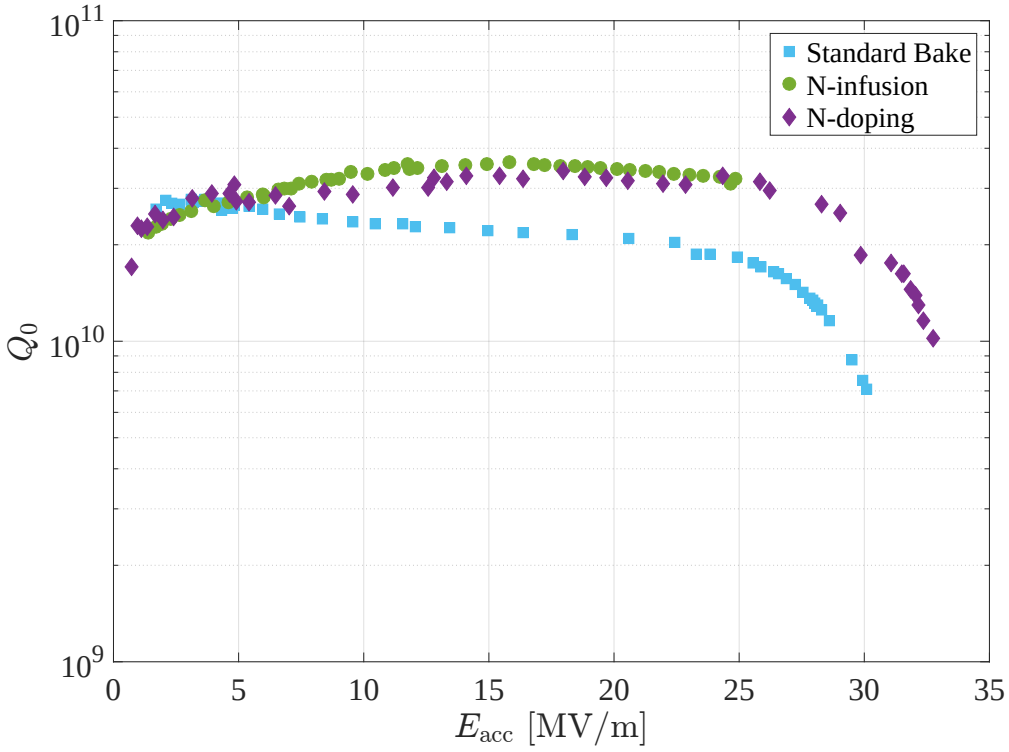

Figure 4.1: Quality factor, Q_0, as a function of accelerating gradient, E_{acc}, at 2.0 K for 1.3 GHz cavities treated with the standard bake, nitrogen infusion, and nitrogen doping.

4.2 Surface Preparation

Following the post-fabrication EP, the cavities are taken to an ultra-high vacuum furnace to be baked. There are four different bake recipes used throughout this dissertation: the standard bake, a variation of the standard bake called the low temperature bake, nitrogen infusion, and nitrogen doping. The details of each recipe are discussed in the following sections. Examples of quality factor measurements as a function of field for 1.3 GHz cavities at 2.0 K are shown in Figure 4.1 for the standard bake, nitrogen infusion, and nitrogen doping.

4.2.1 The Standard Bake

The standard bake is the most simple of the four surface preparations. It involves an 800 °C ultra-high vacuum bake that serves to degas the predominately interstitial hydrogen [PKH08] accumulated during the post-fabrication BCP and EP steps. This bake typically lasts from 3 to 5 hours. After the bake has ended and the furnace has cooled down to 20 °C, it is vented with an ultra-high purity nitrogen-oxygen gas mixture to allow a clean oxide layer to regrow on the surface. The cavity is then removed from the furnace and moved directly into a portable clean room where is it bagged and either taken to the chemistry room for a final EP ($\lesssim$ 5 μm) or to the Class 100 cleanroom to be prepared and assembled for testing.

There is a variation of the standard bake called the low temperature bake. In this variation, the cavity is either removed from the furnace to receive a light EP ($\lesssim$ 5 μm) and sent back into the furnace for a 48 hr ultra-high vacuum bake at 120 °C or it is baked for this time and temperature after the furnace has been vented and the oxide has regrown. In either case, the 120 °C bake causes the oxide layer on the surface to break up and the oxygen to diffuse into the niobium surface. Cavities baked this way tend to reach higher accelerating gradients than standard bake cavities since they do not suffer from the so-called 'high-field Q-slope' (HFQS) that is common in standard baked cavities [VCC98, Kne00].

4.2.2 Nitrogen Infusion

Nitrogen infusion was first discovered at Fermi National Accelerator Laboratory (Fermilab) by Grassellino *et al.* [Gra17] is called so to differentiate it from nitrogen doping which is done at much higher temperatures than infusion. The infusion moniker refers to the diffusion of interstitial nitrogen and other light elements such as oxygen and carbon into the niobium surface by tens of nm which serves to lower the electron mean free path within the penetration depth [Gra17, Man20]. This results in the effect referred to as 'anti-Q-slope' which is an increase in Q_0 with increasing E_{acc}. This anti-Q-slope behavior can be seen in Figure 4.1. There are several theories that attempt to explain the cause of this effect, but there is no definitive explanation at this point [Gur14, Lec21, Kub19].

The bake itself begins at 800 °C in ultra-high vacuum for 3 to 5 hours. The furnace is cooled down to 160 °C while still under vacuum and sits for 3 hours to allow the cavity temperature to equilibrate. A light atmosphere of nitrogen (20 – 40 mTorr) for times ranging anywhere from 12 to 168 hr is then introduced into the furnace. Optionally, the nitrogen atmosphere can be pumped out after the infusion step and the cavity vacuum annealed at the same temperature for 12 to 48 hr. The same venting and removal procedure from the standard bake is used to remove the cavity from the furnace once the bake is complete. The cavity is then bagged and taken to the Class 100 cleanroom to be cleaned and assembled for testing.

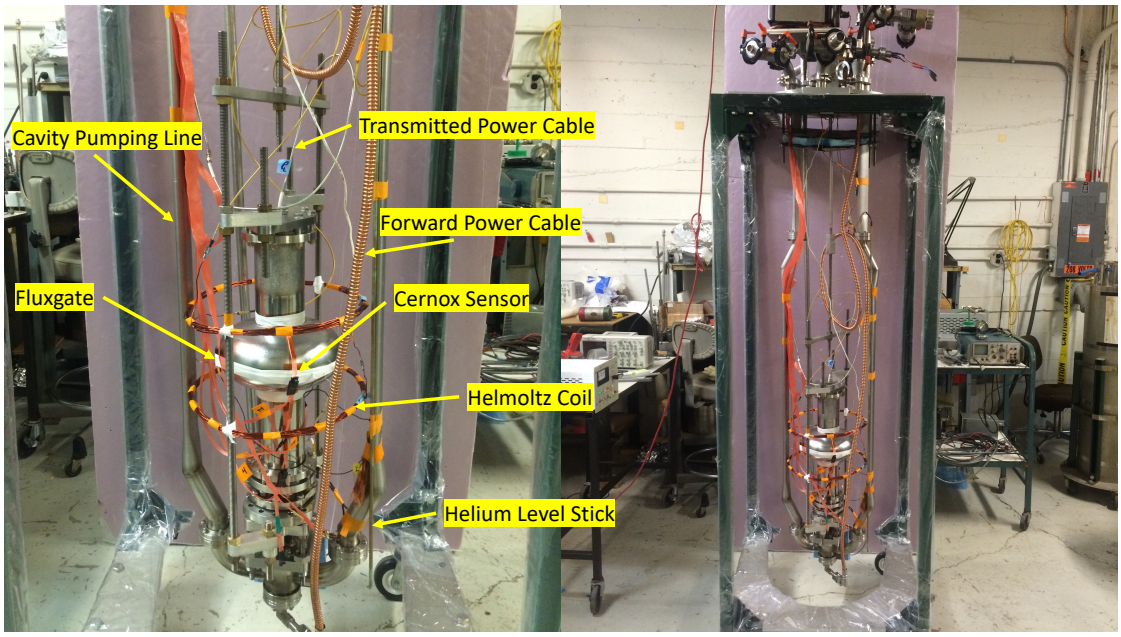

Figure 4.2: Test insert with a single-cell 1.3 GHz cavity installed with full instrumentation.

4.2.3 Nitrogen Doping

Nitrogen doping was first discovered at Fermilab by Grassellino *et al.* in 2013 [GRS+13]. The doping procedure starts with an ultra-high vacuum bake at 800 °C for 3 to 5 hr followed immediately by the introduction of a light nitrogen atmosphere (~40 mTorr) at 800 °C for 2 to 20 min and finally by an ultra-high vacuum anneal at 800 °C for 0 to 30 min. The nitrogen doped cavities in this dissertation use a doping time of 2 min and anneal of either 0 or 6 min.

This process grows a niobium nitride layer on the surface of the niobium [GRS+13]. From this nitride layer, nitrogen diffuses interstitially many μm into the bulk. Since the growth process is uncontrolled, different phases of nitride are formed. Some of these phases are lossy in RF fields and, therefore, must be removed. The removal of the nitride layer is done via EP (5 – 50 μm). Doing so allows one to finely control the electron mean free path since the nitrogen

concentration varies slowly over many penetration depths [Gon16a]. This treatment also result in 'anti-Q-slope', an example of which can be seen in Figure 4.1.

4.3 Cleaning and Assembly

After a cavity has received one of the surface preparations outlined above, it is taken to our Class 10 cleanroom where it is rinsed on a high pressure rinsing (HPR) system. The HPR system uses ultraclean de-ionized water and a rotating 750 – 1000 psi nozzle that traverses the length of the interior cavity surface to clean it of any contaminates that may interfere with the results of the cavity test. After the cavity has sufficiently air dried, it is taken to the Class 100 area of the cleanroom, installed on a vertical test insert, pumped down to ultra-high vacuum, and checked for vacuum leaks before being removed from the cleanroom.

4.4 Vertical Test Insert

The primary components of the test insert is the forward power coupler (FPC), transmitted power probe, and the pump line. The forward power coupler consists of a coaxial coupler that is parallel and concentric with the beam axis of the cavity. It couples the TEM mode of the coaxial cable supplying power to the cavity to the fundamental TM mode of the cavity. The transmitted power is a power pick up probe situated on the top plate of the cavity and also sits parallel and concentric to the beam axis. It provides a sample of the electromagnetic power stored in the cavity resonant mode. The pump line is present so that the cavity can be actively pumped on during a test ensuring that it stays under

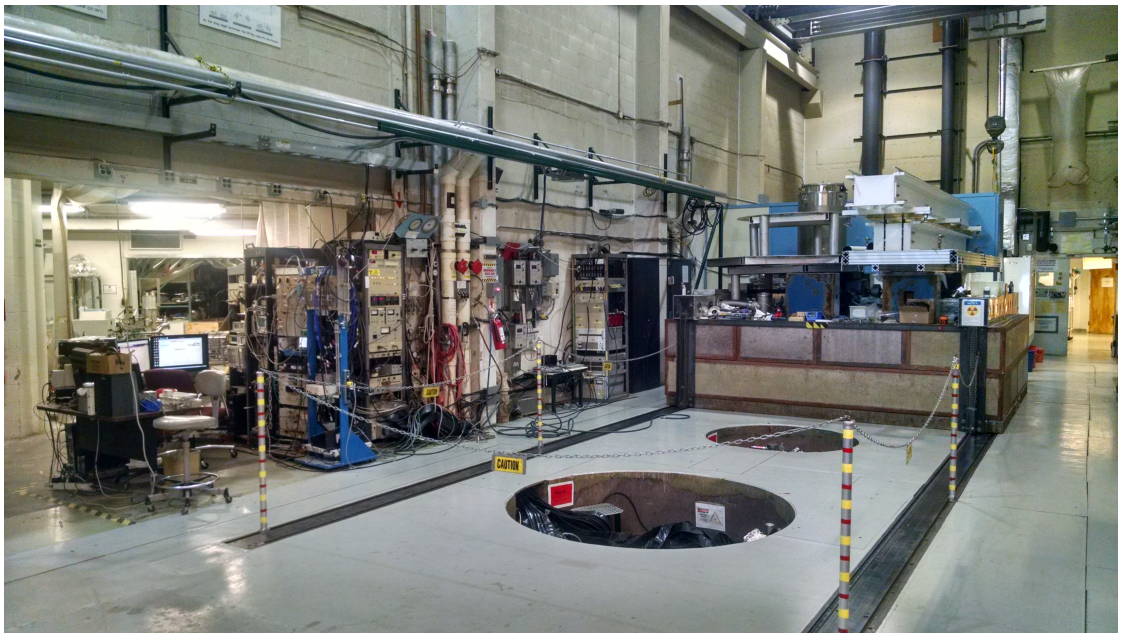

Figure 4.3: Test pits in the basement of Newman Laboratory at Cornell University. Each pit houses its own two-stage cryogenic dewar that house the test inserts during RF testing. A 90-ton concrete block slides on the two rails to cover the pit during testing. Photo adapted from [Hal17].

vacuum.

4.5 Cavity Testing

The vertical test insert is put into a two stage dewar that sits in an underground pit (Figure 4.3). The inner stage of the dewar is pumped out and the outer stage is filled with liquid nitrogen to act as a thermal shield. The inner stage is then filled with liquid helium, cooling the cavity from 300 K to 4.2 K. The speed of the cool down can be controlled so that either 'fast' or 'slow' cool downs can be done. A fast cool down typically takes 30 min with temperature gradients measured from one cavity iris to the other ranging from 10 to 20 K. Slow cool downs typically take 5 to 6 hr and have a temperature gradient of $\Delta T \lesssim 1$ K across the

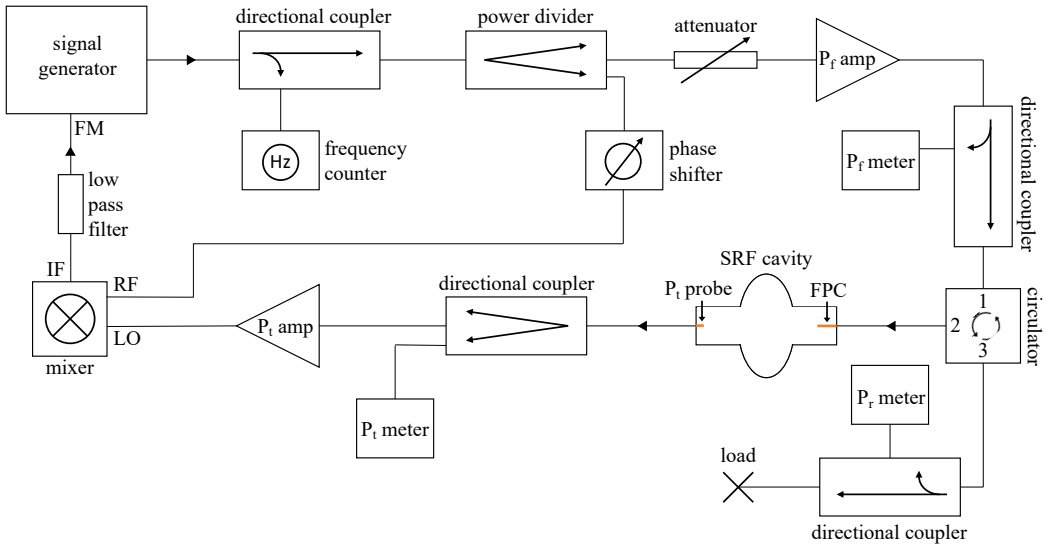

Figure 4.4: RF circuit diagram of single-cell test setup.

cavity. For niobium, cavities should be cooled down with the largest temperature gradient possible so that magnetic flux vortices are pushed out of the bulk as it transition from the normal to superconducting state [GL14, PCC+16]. For Nb_3Sn cavities, large temperature gradients (fast cool downs) create a strong thermoelectric effect which produce magnetic fields in the metal. Magnetic vortices can get trapped in the Nb_3Sn layer which greatly increases surface resistance [Hal17, Por21]. Therefore, it is ideal to cool down with the smallest temperature gradients possible to reduce the production of trapped flux vortices via the thermoelectric effect.

In general, the most prevalent measurements taken during an RF test of a superconducting cavity is the ubiquitous field dependence of the quality factor, Q_0 vs E_{acc}, the temperature dependence of the quality factor, Q_0 vs T, and the temperature dependence of the resonant frequency, f vs T.

4.5.1 Measurement Apparatus

The RF apparatus for testing single-cell cavities has several key features which will be discussed here. The circuit diagram for the RF test setup is shown in Figure 4.4. The system begins with a signal generator that outputs a low power frequency modulated RF signal which is split by a directional coupler. The coupled port connects to a frequency counter that is used to measure that cavity resonance frequency during data collection. The output port connects to a power divider. One side of the divider feeds into the phase-locked loop (PLL) portion of the circuit which will be discussed below. The other side of the divider goes to an adjustable attenuator so that the forward power level can be adjusted before going into the amplifier. The output of the amplifier then goes through a directional coupler which allows a sample of the forward power, P_{f}, to the cavity to be measured using an RF power meter. The output then connects to a circulator with the forward power flowing from port 1 to 2 and into the forward power coupler (FPC) in the cavity. The reverse power, P_{r}, flowing back out through the FPC enters port 2 and exits port 3 of the circulator where is it split by a directional coupler. The majority of P_{r} is dissipated in a load while the coupled port of the directional coupler connects to a power meter for measurement. The transmitted power, P_{t}, is picked up by the P_{t} probe and is sent through a power divider where the signal is split between the PLL and a power meter.

The PLL system ensures the forward signal to the cavity remains locked on resonance. This system consists of a double balanced mixer, phase shifter, and a low pass filter. The RF input of the mixer comes from a sample of the forward power from the signal generator that passes through an adjustable phase shifter that is used to optimize the energy in the cavity. The LO input comes from an

amplified sampling of the transmitted power. These two inputs to the mixer generates a DC signal that is then sent from the IF output of the mixer to the frequency modulation (FM) input on the signal generator. The signal generator then uses this signal to adjust its output frequency. A More detailed discussion of the RF measurement system and the cryogenic system for cavity testing can be found in [PKH08, Hal17, Man20]

4.5.2 Measuring Q_0

First, we must consider some preliminary information. The moment the forward power is turned off, the total power of the system can be written in terms of the power leaking out of the forward power coupler, P_e, the power leaking out of the transmitted power probe, P_t, and the power dissipated by the cavity walls, P_c:

$$P_{\text{tot}} = P_e + P_c + P_t. \tag{4.1}$$

As with the cavity quality factor Q_0, we can also write the total power in terms of a 'loaded' quality factor, Q_L,

$$P_{\text{tot}} = \frac{\omega U}{Q_L}, \tag{4.2}$$

where U is the total energy stored in the fields and $\omega = 2\pi f$ is the angular resonant frequency. The energy stored in the cavity fields decreases as power leaks through the couplers or is dissipated by the resistive cavity walls and obeys the first-order differential equation

$$\frac{dU}{dt} = -P_{\text{tot}} = -\frac{\omega U}{Q_L}. \tag{4.3}$$

Defining the loaded time constant $\tau_L = Q_L/\omega$ and solving for $U(t)$ we obtain

$$U(t) = U_0 e^{-t/\tau_L}, \tag{4.4}$$

where U_0 is the stored energy at the instant the RF power is turned off (i.e., $t = 0$). Using the definition for quality factor in terms of stored energy, frequency, and power, we can rewrite Equation 4.1 as

$$\frac{1}{Q_L} = \frac{1}{Q_e} + \frac{1}{Q_0} + \frac{1}{Q_t}, \tag{4.5}$$

where Q_e and Q_t are the external quality factors for the forward and transmitted power ports on the cavity, respectively, and are given by $Q_{e,t} = \omega U / P_{e,t}$. Defining the coupling factors $\beta_e = Q_0/Q_e = P_e/P_c$ and $\beta_t = Q_0/Q_t = P_t/P_c$, the above expression can be written as

$$Q_0 = Q_L(1 + \beta_e + \beta_t). \tag{4.6}$$

However, since $\beta_e \sim 1$ and $\beta_t \ll 1$, we can simplify the above expression further to

$$Q_0 = \omega\tau_L(1 + \beta_e). \tag{4.7}$$

Thus, Q_0 can be calculated from a measurement of τ_L and β_e. The measurement process for obtaining β_e is discussed in the section below.

4.5.3 Measuring β

Two different methods are used to calculate β_e and are averaged together [PKH08]. The 'steady-state' method uses the off-resonance reverse power, P_i, which effectively measures the forward or 'incident' power on the cavity and the on resonance reverse power, P_r, to obtain

$$\beta_1 = \frac{1 + a\sqrt{P_r/P_i}}{1 - a\sqrt{P_r/P_i}} \tag{4.8}$$

where $a = +1$ if the cavity is overcoupled ($\beta > 1$) or $a = -1$ if the cavity is undercoupled ($\beta < 1$) .The 'instantaneous' method uses the emitted power, P_e, measured at the first point of the decay curve after the RF power has been turned off and P_i to obtain

$$\beta_2 = \frac{1}{2\sqrt{P_i/P_e} - 1}. \tag{4.9}$$

4.5.4 Measuring E_{acc}

To calculate the accelerating gradient, E_{acc}, the power in the cavity must first be calculated from the coupler factor and the measured forward power. The initial stored energy, $U(t = 0) = U_0$ is then calculated from this. Finally, the stored energy is used to determine the accelerating gradient. The power dissipated by the cavity is calculated from the on resonance forward power, P_f, and and the averaged coupler factor β,

$$P_c = \frac{4\beta}{(1+\beta)^2} P_f. \tag{4.10}$$

This initial stored energy is calculated from the relation

$$U_0 = \frac{Q_0 P_c}{\omega}. \tag{4.11}$$

Finally, E_{acc} is given by the expression

$$E_{\text{acc}} = \left(\frac{\kappa_1}{\kappa_2}\right) \sqrt{U_0} \tag{4.12}$$

where $\kappa_1 = E_{\text{pk}}/\sqrt{U}$ and $\kappa_2 = E_{\text{pk}}/E_{\text{acc}}$ are the aforementioned geometry-dependent cavity parameters determined through finite element simulations.

CHAPTER 5

LOW TEMPERATURE INFUSION

Reducing the microwave surface resistance of superconducting cavities is a primary focus of the SRF community. Smaller resistance results in smaller cryogenic loss at a given accelerating gradient which leads to smaller cryogenic cooling power costs. In this chapter, the inclusion of interstitial impurities such as carbon, nitrogen, and oxygen and their role in the reduction of the temperature dependent component, R_{BCS}, of the surface resistance will be discussed. It will be shown that interstitial impurities near the RF surface (i.e., < 100 nm) play a significant role in cavity performance. The role of impurity species and concentration on cavity performance will be examined.

5.1 Historical Background

Nitrogen-doping of niobium cavities was discovered by Grassellino *et al.* [GRS+13]. The process involved baking the cavities at high temperatures (~800 °C) in a light atmosphere of nitrogen gas (~20-40 mTorr) introducing significant amounts of nitrogen interstitials (~0.09-0.4 at.%) over tens of μm into the niobium surface [GRS+13, Gon16a]. This resulted in the the so-called 'anti-Q-slope', an increase in cavity quality factor Q_0 with increasing accelerating field E_{acc}. Because lossy, or poorly suerconducting nitride phases grow on the cavity surface in this temperature range, cavities treated with this process need electropolishing (EP) after the doping to remove the surface nitride layer. Electropolishing also doubled as a way to control the concentration of interstitial nitrogen as the concentration slowly decreases over many μm into the surface.

A few years later, it was found that cavities could be baked at much lower temperatures (~160 °C) in the same nitrogen atmosphere to achieve similar results [Gra17]. This process was called nitrogen infusion and offered a way to introduce anti-Q-slope without the need for post treatment EP since nitride phases do not grow in this temperature regime. Around the same time, it was discovered that cavities could be baked at the same infusion temperature but instead with an argon and carbon dioxide gas mixture and still obtain anti-Q-slope [Kou17]. This discovery suggested that nitrogen may not be solely responsible for the observed anti-Q-slope in infusion type preparations. This notion was later reinforced by Lechner *et al*. [Lec21] with the discovery that cavities baked in vacuum between 300 – 400 °C also resulted in anti-Q-slope due to the dissolution of the native surface oxide layer into the niobium.

5.2 Surface Treatments

All cavities shown in this chapter are of the TESLA elliptical design similar to [ABB+00] with a resonant frequency of 1.3 GHz operating in the TM_{010} mode. Surface preparation begins with an electropolish (EP) of the interior cavity surface to remove impurities from machining or previous treatments. The initial EP will typically remove anywhere from 100 to 150 μm from the cavity surface.

The infusion process involves several baking steps in an ultra-high vacuum furnace. The first step is a high temperature anneal in the range of 800 to 900 °C to degas hydrogen introduced during the EP and mostly dissolve the surface oxide. The next optional anneal at low temperature serves to allow the cavity to equilibrate with the furnace temperature as it cools down from the first an-

Table 5.1: Cavity treatments

Treatment	Anneal #1	Anneal #2	Infusion	Gas	Anneal #3	Chemical Etching[1,2,3]
C1P1	800 °C (3 hr)	—	160 °C (48 hr)	Ar + CO_2	—	HF
C1P2	800 °C (3 hr)	—	160 °C (48 hr)	Ar + CO_2	—	HF + OP (27 nm)
C1P3	800 °C (3 hr)	160 °C (3 hr)	160 °C (24 hr)	N_2	—	—
C1P4	800 °C (3 hr)	160 °C (3 hr)	160 °C (24 hr)	N_2	—	OP (54 nm)
C2P1	900 °C (3 hr)	160 °C (3 hr)	160 °C (4.5 dy)	N_2	—	—
C2P2	900 °C (3 hr)	160 °C (3 hr)	160 °C (4.5 dy)	N_2	—	HF
C2P3	900 °C (3 hr)	160 °C (3 hr)	160 °C (4.5 dy)	N_2	—	HF (×2)
C3P1	800 °C (3 hr)	160 °C (3 hr)	160 °C (48 hr)	N_2	—	—
C3P2	800 °C (3 hr)	160 °C (3 hr)	160 °C (48 hr)	N_2	—	HF (×2)
C3P3	800 °C (3 hr)	160 °C (3 hr)	160 °C (48 hr)	N_2	—	HF (×2) + EP (100 nm)
C4P1	800 °C (5 hr)	—	160 °C (48 hr)	Ar + CO_2	—	OP (54 nm)
C5P1	800 °C (12 hr)	—	160 °C (48 hr)	N_2	160 °C (168 hr)	—
C5P2	800 °C (12 hr)	—	160 °C (48 hr)	N_2	160 °C (168 hr) + 75 °C (6 hr)	—

[1] HF = hydroflouric acid rinse of interior cavity surface (removes ~5 nm).
[2] OP = oxypolish (i.e. anodization followed by HF rinses).
[3] EP = electropolish

neal. The following is the most important step of the process: 'infusion'. The furnace is injected with a light atmosphere (~40 mTorr) of either ultra-high purity nitrogen or ultra-high purity argon mixed with 10 ppm CO_2 depending on the recipe. The bake times of the infusion process range from 24 hr to several days. The long bake times of this step are necessary to allow carbon and nitrogen, which diffuse very slowly compared to oxygen, enough time to penetrate the cavity surface and diffuse into the material. An additional vacuum anneal after infusion is optional. Finally, cavities are removed from the furnace and prepared for the initial RF test.

After the initial RF test, the cavity may receive chemical etching to remove small amounts from the interior cavity surface. Three methods of chemical etching are used, hydroflouric acid (HF) rinsing [PKH08], oxypolishing (OP), and electropolishing (EP) [PKH08]. An HF rinse involves filling the interior cavity volume with 48% HF for 10 min, emptying the acid from the cavity and rinsing it with de-ionized water for several minutes. This process removes the approximately 5 nm thick surface oxide layer from the cavity surface and, in the process of oxide regrowth, converts about 2 nm of niobium into a new oxide layer. Oxypolishing is a two part procedure: anodizing the cavity surface to build a thick oxide layer, followed by HF rinsing to remove the built-up oxide. This process can be repeated multiple times to achieve the desired amount of material removal and will typically be used to remove tens of nm from the surface. The electropolishing procedure is explained in Chapter 3 and can be used to remove as little as 100 nm up to 150 µm from the cavity surface. All individual infusion preparations discussed in this chapter are summarized in Table 5.1.

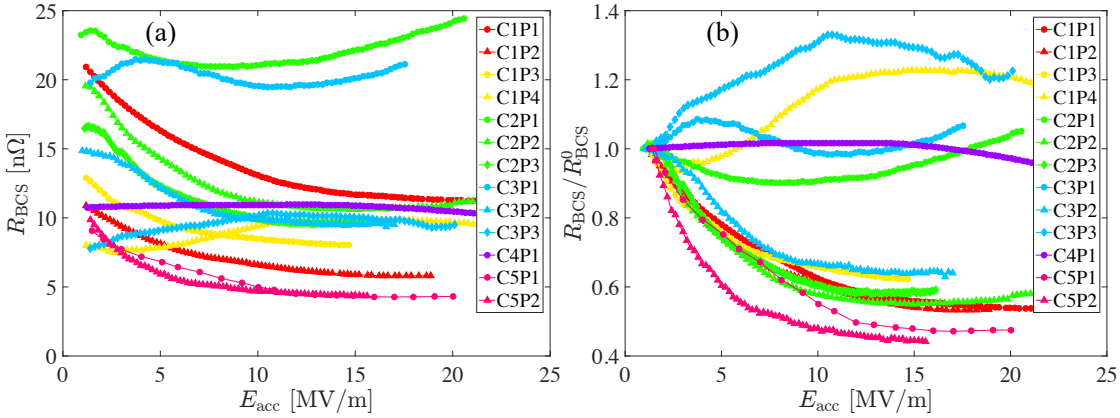

Figure 5.1: (a) BCS resistance and (b) BCS resistance normalized to $R_{BCS}(E_{acc} = 1$ MV/m) for all cavity treatments. All curves shown were measured at 2.0 K with 1.3 GHz cavities.

5.3 Cavity Performance

Cavity performance is analyzed by breaking down the measured surface resistance into its temperature dependent R_{BCS} and independent R_{res} components as in Equation 3.14 as a function of field. The R_{BCS} curves at 2.0 K for all cavity preparations are shown in Figure 5.1(a). To more clearly see the effects of a particular surface treatment, R_{BCS} normalized to a low field value is shown in Figure 5.1(b). For example, for preparation C1P1, it can be seen that the resistance at high fields (i.e., ~20 MVm) is roughly 60% of its value at low field (i.e., ~1 MV/m). The field dependent R_{res} is shown in Figure 5.2 for all surface preparations. An approximately linear field dependence is observed for all curves in the medium to high field range.

The effect of the amount of post-bake chemical etching of the cavity surface will be investigated to determine which interstitial impurities introduced during baking are responsible for the observed anti-Q-slope effect, if any of the impurities are particularly unique in their effect, and if the anti-Q-slope is a near

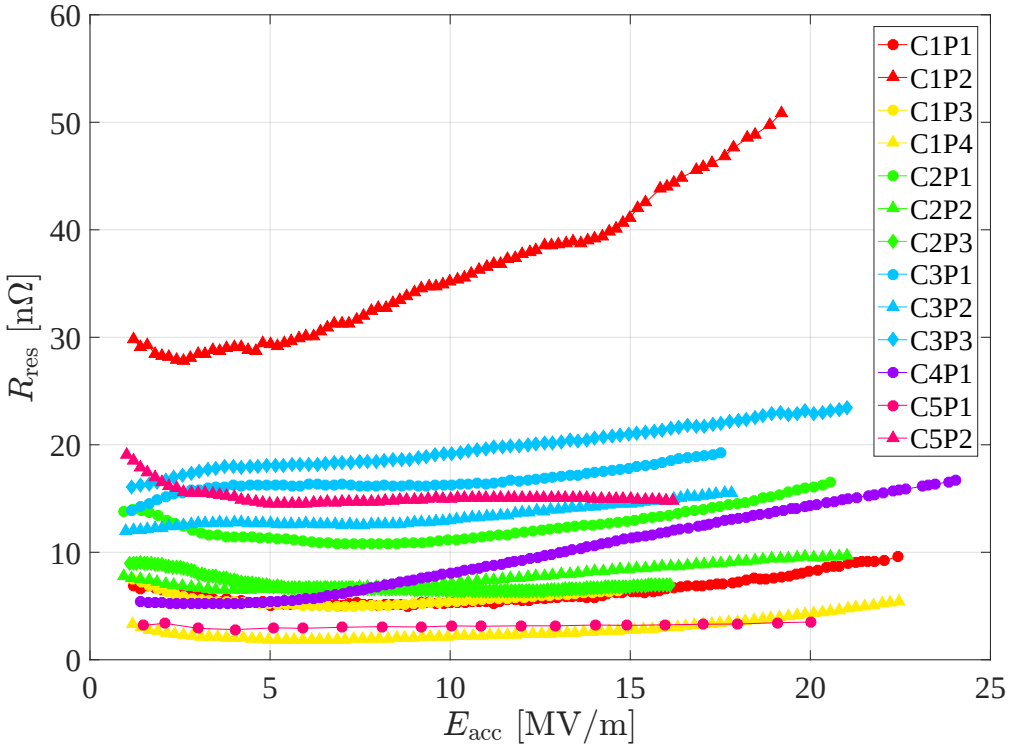

Figure 5.2: Residual resistance as a function of accelerating gradient for all cavity preparations.

surface phenomenon (e.g., caused by impurities in the first few nm of the RF surface).

5.3.1 Nitrogen Infusion

The cavities treated in a nitrogen atmosphere are shown in Figure 5.4(a)-(d). Each subplot shows a sequence of treatments on a single cavity beginning with the data acquired from an RF test immediately after the initial bake followed by data acquired after one or more chemical etches.

Treatment C1P3 (see Figure 5.4(a)) shows a strong reduction in R_{BCS} following its 24 hr nitrogen infusion. However, after approximately 54 nm of etch-

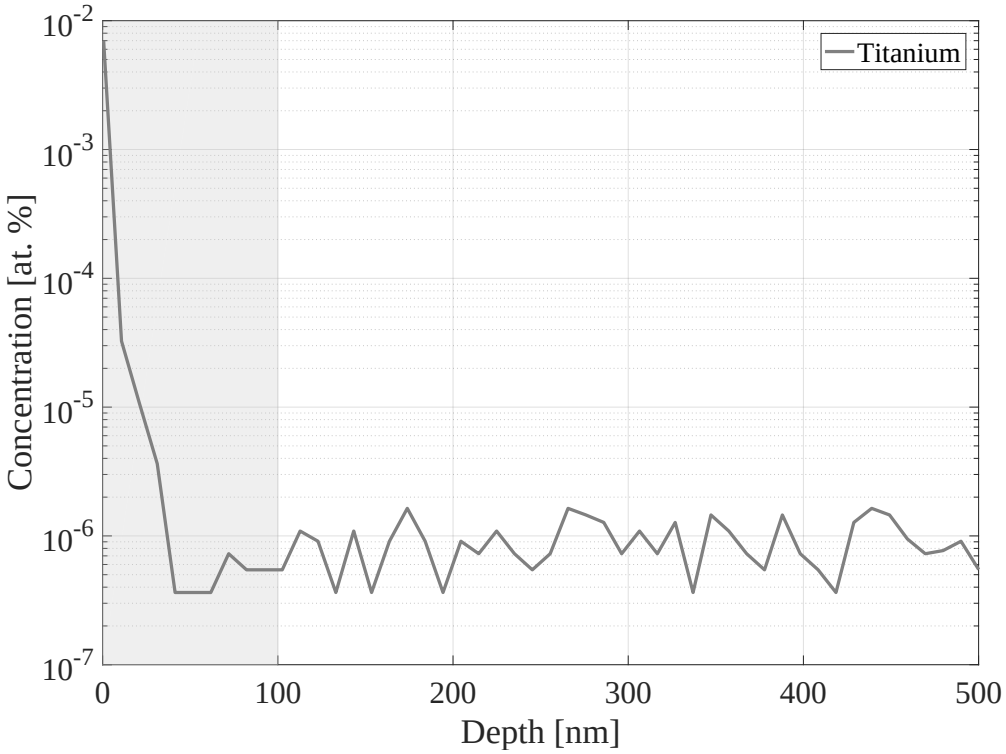

Figure 5.3: Concentration profile of Ti from the witness sample to C2P1.

ing via OP, the reduction disappears completely leading to the conclusions that whatever is responsible for the reduction of the resistance occurs in a depth less than ~50 nm.

Treatment C2P1 displays a weak dependence on field, $R_{\mathrm{BCS}} > 20$ nΩ for all field strengths, and a higher R_{res} than its subsequent treatments. It was discovered that the NbTi flanges on the cavity contaminated the cavity surface with Ti. Secondary ion mass spectroscopy (SIMS) measurements were taken to obtain the concentration of the Ti contamination as a function of depth into a witness sample baked alongside the C2P1 cavity treatment. The SIMS measurement of the Ti profile is shown in Figure 5.3. A single HF rinse remedied the situation (see C2P2), reducing R_{BCS} by up to ~10 nΩ in the medium and high field range, reducing R_{res} by an average of 4.8 nΩ, and restoring the strong reduction of R_{BCS}

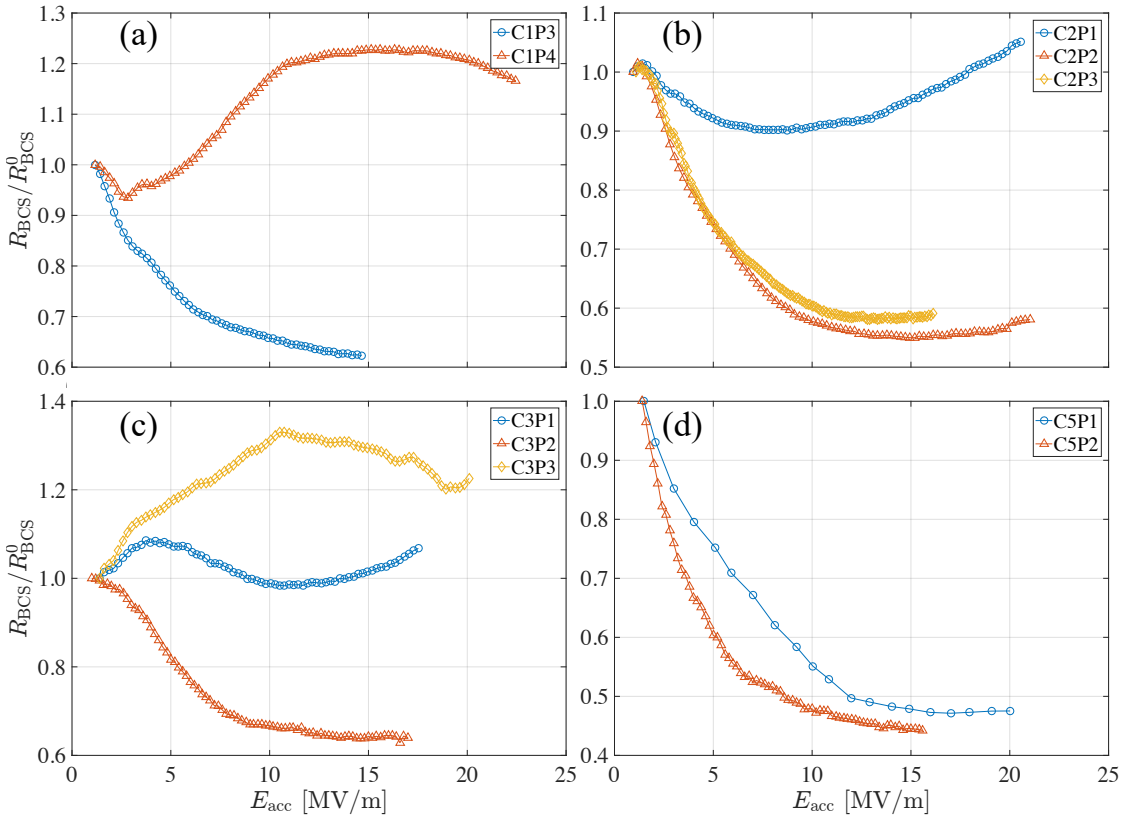

Figure 5.4: Normalized R_{BCS} resistance at 2.0 K for all nitrogen treatments.

with field. An additional HF rinse (C2P3) had little to no effect compared to the previous treatment (C2P2); the only noticeable change was a slight drop in the magnitude of R_{BCS} across the entire field range. An important conclusions can be drawn from these observations. Titanium contamination in the first few nm can destroy the anti-Q-slope leading to the conclusion that surface chemistry can turn the anti-Q-slope on or off.

The C3Px sequence shows similar behavior to the C2Px sequence as it also had NbTi flanges and Ti contamination on the RF surface. Two HF rinses (C3P2) restored the reduction of R_{BCS} with field and greatly reduced its magnitude over the entire field range. An additional 100 nm EP, however, completely reversed the field dependence of R_{BCS} displaying a field dependence similar to a standard

cavity (i.e., a cavity that receives only a high temperature anneal). This further reinforces that etching more than ~50 nm completely removes the suppression of R_{BCS} with field for this specific treatment. This also leads to the conclusion that the beneficial effects of infusion can be the result of the impurities at depths of at least ~5 nm. This demonstrates that the chemistry of the first few nm plays an important role in the behavior of R_{BCS}.

Treatments C5P1 and C5P2 show a slightly stronger drop in R_{BCS} compared to the other treatments discussed in this chapter. This may be due to the additional post-infusion vacuum anneal which would allow the impurities extra time to diffuse further into the surface. See, for example, the difference relative drop of R_{BCS} between the C5P1/C5P2 treatments and the other nitrogen infusion treatments in Figure 5.6. However, additional testing would be needed to investigate this hypothesis further.

5.3.2 Carbon-Oxygen Infusion

Treatments C1P1 and C1P2 (see Figure 5.5) are significant in that they show that it is not necessary to use nitrogen gas during the infusion step. In these, as well as the C4P1 treatment, a mixture of research plus grade Ar (99.9999% purity) from Airgas, Inc. mixed with 10 ppm CO_2 was used during the infusion step. The initial treatment, which included an HF rinse, showed a strong reduction in R_{BCS}. More interestingly, after also receiving a 27 nm OP (i.e., 32 nm of total etching after the bake) reveals that the field dependence of R_{BCS} changed only slightly. Therefore, the positive effect of infusion lies at least 30 nm into the surface and turns 'off' somewhere between 30–50 nm of etching. Treatment

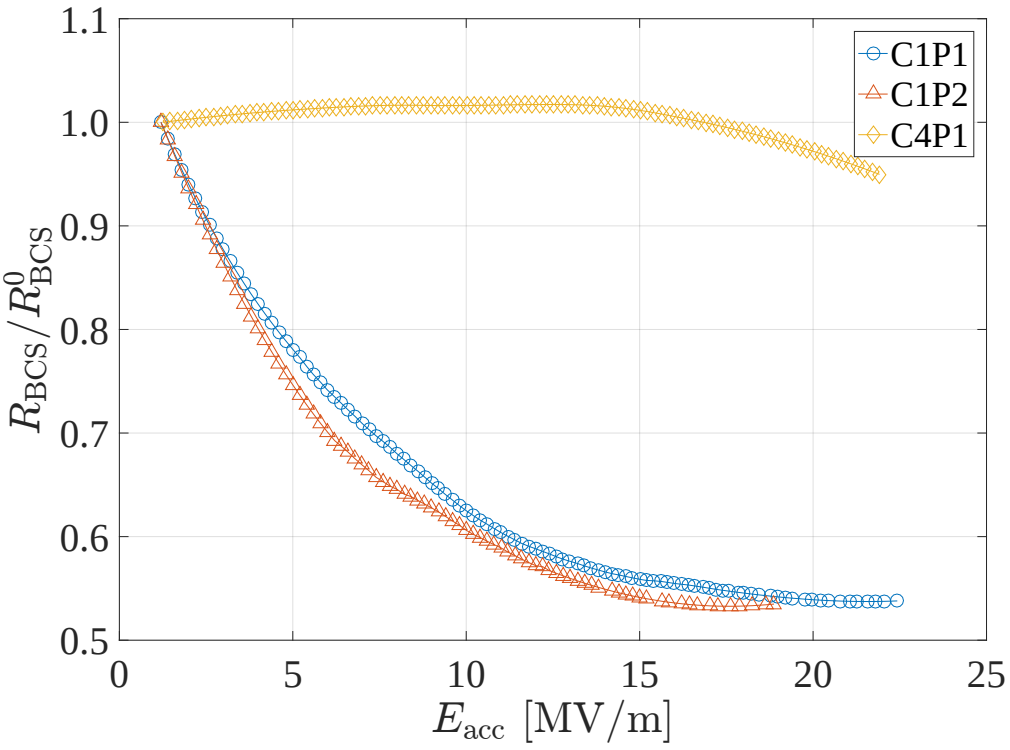

Figure 5.5: Normalized R_{BCS} resistance at 2.0 K for carbon-oxygen treatments.

C4P1 only having received a single 54 nm OP after the bake causes the reduction to disappear completely further reinforcing that the region of interest lies no further into the RF surface than ~50 nm for these treatments.

It is also curious to note the strongly linear dependence of R_{res} with field after the two OP treatments but not in the case of C1P4 which was nitrogen treated. This finding may warrant further investigation. The abnormally high residual of C1P2 may be due to many factors such as contamination of the RF surface during cavity assembly onto the test equipment or large amounts of trapped flux due to high residual magnetic fields during cool down.

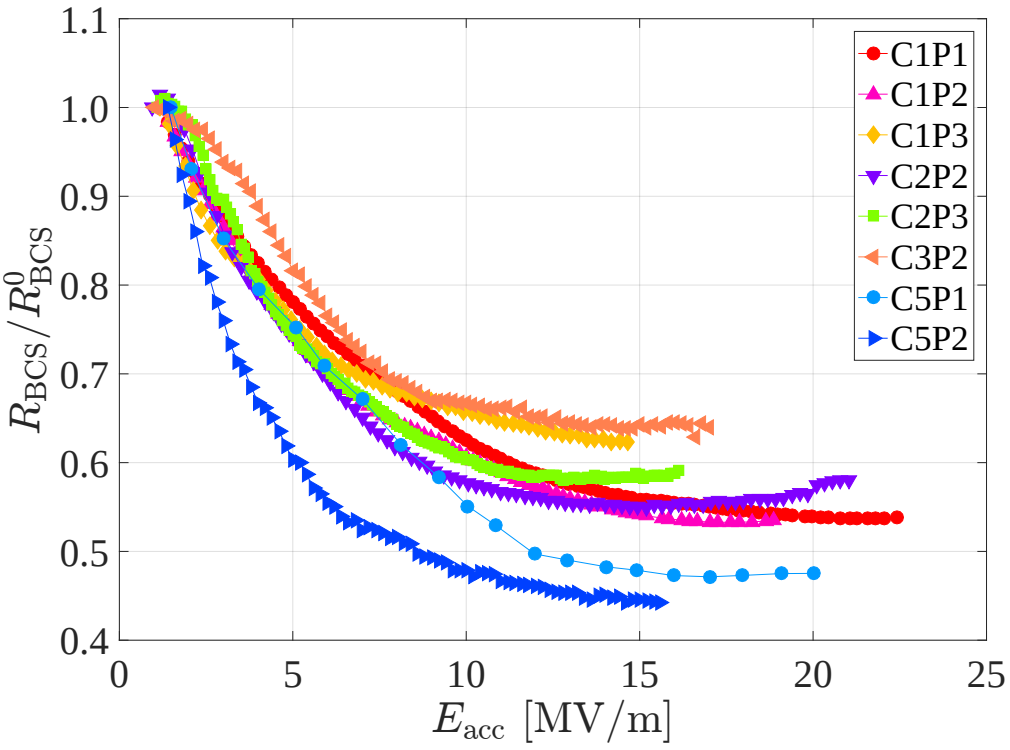

Figure 5.6: Normalized R_{BCS} resistance at 2.0 K for all treatments that produce a field suppressed BCS resistance.

5.3.3 Performance Reproducibility

On a final note, it is important to mention the reproducibility of the field suppression of R_{BCS}. It has been shown that infusion time can vary from one to several days and the impurity gas used during the infusion (N_2 vs. CO_2) can be changed while still producing very similar results. The treatments that produced such results are shown and summarized in Figure 5.6. The variance of the infusion times may be an indication that the required diffusion into the RF layer happens on time scales less than 24 hr. The use of different infusion gases implies that the behavior of R_{BCS} is rather insensitive to the species of the interstitial.

5.4 Secondary Ion Mass Spectroscopy Measurements

Large grain or single crystal niobium witness samples received a 50−100 μm EP and were baked along side treatments C1P1, C1P3, C2P1, and C3P1. The samples did not receive any chemistry after the bake. They were then sent to EAG Laboratories for secondary ion mass spectroscopy measurements to acquire the concentration profiles of C, N, and O as a function of depth into the material. The concentration profiles shown throughout this section for the cavity treatments with chemical etching were obtained by shifting the concentration profiles from the witness sample measurements by the amount of chemical etching the treatments received. Therefore, the concentration profiles for treatments that included chemistry do not show the effects of the regrowth of the surface oxide layer after the chemical treatment is completed. These profiles and their importance in explaining the observations of the previous section will be discussed here.

Figure 5.7(a) shows the impurity concentrations of C (red), N (green), and O (blue) as a function of depth for the CO-infusion treatments of C1P1, C1P2, and C4P1. The light gray region spanning from 0 to 100 nm represents the RF penetration layer. The light purple region represents the typical nitrogen concentrations of high temperature nitrogen doped cavities which are relatively constant over several microns [Gon16a].

Figure 5.7(b)-(d) show the C, O, and N concentration profiles along with post-treatment etching included. Treatment C1P1 has concentrations of C and O well above the typical range of values for a nitrogen doped cavity and are the primary contributors to reducing the electron mean free path near the sur-

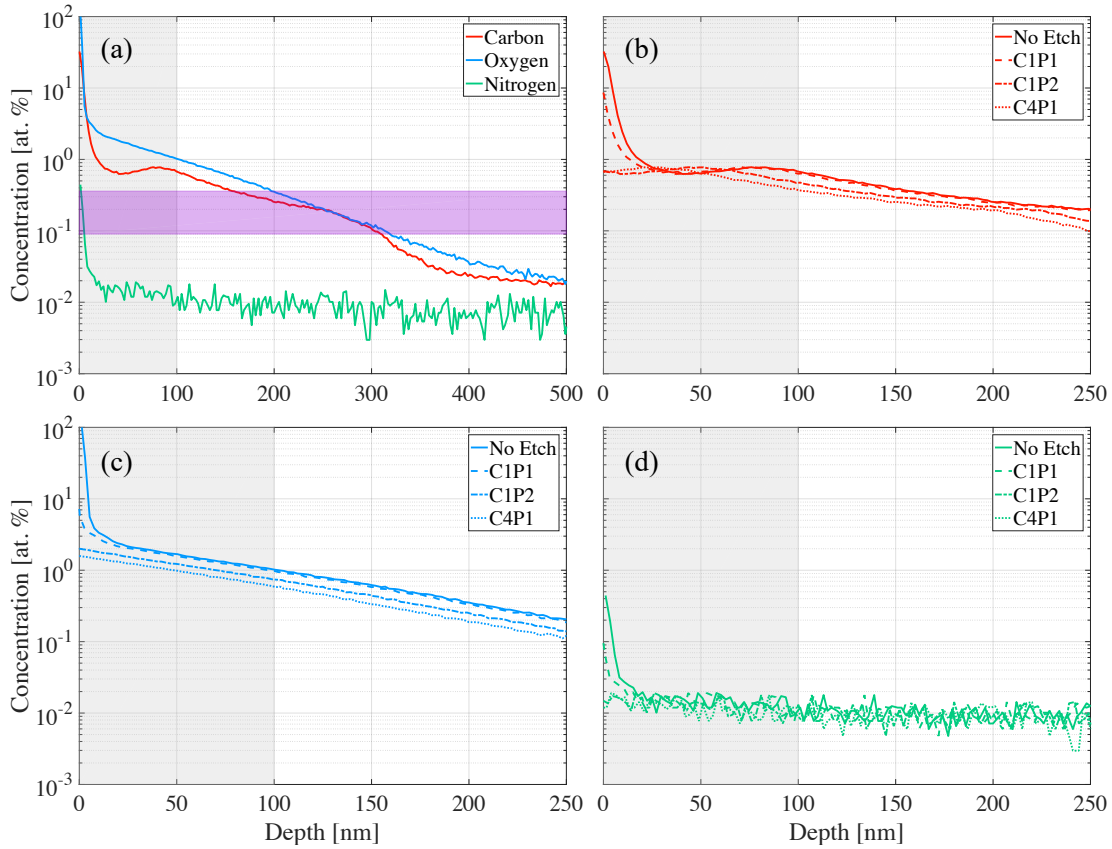

Figure 5.7: (a) Concentration profiles for C, N, and O for a single-crystal witness sample baked alongside the C1P1, C1P2, and C4P1 CO-infusion cavity treatment. The concentration profile for C (b), O (c), and N (d) for all three cavity treatments are shifted to the left by the estimated amount of material removed from their respective post-bake chemical treatments.

face [Man20]. The nitrogen concentration is ~0.09 at. % at the surface sitting just on the lower limit of typical values for nitrogen doped cavities. One may be tempted to assume that the nitrogen is still the responsible factor for the performance change of the surface resistance. However, it should be noted that in the next treatment C1P2, the C and O concentrations still sit above the upper limit of the nitrogen-dope band while the N concentration is situated firmly at background levels. This clearly demonstrates that nitrogen plays no role in the appearance of the anti-Q-slope in this cavity treatment and that C and O are responsible. This goes against the long held belief that nitrogen was the sole

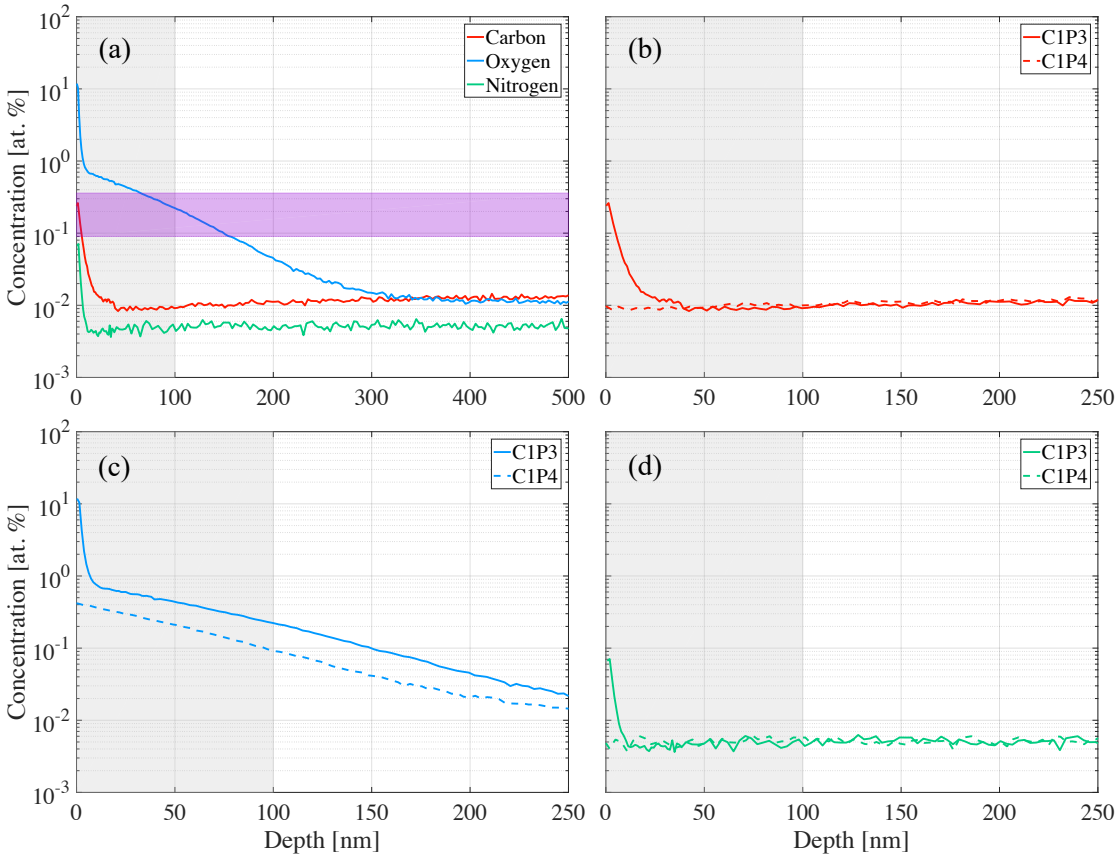

Figure 5.8: (a) Concentration profiles for C, N, and O for a large grain witness sample baked alongside the C1P3 and C1P4 N-infusion cavity treatment. The concentration profile for C (b), O (c), and N (d) for both cavity treatments are shifted to the left by the estimated amount of material removed from their respective post-bake chemical treatments.

culprit in producing anti-Q-slope in infused cavities and was somehow special. In the last treatment, C4P1, the C signal remains relatively stable while the O signal is approximately reduced by half from 1 to 0.5 at. % and the N signal is at background levels. The reduction of O and the relatively similar levels of C and N from C1P2 to C4P1 indicates that O plays a large role in the appearance of the anti-Q-slope.

Figure 5.8 shows the concentration profiles for treatments C1P3, which had an anti-Q-slope, and C1P4, which did not. For treatment C1P3, O sits well

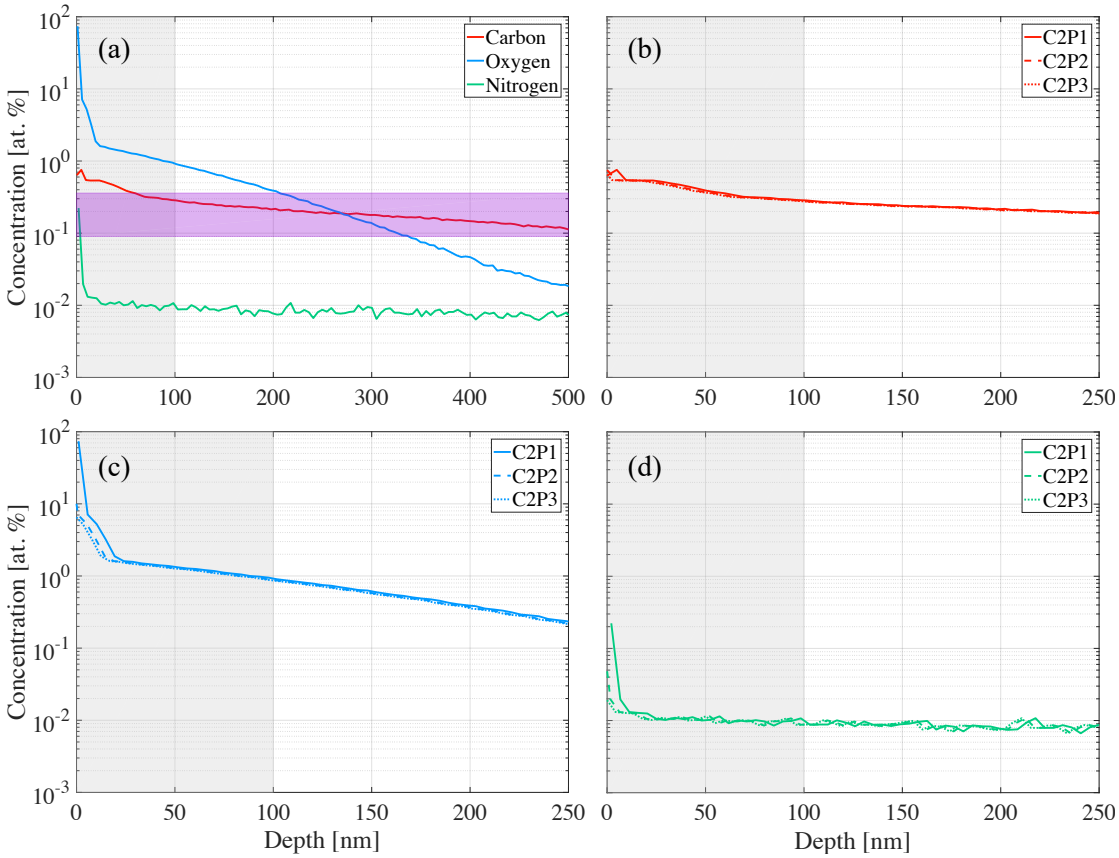

Figure 5.9: (a) Concentration profiles for C, N, and O for a large grain witness sample baked alongside the C2P1, C2P2, and C2P3 N-infusion cavity treatment. The concentration profile for C (b), O (c), and N (d) for the three cavity treatments are shifted to the left by the estimated amount of material removed from their respective post-bake chemical treatments.

above, C inside, and N below the nitrogen dope range near the surface again suggesting that O and potentially C play the primary role in the drop in R_{BCS}. After etching both C and N concentrations drop to background levels while O is reduced significantly near the surface and through the entire region of interest. In this case, the field suppression of R_{BCS} disappears completely indicating that if the concentrations of the impurities drop too low the anti-Q-slope will be turned 'off'.

Figure 5.9 shows the concentration profiles for the N-infusion treatments

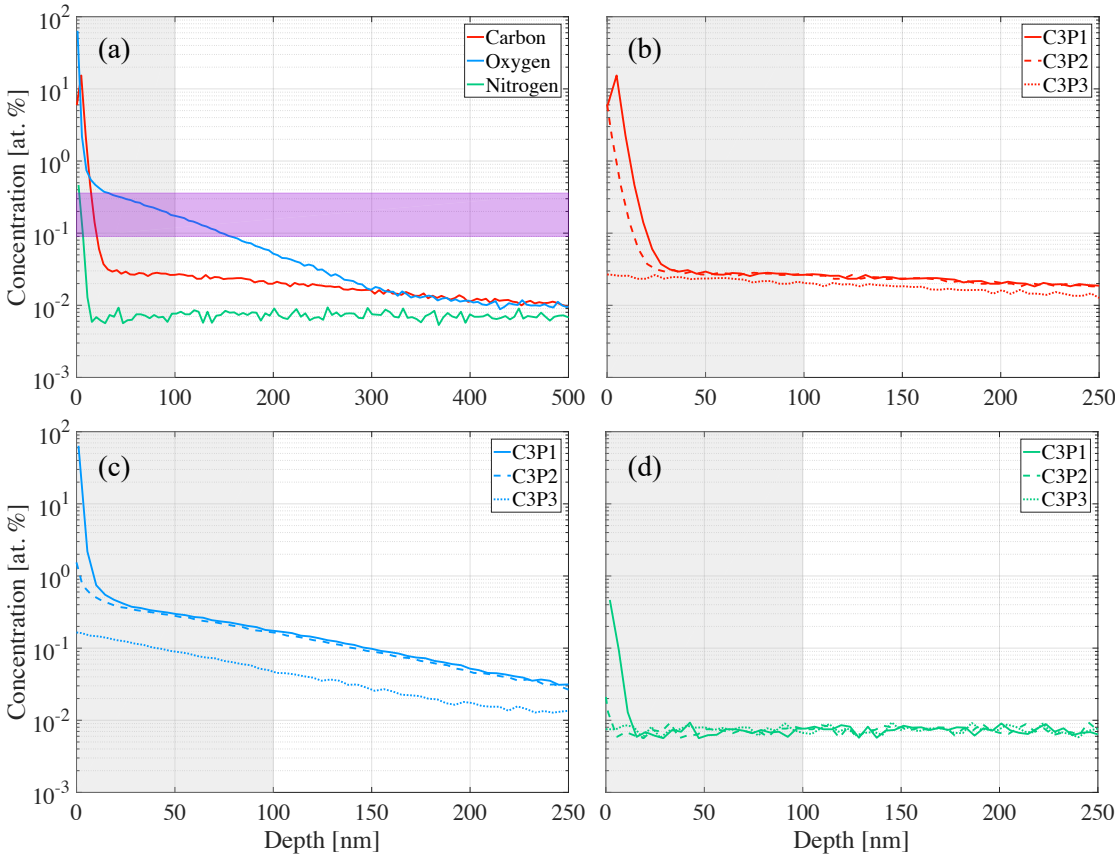

Figure 5.10: (a) Concentration profiles for C, N, and O for a large grain witness sample baked alongside the C3P1, C3P2, and C3P3 N-infusion cavity treatment. The concentration profile for C (b), O (c), and N (d) for the three cavity treatments are shifted to the left by the estimated amount of material removed from their respective post-bake chemical treatments.

C2P1, C2P2, and C2P3. Both C2P2 and C2P3 have a very similar R_{BCS} curves while although much weaker C2P1 still displays a field suppression for fields <10 MV/m. The lack of suppression of the resistance in the C2P1 treatment is primarily due to Ti contamination, as discussed previously, which appears to offset the benefits from the other impurties. However, a single HF rinse removed sufficient material to reduce the Ti contamination to levels where the anti-Q-slope re-appeared. The concentration profile of Ti for this treatment is shown in Figure 5.3. The C profile remains mostly unchanged from one treatment to the next whereas both N and O are significantly reduced after etching.

However, the O concentration remains quite high sitting well above 1 at. % for all three treatments. On the other hand, N is reduced to background levels. It appears cavity performance is not sensitive to change in the O concentration near the surface for concentrations above 1 at. % as can be seen in Figure 5.4(b).

Concentration profiles for N-infusion treatment sequence C3P1, C3P2 and C3P3 are shown in Figure 5.10. The cavity in used in the C3Px sequence of treatments also had NbTi flanges and suffered from Ti contamination that required required chemical etching to remove. Treatment C3P1 did not have an anti-Q-slope as a consequence of this contamination. After two HF rinses (C3P2), the field suppression of R_{BCS} was restored, again reaffirming the previous observation that an HF rinse is sufficient to remove the negative effects of Ti contamination in these infusion treatments and that HF rinsing does not destroy the observed field suppression of R_{BCS}.

The O concentration is low enough that, when compared to other treatments, no field suppression should be observed. However, the C concentration is much higher in comparison to the other treatments previously discussed and may help to offset the lack of oxygen. Again, the N concentration is low enough to assume that it plays little to no role in cavity performance. In C3P3, it is no surprise that cavity performance returns to normal as the concentrations of all three impurities drop to insignificant levels.

5.5 Discussion

Important conclusions regarding the role of the interstitial impurities C, N, and O in the appearance of the anti-Q-slope can be drawn from the observations

made in this chapter. These conclusions, as well, as other topics related to the role these impurities play, will be discussed here.

The fact that the CO-infusion treatment C1P2 displayed anti-Q-slope after approximately 32 nm of etching indicates that N is not necessarily needed to produce this effect. For quite some time it was assumed that N was primarily, if not solely, responsible for the observed field suppression of R_{BCS}. However, the SIMS measurements performed on the witness sample for the C1P2 treatment indicate that the N concentration was at background levels (~0.01−0.02 at. %) throughout the penetration layer (~100 nm) and, therefore, played little to no role in the observed anti-Q-slope for this recipe.

Figure 5.11 shows the concentration profiles for C, N, and O from all cavity treatments that had SIMS measurements taken. The profiles are grouped by impurity species and by those that had anti-Q-slope versus those that did not. All treatments that resulted in anti-Q-slope have several key features in common. For these treatments, the O concentration at the surface was consistently above ~1 at.%, the C concentration varied significantly (~0.2−9 at.%) at the surface from treatment to treatment, and the N concentration were consistently below the typical values (~0.09−0.4 at.%) seen in N-doped cavities. These trends indicate that O plays the primary role in the appearance of anti-Q-slope, which is reinforced by findings made by Lechner [Lec21], the strength of the drop in R_{BCS} is insensitive to the variation of the concentration of C at the surface but may still depend on the concentration of C to an extent, and that N does not seem to have a significant role in the field dependence of R_{BCS} for infusion treated cavities.

The chemical etching performed after these infusion treatments showed that

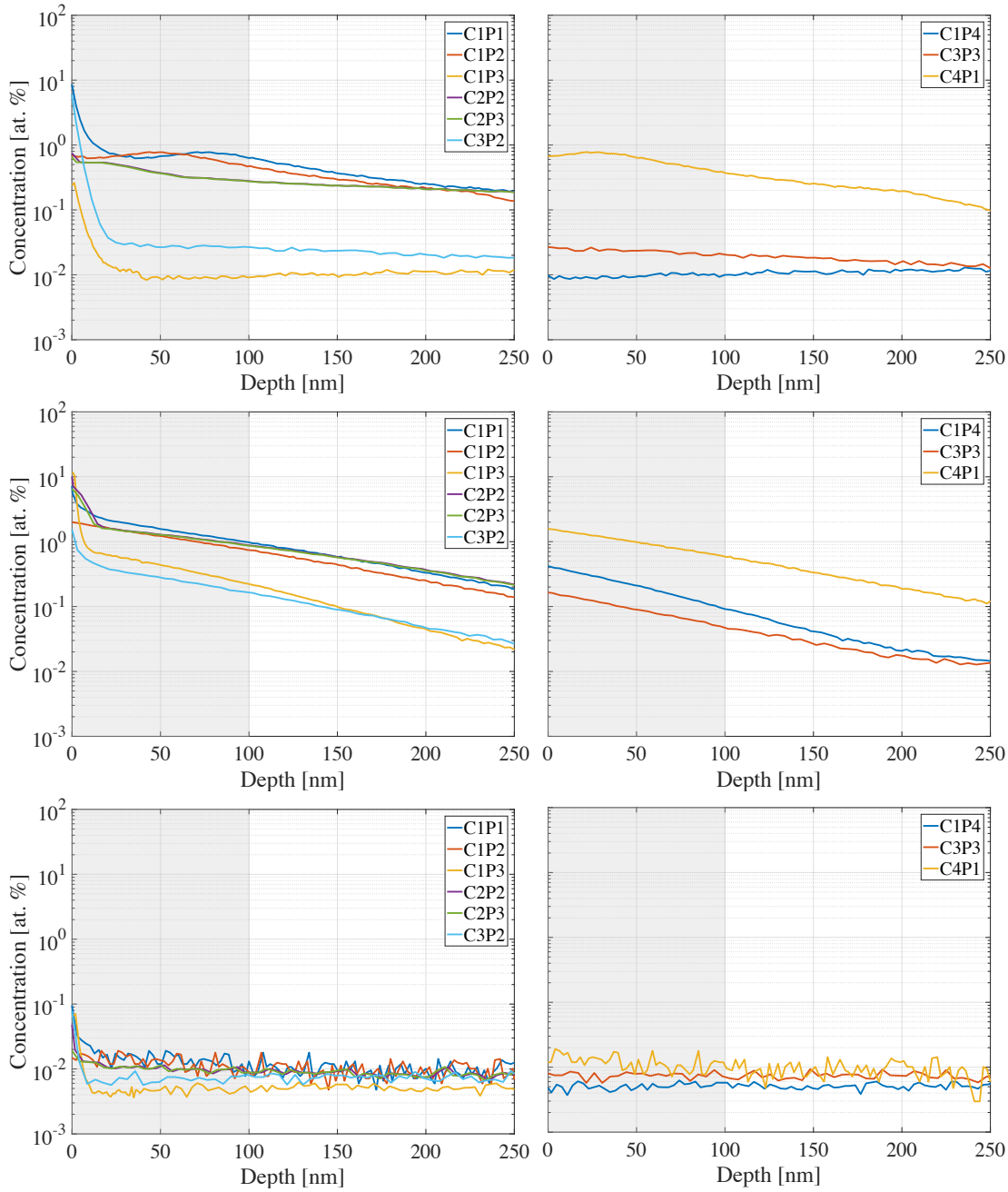

Figure 5.11: C (**top**), O (**middle**), and N (**bottom**) concentration profiles for the cavity treatments that resulted in anti-Q-slope (**left**) and those that did not (**right**).

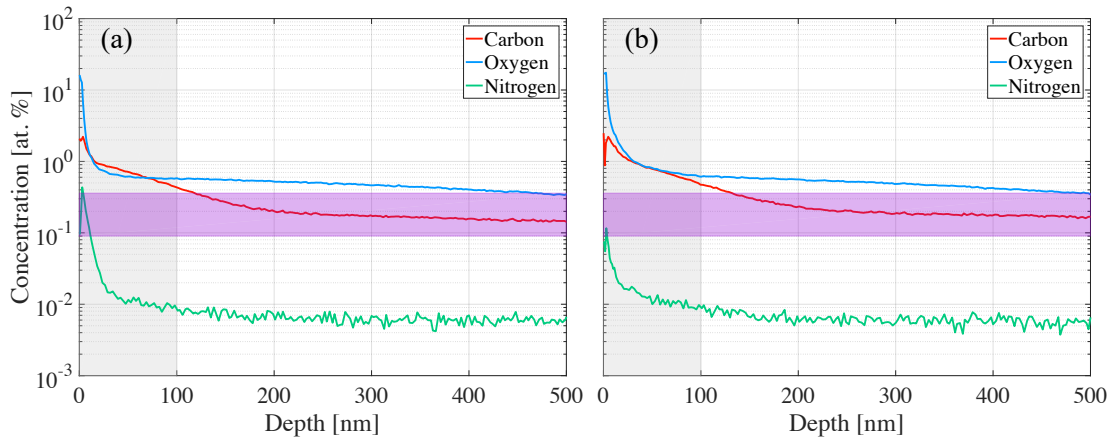

Figure 5.12: Comparison of SIMS measurements done on two different spots on an N-infused fine-grain niobium sample.

the area of interest lies between 5–50 nm into the surface. In other words, the content of the near surface chemistry ($\lesssim$ 50 nm) is incredibly important for producing cavities with anti-Q-slope. It is important to note, however, that the amount of etching required to completely destroy the anti-Q-slope depends on the exact recipe used. For example, cavities with longer infusion or post-infusion anneal times would require more etching to get rid of the anti-Q-slope.

Finally, it is worth discussing the limits of the SIMS data presented in this chapter. For example, SIMS data taken at two different spots on a fine-grain sample that received a nitrogen infusion treatment are shown in Figure 5.12. There is significant variation in the N concentration at the surface, and to a lesser extent the C concentration, for the two sets of measurements. This variation may be less significant for large-grain or single crystal samples, where effects due to grain boundaries do not come into play. It is also unknown to what degree crystal orientation may effect the results. Therefore, when drawing conclusions from SIMS measurements such as those shown here it is important to take into account the possible variation of concentration profiles from spot to spot on a single sample or from sample to sample treated under the same conditions and

to be careful when quoting exact concentration values.

CHAPTER 6

HIGH FREQUENCY EXPERIMENTAL APPARATUS

This chapter will cover the design and commissioning of experimental apparatus to perform electropolishing (EP), high pressure rinsing (HPR), and RF testing of high frequency (3.9 and 5.2 GHz) cavities. Since the linear dimensions of a cavity scale inversely with cavity frequency [PKH08], these higher frequency cavities are much smaller than the standard 1.3 GHz cavities that are more commonly used. The established EP, HPR, and test insert systems are optimized for 1.3 GHz cavities so new systems needed to be designed that are instead optimized for the smaller, higher frequency cavities. For example, the diameter of the beam tubes on these cavities are too small to fit on the current HPR system so the new system had to have a much smaller nozzle that can fit inside the cavity. The older test inserts have forward power coupler designs that were incompatible with the new cavities and, therefore, an entirely new system was needed. This chapter will first discuss the EP system, followed by the HPR system and the RF test insert. Next, the design and electromagnetic simulation results of a new coupler system for the 3.9 and 5.2 GHz cavities will be discussed. To conclude the chapter, the construction and commissioning of the high frequency test insert will be reviewed.

6.1 Electropolishing System

Cavity surface treatments begin with an electropolish (EP) of the interior surface followed by vacuum baking. The EP process will typically be used to remove 1 – 150 μm of material from the surface. This is done for several reasons.

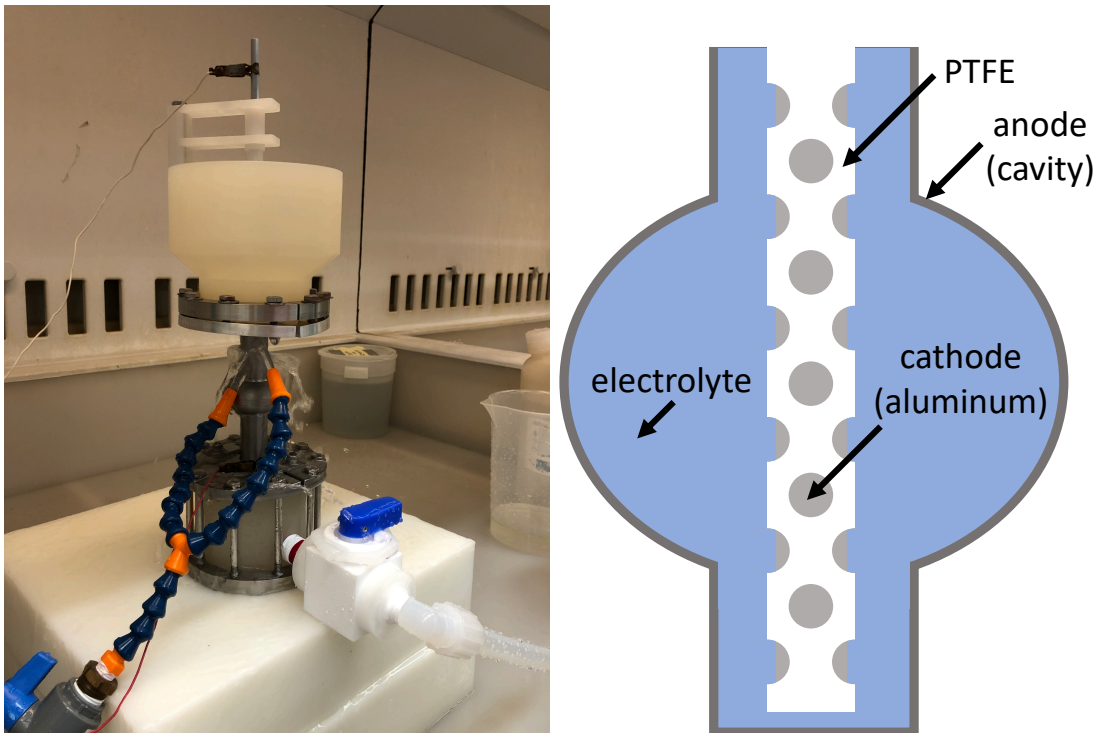

Figure 6.1: Electopolishing setup for the 3.9 and 5.2 GHz cavities with a 5.2 GHz cavity installed (**left**) and diagram of the cavity filled with electrolytic solution with aluminum anode and PTFE sleeve installed (**right**).

Namely, to smooth the surface which reduces field enhancement at sharp edges or protrusions [PKH08], to remove previously treated surfaces, or to remove the damaged layer from cavity fabrication. This essentially resets the cavity surface allowing a single cavity to undergo many treatments and tests over its lifetime. An EP system was developed for the smaller 3.9 GHz (CTE) and 5.2 GHz (QTE) cavities. The new EP setup with a 5.2 GHz cavity installed is shown in Figure 6.1.

The cavity sits vertically on a cylindrical PTFE base that is used to drain the EP solution after a run is finished. A PTFE cup sits on top of the cavity to hold excess solution to ensure the entire interior surface is submerged. A pure aluminum rod (cathode) is inserted into the length of the cavity (anode) centered parallel to its beam axis. A slotted PTFE sleeve surrounds the cathode to

Table 6.1: Typical Electropolish Parameters for 3.9 and 5.2 GHz Cavities

Parameter	**Typical Value (CTE)**	**Typical Value (QTE)**
Anode Voltage	11–13 V	11-13 V
Electrolyte Temperature	12–19 °C	12–19 °C
Current	1–2 A	0.6–1.6 A
Cavity Surface Area	20 cm^2	13.2 cm^2
Material Removal	2–100 μm	2–100 μm

prevent hydrogen bubbles formed on the cathode during the EP process from diffusing towards the cavity as they rise to the electrolyte's surface. Cooling lines spray chilled water onto the exterior cavity surface to keep the acid temperatures below 19 °C. A diagram showing a cross section of teh cavity filled with the electrolytic acid solution and aluminum cathode and PTFE sleeve is shown in Figure 6.1.

The electrolytic acid solution consists of a 10:1 volume ratio of 98% H_2SO_4 and 48% HF acid. The applied negative voltage on the cathode produces a current of negatively charged electrons and oxygen flowing towards the niobium anode and positively charged hydrogen towards the aluminum cathode. Reactions on the anodic surface result in the growth of the niobium pentoxide layer, Nb_2O_5, whereas the reactions on the cathodic surface produce hydrogen gas, H_2 [Pad09]. The HF then dissolves the pentoxide into soluble $NbOF_5$ or NbF_5. The oxide is then regrown on the exposed Nb surface by the H_2SO_4 resulting in a cyclic process of oxide growth and dissolution [Pad09]. This cyclic process is repeated until the desired amount of material removal is achieved. The typical values of the parameters used during an EP are shown in Table 6.1.

To calculate the thickness of the material removed from the cavity surface, the total charge accumulated during the polish must first be obtained by inte-

grating the current over the duration of the polish:

$$Q = \int I(t)\, dt. \tag{6.1}$$

Once the total charge accumulated is acquired, the following formula is used to calculated the thickness, d, of niobium removed

$$d = \frac{m_{\mathrm{Nb}} Q}{\rho_{\mathrm{Nb}} A e N_e} \tag{6.2}$$

where m_{Nb} is the atomic mass of niobium, ρ_{Nb} is the density of niobium, A is the surface area of the cavity surface, $N_e = 5$ is the number of valence electrons per niobium atom, and e is the fundamental charge.

After an EP is complete, the acid solution is drained and the cavity is rinsed four times with ultra-clean deionized (DI) water and once with methanol. The cavity is then rinsed in an ultrasonic with DI and detergent (Liquinox) at 65 °C for 30 min followed by a DI rinse and an additional ultrasonic in DI water at room temperature for 30 min. At this point the cavity is ready to be transported to the clean room for a high pressure rinse with DI water and assembly onto an RF test insert.

6.2 High Pressure Rinsing System

Before cavities can be assembled onto the test insert, they must undergo one or more high pressure rinses with filtered de-ionzed water to remove any surface contamination such as dust or debris. This is done because even the smallest particulate contamination on the surface can lead to field emission, multipacting, quenches at low fields, and general cavity performance degradation [PKH08].

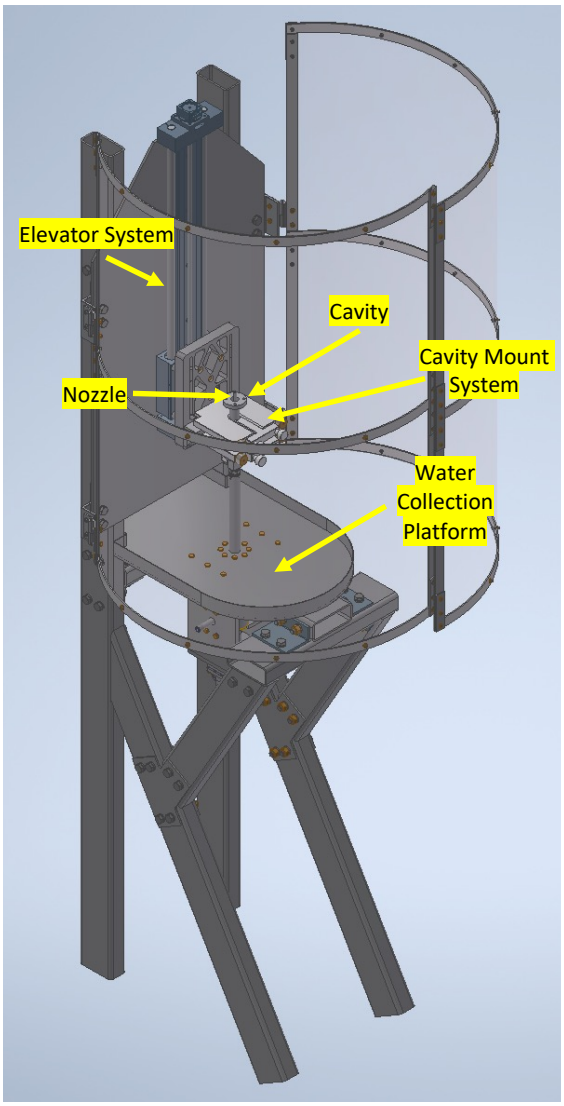

Figure 6.2: Model of the high pressure rinsing system for the high-frequency 3.9 and 5.2 GHz single-cell cavities.

The entire high pressure rinsing (HPR) system model is shown in Figure 6.2. The HPR sits in a Class 10 (ISO 4) cleanroom to prevent airborne particulates from contaminating the cavity surface before, during, and especially after the rinse. The cavity is mounted vertically, typically with the cavity top plate installed, on an electronically controlled elevator system which allows the cavity to be slowly raised and lowered during a rinse. The nozzle and stem is situated on a platform that collects and drains excess water. The nozzle is connected

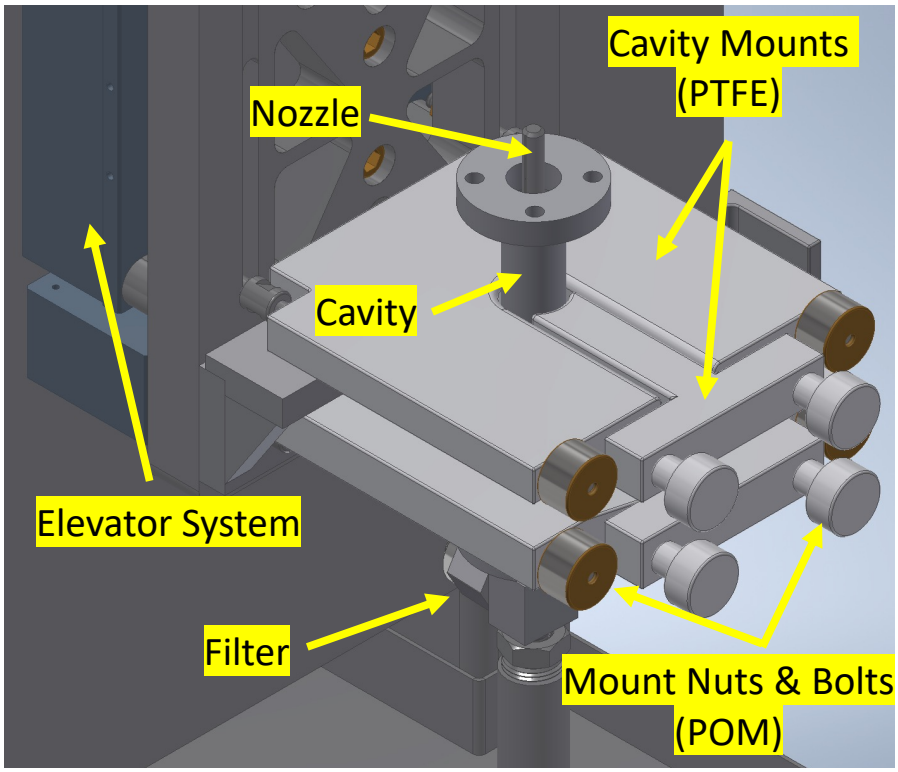

Figure 6.3: Cavity mount of the 5.2 GHz single-cell cavity high pressure rinsing system.

to an electric motor underneath the platform that allows the user to control its rotation speed. The rotation of the nozzle and the vertical motion of the cavity prevent the high pressure (750 psi) jet streams from sitting at a particular spot on the cavity surface for too long. This ensures that the high pressure stream will not erode the niobium or contribute to oxide growth.

The cavity mounting system consists of two polytetrafluoroethylene (PTFE) plates and tee inserts to both mount and center the cavity beam axis with the nozzle, as shown in Figure 6.3. The plates are attached to the back mount by threaded rods and polyoxymethylene (POM) nuts. Likewise, the tee inserts mount to the plates with a set POM bolts. The mounting system was made from PTFE and POM because these materials typically produce less particulates during cavity removal than the more commonly used steel or aluminum mounts.

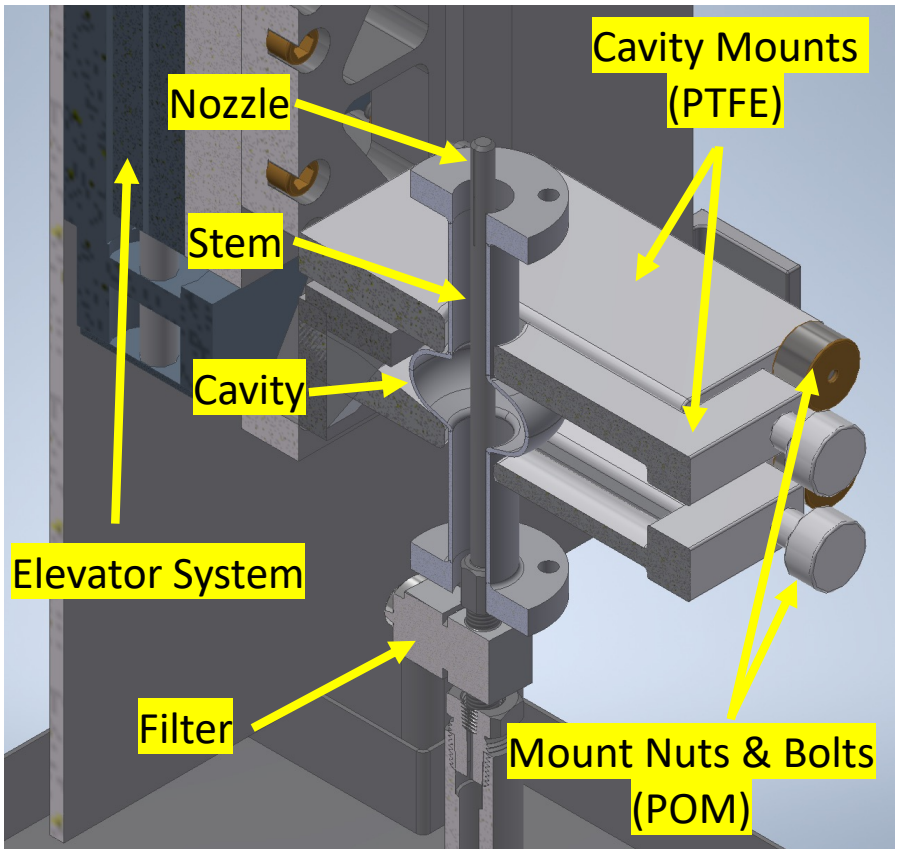

Figure 6.4: Cross-section of the 5.2 GHz single-cell cavity high pressure rinsing system.

Also, particulates from this mounting system are far less likely to become field emitters during cavity testing than metallic particulates if they make their way onto the cavity surface. For reference and clarity, a cross sectional view of the HPR system is shown in Figure 6.4.

A typical HPR run consists of 2.5 passes where one pass is defined as the transversal of the nozzle from one cavity flange to the other and lasts approximately 15 to 20 min. After the rinse is complete, the HPR system is turned off and the cavity is lifted far enough away from the nozzle to make removal efficient and convenient. The cavity will then sit undisturbed for approximately 24 hr to dry. Once dry, the bottom flange of the cavity is covered with cleanroom-

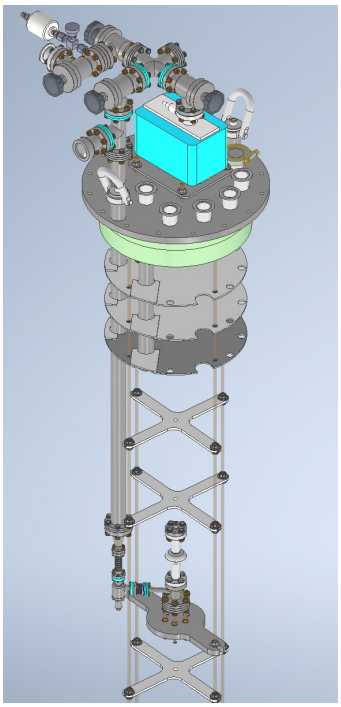

Figure 6.5: Full design of the HF insert.

grade plastic that is wiped down with methanol and secured with ultra-high vacuum aluminum foil to prevent and reduce particulates from entering the interior cavity volume. The cavity is them dismounted from the system and taken to an adjacent room in the cleanroom (Class 100) to be mounted on the test insert. The mounting of the cavity on the insert and the insert design will be discussed in the following section.

On a final note, it is important to mention that only the 5.2 GHz cavity and mount system was shown here for the sake of brevity. The 3.9 GHz setup is nearly identical with the only difference being the modified geometry of the of the PTFE mounting plates to account for the larger beam tube diameter and longer cell length.

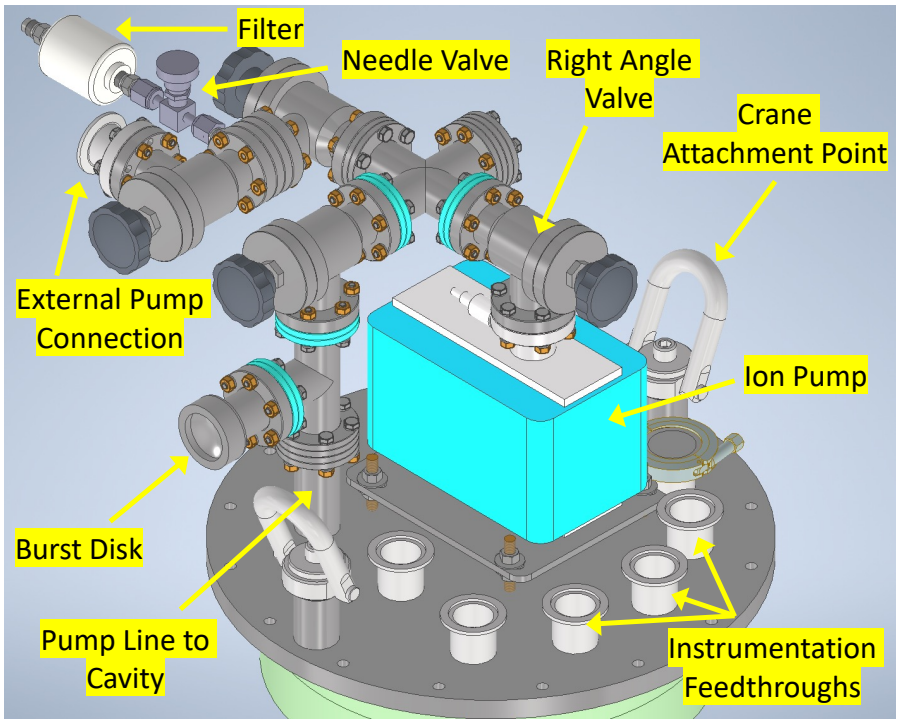

Figure 6.6: Design of the top plate assembly of the HF insert.

6.3 Test Insert Design

After receiving a final HPR, the cavity is installed on the high frequency (HF) test insert. The insert is the apparatus that is placed into the cryogenic dewar for RF testing. As discussed in the introduction, the HF insert was designed and optimized for use with the 3.9 and 5.2 GHz cavities. The full insert design is shown in Figure 6.5.

The insert top plate separates the air side from the cryogenic side of the test dewar and is shown in Figure 6.6. The vacuum piping on the top plate allows the cavity to be actively pumped on after initial installation and during testing. A filtered needle valve is included to allow the cavity to be let-up in the clean room after testing is complete. After initial installation in the clean room, the right-angle valve port connected to the needle valve is used to do a slow pump

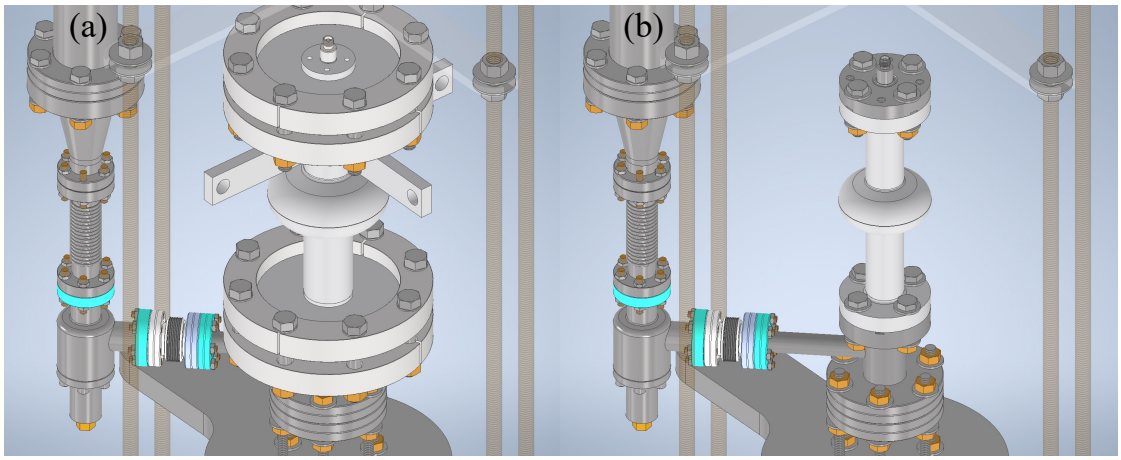

Figure 6.7: Close-up of the pump line, cavity, and coupler section of the HF insert for the 3.9 and 5.2 GHz cavities.

down with a roughing and turbo-pump stand. During testing, the ion pump (large green rectangular box on the top plate) is used to maintain vacuum and to identify small cryogenic leaks. A minimum of four right-angle valves are assembled in the vacuum system in such a way that either the cavity or the ion pump can be pumped on with an external turbo-pump should the need arise. Two shackles are welded to the top plate and are used to connect a 10-ton overhead crane to the insert so that it can be lifted in and out of the test dewar. Six K-flange feedthroughs are welded to the top plate to pass through instrumentation, a helium transfer line, and a helium pumping line.

The vacuum line runs all the way down to the cavity where it undergoes a diameter reducing-transition connected in series to a bellow, right angle valve, and another smaller bellow. The final bellow then connects to the coupler tee of the cavity-coupler system. The cavity sits vertically atop the coupler tee. The coupler tee and feedthrough connect to the coaxial forward power transition line via an N-type connecter. The cavity top plate has a small pick-up probe that connects to the transmitted power line. A close-up of the both 3.9 and 5.2

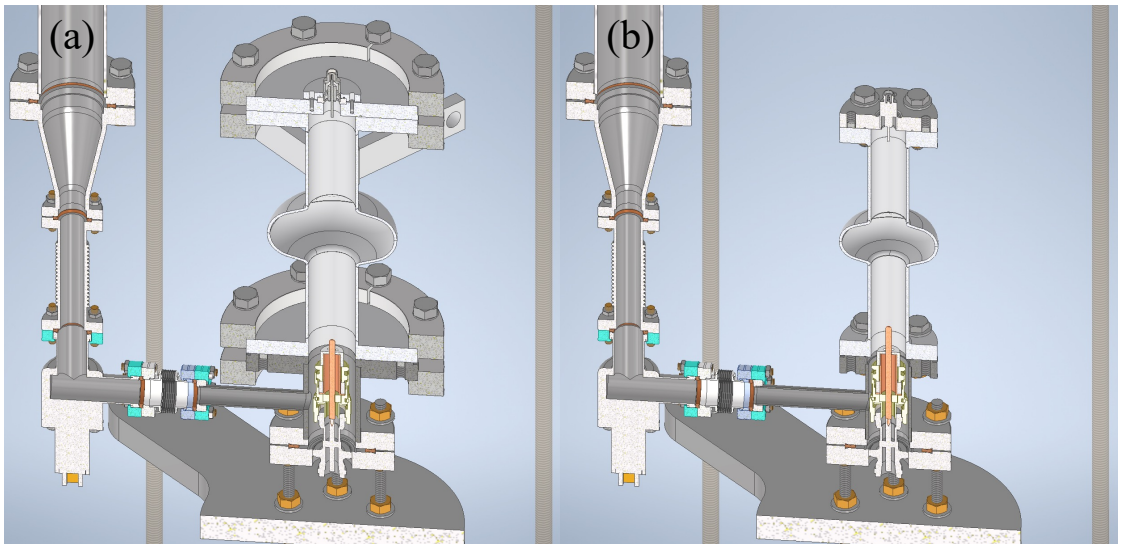

Figure 6.8: Cross-section of the 3.9 and 5.2 GHz single-cell cavity insert coupler section.

GHz cavities installed on the cavity-coupler-pumping line section of the insert is shown in Figure 6.7. Additionally, a cross sectional view is provided in Figure 6.8. This view shows the interior cavity volume and the arrangement of the coaxial coupler system in relation to the cavity.

The coupler tee and feedthrough is secured to a base plate which, in turn are connected to silicon-bronze load-bearing support rods that connect to the underside of the insert top plate. Due to stability issues, several aluminum cross-bar supports are used to connect the four support rods to provide additional rigidity and reduce vibrational motion of the cavity during transport from the clean room to the cavity testing area.

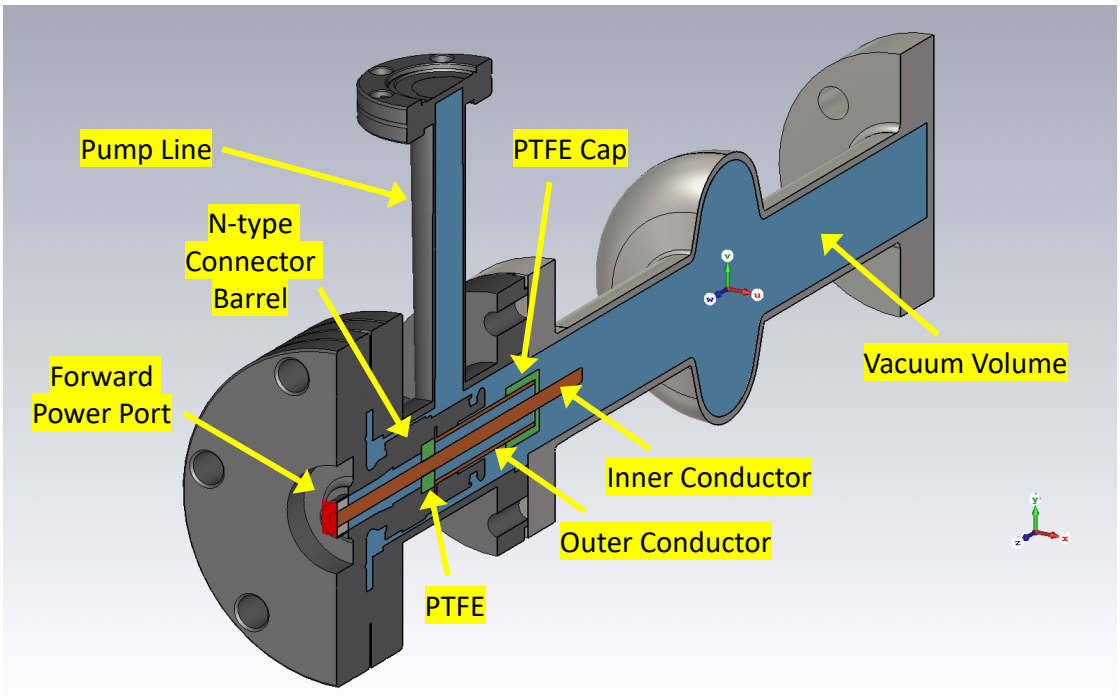

Figure 6.9: Cavity and coupler 3D model geometry for the 5.2 GHz QTE series cavity.

6.4 Coupler Design and Simulations

Electromagnetic modeling via finite element analysis is an extremely important step in the process of cavity-coupler design. Simulations allow the designer to find the optimal coupler geometry for the desired external quality factor, Q_{ext}, for the cavity resonant mode, the resonant frequencies and Q_{ext} of coupler modes, and S-parameters of the input coupler.

The Eigenmode Solver of CST Studio Suite® 2019 [CST] was used to calculate the resonant frequencies and Q_{ext} of the cavity and coupler modes whereas the Frequency Domain Solver was used for coupler S-parameter calculations. Two cavity-coupler models were created and simulated in this fashion. Both cavity models are of the same geometry but one is a scaled down version of the other. The CTE model is a single-cell elliptical cavity with a nominal frequency

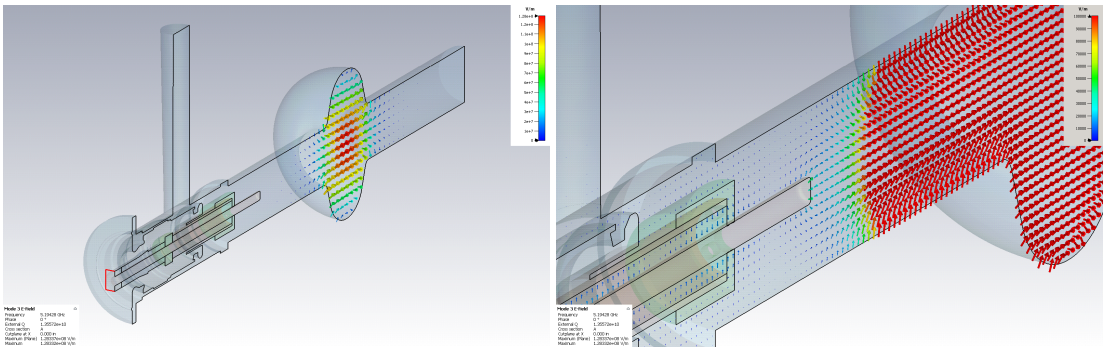

Figure 6.10: **Left:** Cavity electric field projected on the $x = 0$ symmetry plane for the TM_{010} mode. **Right:** Close up of the field in area between the coupler and cavity.

of 3.9 GHz whereas the QTE model is the scaled-down version with a nominal frequency of 5.2 GHz. The primary differences between the two models are the cavity size, coupler length, and inner diameter of the coupler tee (i.e., bore of the housing for the coupler). These differences are minute, however, and do not significantly alter the qualitative features of the discussion below. Hence, the main focus will be on the QTE model which is shown in Figure 6.9.

The coupler designed for these experiments are of the coaxial variety with a solid inner conductor made of high purity copper centered on and parallel to the cavity beam axis and a shorter concentric copper outer conductor. The coupler dimensions were chosen to get as close to an impedance of 50 Ω while also facilitating ease of fabrication. A PTFE cap is used to center the two conductors. The coupler is connected to the coupler feedthrough plate via a N-type coaxial barrel. A single side-port provides a vacuum line for active pumping on the cavity-coupler volume during preparation and testing.

In Figure 6.9, the coupler is colored orange, the cavity light gray, the coupler feedthrough assembly dark gray, PTFE components white and light green, and vacuum volume light blue. The highlighted red surface is the input port for the

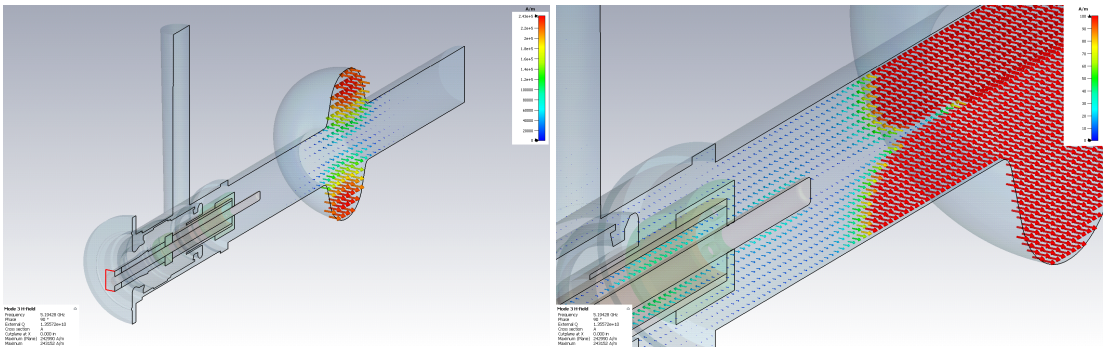

Figure 6.11: **Left:** Cavity magnetic field projected on the $x = 0$ symmetry plane for the TM_{010} mode. **Right:** Close up of the field in area between the coupler and cavity.

excitation signal in the simulations. From this point onward, only field distributions of the QTE model will be shown as the distributions for the CTE model are qualitatively very similar.

6.4.1 Eigenmode Simulations

The Q_{ext} for both designs was chosen to have a value between 1×10^{10} and 1.5×10^{10} so that for the estimated cavity quality factor Q_0 ranging from 1×10^8 (4.2 K) to 1×10^{10} (1.6 K) the coupling factor $\beta = Q_0/Q_{ext}$ would approximately lie in the range from 0.01 to 1 so that the cavity would remain on the under coupled side to prevent coupler losses stemming from over coupling.

The electric and magnetic fields for the QTE cavity fundamental transverse magnetic mode (TM_{010}) are shown in Figure 6.10 and Figure 6.11, respectively. Boundary conditions require that the electric field is perpendicular to the conducting walls of the cavity. Along the beam axis, the field is parallel (i.e. only in the z-direction) and is at a maximum at the center of the cavity. The magnetic field, on the other hand, vanishes along the beam axis and curls around

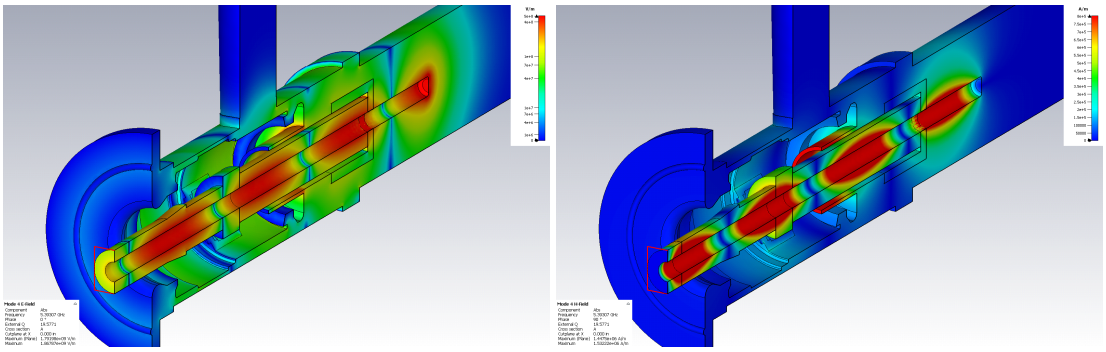

Figure 6.12: Surface electric field (**left**) and magnetic field (**right**) for a standing wave 'inner' coupler mode for the QTE cavity-coupler design with resonance frequency $f = 5.393$ GHz and $Q_{\text{ext}} \approx 20$.

in the azimuthal direction as seen in Figure 6.11. Boundary conditions for the magnetic fields demand that it is strictly parallel to the conducting walls. The simulated resonance frequency of this mode is 5.194 GHz. As a note, the actual resonance frequency of a cavity can somewhat deviate from its design value due to tolerances in the fabrication process and also by the amount of chemical etching the interior surface receives.

The eigenmode analysis surveys the coupler modes above and below cavity resonance. This is a precautionary measure to ensure none of the coupler modes overlap with or are too close to the cavity mode. If a coupler mode is too close to cavity resonance, a non-negligible amount of incoming power that would go to supplying the cavity would instead by diverted to the coupler resonance. Overlap of modes is highly undesirable and is avoided as much as possible. If the designer is unfortunate enough to find a coupler geometry with the desired Q_{ext}, but with significant mode overlap, the coupler design would need to be reevaluated. In actual practice, sending power into an overlapping coupler mode can create a myriad of issues such as significant coupler losses through resistive dissipation, heating, outgassing, arcing, and cavity vacuum degradation [PKH08]. This is why a good coupler design is of particular importance.

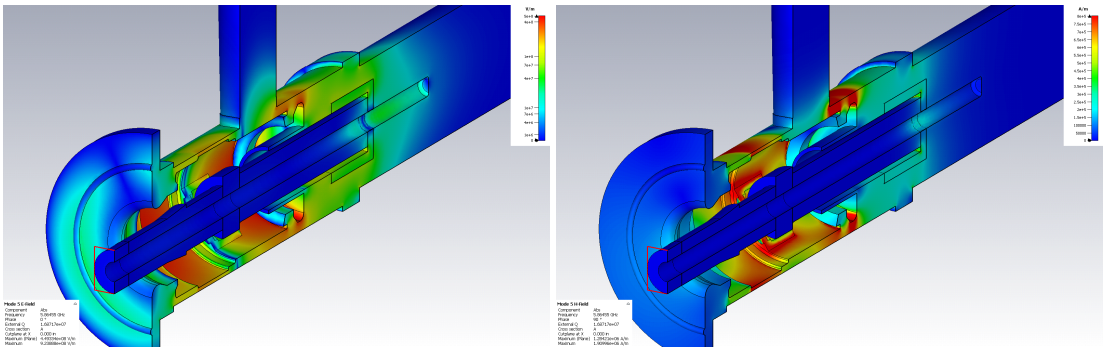

Figure 6.13: Surface electric field (**left**) and magnetic field (**right**) for a standing wave 'inner' coupler mode for the QTE cavity-coupler design with resonance frequency $f = 5.865$ GHz and $Q_{\text{ext}} \approx 1.7 \times 10^7$.

An example of the surface electric and magnetic fields of a coupler mode for the QTE model is shown in Figure 6.12. Here, the electric field is directed radially from the inner conductor and the magnetic field curls azimuthally around it. This particular mode has a resonance frequency of 5.393 GHz with $Q_{\text{ext}} \approx 20$. Because the fields are concentrated primarily in the region between the inner and outer conductor of the coupler, this mode is referred to as an *inner* coupler mode. Figure 6.13 shows the surface electric and magnetic fields for an *outer* mode, where as one would correctly guess, the fields are concentrated between the outer conductor of the coupler and the inner wall of the feedthrough housing. In this case, the mode frequency sits at 5.865 GHz with $Q_{\text{ext}} \approx 1.7 \times 10^7$. Both of these modes, although undesirable, occur far enough away from cavity resonance as to not pose a significant problem for cavity testing. The results of the eigenmode analysis for both models are summarized in Table 6.2.

6.4.2 S-Parameter Simulations

The cavity-coupler system can be considered a generalized two-port network where port 1 (i.e. red square in Figure 6.9) is the coupler feedthrough that con-

Table 6.2: CST Studio Suite Eigenmode and S-Parameter Simulation Results

Model	**Frequency [GHz]**[1]	**Est. Frequency [GHz]**[2]	**% Diff**[3]	**External Q**
CTE	2.912	—	—	8.59
CTE	3.898[4]	—	—	1.96×10^{10}
CTE	4.149	4.145	0.10	1.03×10^{3}
CTE	4.449	4.445	0.09	2.86×10^{5}
CTE	4.517	4.513	0.09	1.48×10^{4}
CTE	4.658	4.636	0.47	16.80
QTE	4.614	4.598	0.35	2.23×10^{4}
QTE	4.709	4.692	0.36	8.20×10^{3}
QTE	5.194[4]	—	—	1.36×10^{10}
QTE	5.393	5.384	0.17	19.58
QTE	5.865	—	—	1.68×10^{7}
QTE	5.949	—	—	5.39×10^{7}

[1] Obtained from eigenmode simulations
[2] Estimated from peaks in S-parameter simulations
[3] Percent deviation between eigenmode frequency and estimated frequency
[4] Cavity fundamental TM_{010} mode.

nects the cavity-coupler system to a forward power cable. The end of the coupler can be taken to be port 2 of the network, but this fact will be largely irrelevant for the following discussion. With the system defined this way, the power flowing into the system would be the forward power P_f and the power flowing out of the system would be the reverse power P_r. Then the quantity of interest is the scattering parameter S_{11} which is a measure of the ratio of the reverse to forward power and is given by [Poz12]

$$S_{11} = 10 \text{ dB } \log_{10}(P_r/P_f) \tag{6.3}$$

in units of decibels. Qualitatively, if the same amount of power is flowing into and out of the system, $S_{11} = 0$ dB. The same is true if all of the forward power is simply reflected. However, when the reverse power is less than the forward

power, $S_{11} < 0$ dB. This occurs primarily when forward power is fed into a resonant mode thus reducing the reverse power.

The purpose of the simulations is to obtain the S-parameter as a function of input signal frequency, f. This offers a second, independent method of predicting at what frequencies resonant modes will occur. It is more insightful to reframe S_{11} in terms of the coupling factor β or in terms of Q_0 and Q_{ext}, the intrinsic and external quality factors, respectively. Considering the relation between forward and reverse power and the coupling factor [PKH08],

$$\frac{P_r}{P_f} = \left(\frac{\beta - 1}{\beta + 1}\right)^2, \tag{6.4}$$

and coupling and quality factor, $\beta = Q_0/Q_{\text{ext}}$, the expression in Equation 6.3 becomes

$$S_{11} = 20\log_{10}\left(\frac{\beta - 1}{\beta + 1}\right) = 20\log_{10}\left(\frac{Q_0 - Q_{\text{ext}}}{Q_0 + Q_{\text{ext}}}\right). \tag{6.5}$$

Now it is more clearly seen that the depth of a resonance depends on β. The closer to unity β is, the deeper the resonance. This means $Q_0 \approx Q_{\text{ext}}$ for deep resonances. For weak resonances, $\beta \ll 1$ ($Q_0 \ll Q_{\text{ext}}$) or $\beta \gg 1$ ($Q_0 \gg Q_{\text{ext}}$) and $S_{11} \approx 0$ dB. The width of a resonance depends on the loaded quality factor Q_L which is related to Q_0 and Q_{ext} by [PKH08]

$$\frac{1}{Q_L} = \frac{1}{Q_0} + \frac{1}{Q_{\text{ext}}}, \tag{6.6}$$

where the smaller of Q_0 and Q_{ext} dominates due to the reciprocal dependence. The full-width half-maximum, Δf, then is given by [PKH08]

$$\Delta f = \frac{f_0}{Q_L}, \tag{6.7}$$

where f_0 is the resonant frequency of the mode. The reason that cavity resonance is essentially invisible over large frequency ranges is because both Q_{ext}

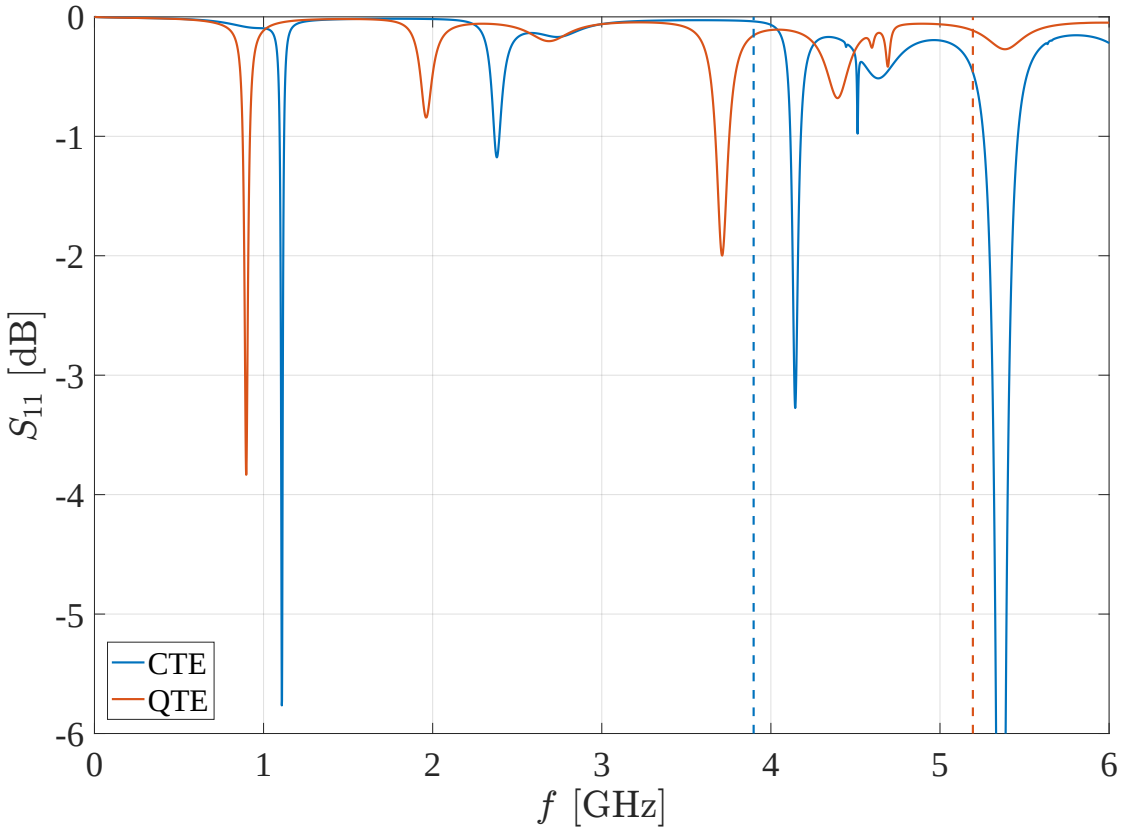

Figure 6.14: CST Studio Frequency Domain Solver simulation of S_{11} as a function of f for the CTE (3.9 GHz) and QTE (5.2 GHz) cavity-coupler models. The dashed vertical lines correspond to the cavity resonant frequencies for the TM_{010} mode.

and Q_0 are very large resulting in a very large Q_L and, in turn, a very narrow Δf. Conversely, for coupler resonances with very low Q_{ext}, $Q_L \approx Q_{\text{ext}}$ and Δf is broad and visible.

The simulations were done for both the CTE and QTE models using the Frequency Domain Solver in CST Studio using over 1000 independently simulated points. As mentioned previously, the resonance peaks in the simulated curves should match the resonant frequencies of the coupler modes, providing a consistency check. In addition, it provides a rough quantitative estimate for the attenuation of the forward power in the vicinity of cavity resonance. If a cou-

pler mode is too close to cavity resonance, an appreciable fraction of the forward power will go to the coupler resonance rather than the cavity mode. The simulated curves are shown in Figure 6.14 and the resonant frequencies estimated from these curves for several coupler modes in Table 6.2. Due to resolution limits, the depth of the peaks in the S_{11} curve are more qualitative than quantitative. Likewise, for peaks corresponding to modes with high Q_{ext} and Q_0, the peaks may be too narrow to see in Figure 6.14. Of those peaks that could be determined, the resonant frequency was estimated by finding the lowest point in the peak. These estimated values are shown next to the frequencies calculated from the eigenmode simulations in Table 6.2. The percent difference for these estimated frequencies were all below 0.5 % resulting in excellent agreement between the two simulation methods.

6.5 Commissioning

This section will discuss the commissioning of the high frequency (HF) insert system and show results from a preliminary RF test of a 5.2 GHz cavity. The fully commissioned insert is shown in Figure 6.15 with a 5.2 GHz cavity installed in the process of being dressed with the necessary instrumentation required for an RF test.

The pit pump line is used to pump on the helium in the dewar to cool down from 300 K to the testing range of 4.2 to 1.6 K. Three layers of aluminum sheets and two layers of styrofoam hang from the bottom of the top plate and act as thermal shields to prevent heat leak from the air side of the top plate into the dewar. This significantly slows down the rate of helium boil-off due to heat

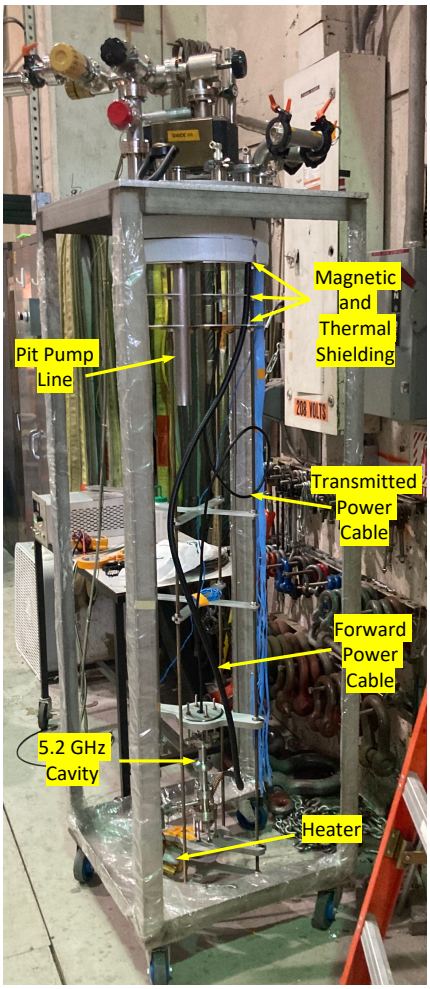

Figure 6.15: HF insert

leak. A single layer of magnetic shielding metal sits on top of the lowest aluminum heat shield to prevent external magnetic fields from making their way into the dewar volume and reaching the cavity. Power is supplied to the cavity by the forward power cable while the transmitted power cable samples the power in the cavity. The instrumentation not shown in Figure 6.15 include the helium level stick, temperature sensors, and magnetic field sensor (fluxagte). Three temperature sensors are used with one on the top iris of the cavity, one on the cavity equator, and one on the bottom iris. This configuration allows for the measurement of the temperature of the helium bath and the temperature

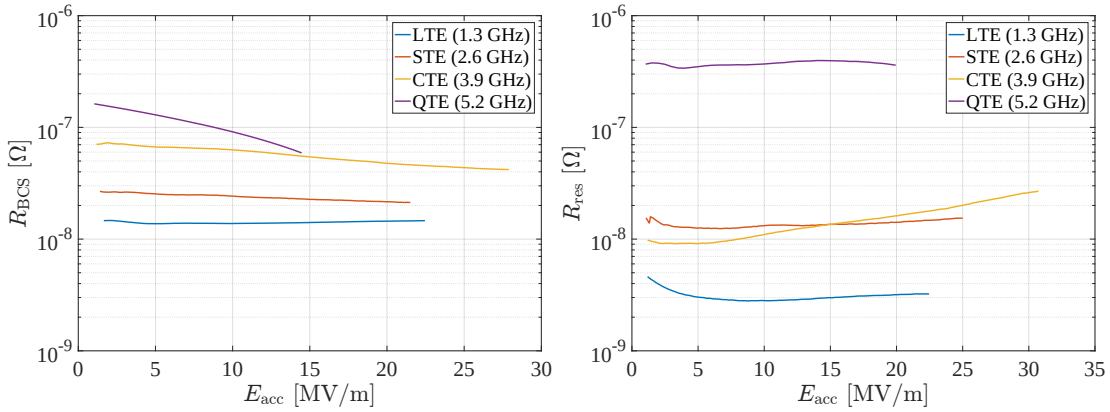

Figure 6.16: **Left:** BCS resistance as a function of accelerating field at 2.0 K. **Right:** Residual resistance as a function of accelerating field. The standard bake preparation was used for all cavities shown.

gradient across the cavity cell during the normal-superconducting transition. The fluxgate is attached to the cavity equator and measures the magnetic field in the vertical direction. This allows the operator to monitor the magnetic fields during transition as well as calculate the amount of flux expulsion from the cavity during a transition [PCC+16]. The helium level stick measures the height of liquid helium in the dewar which allows the operator know when the cavity becomes uncovered and is no longer being properly cooled by the helium bath. Finally, a small 100 W heater hangs from the bottom cavity support plate to boil off the remaining liquid helium in the dewar after an RF test is complete.

Data from a preliminary test of a 5.2 GHz cavity using the HF insert is shown in Figure 6.16 alongside data from tests on 1.3, 2.6, and 3.9 GHz cavities. The standard bake preparation was used for all four cavities. As can be seen, the residual resistance at 5.2 GHz was extremely high. The exact cause of the high residual resistance is currently unknown and additional testing and diagnostic measurements would need to be completed to diagnose the issue. It is likely, however, that the source was not intrinsic to the cavity as several tests with two different 5.2 GHz cavities yielded extremely similar results. This points

to possible issues such as small helium leaks in insert vacuum seals at cryogenic temperatures leading to arcing inside the coupler-cavity system, a damaged coaxial cable or connector somewhere along the test system path, or issues with coupler alignment causing extremely high electric fields that lead to additional losses in the coupler. After each test was completed, the coupler was examined and showed signs of oxidation which usually points to arcing issues or contaminate gases such as helium making their way into the cavity vacuum system. Despite these relatively minor challenges, complete data sets were obtained in most cases providing evidence that HF insert is operational and can be used to test 3.9 GHz and 5.2 GHz cavities.

Future work for this insert would entail diagnosing and fixing the issues leading to high residual resistances, designing and commissioning a Helmholtz coil to perform magnetic flux trapping experiments [Gon16a] to study the sensitivity of the surface resistance to trapped flux at higher frequencies, and creating new coupler systems for even higher frequency cavities.

6.6 Conclusion

In this chapter, the design and commissioning of high frequency apparatus to perform chemistry, high-pressure rinsing, and RF testing was discussed. Also, the design and electromagnetic simulation results of new coupler systems for use on the high-frequency insert for 3.9 and 5.2 GHz cavities was shown. The purpose of this chapter was to showcase the infrastructure that was added to the Cornell SRF laboratory to test cavities of up to 6 GHz.

CHAPTER 7

FIELD AND FREQUENCY DEPENDENCE STUDIES

The aim of this chapter is to introduce a model that predicts the optimal resonant frequency, helium bath temperature, and accelerating field to minimize the cryogenic power required to maintain cavities at these values. The theoretical background will first be introduced followed by the methods of data analysis and modeling, and, finally, the results of the model as well as the ranges used for the field, frequency, and temperature.

7.1 Theoretical Background

This section introduces the theoretical background necessary for understanding how the numerical model and simulations presented in the next section work. An expression for the power dissipated by a cavity per unit beam energy is derived followed by a short discussion on cavity surface resistance. Finally, this section is ended by a derivation relating the dissipated power to the 'real-world' cryogenic power.

Accelerator physicists and engineers know the target beam energy before accelerator design is started. Thus, the decision to normalize to units of beam energy was very deliberate with that hope that the results obtained herein could be used to quickly and easily calculate the required cryogenic power for a given beam energy.

7.1.1 Dissipated Power

The power dissipated by a cavity (or string of cavities) is related to the accelerating voltage V_{acc} and the cavity shunt impedance R_{sh}

$$P_{\text{diss}} = \frac{V_{\text{acc}}^2}{R_{sh}} \tag{7.1}$$

where the accelerator definition of P_{diss} has been shown rather than the circuit theory definition which differs by a factor of 1/2 [PKH08, Wan08]. The shunt impedance can be recast in a form which is dependent only on cavity geometry by dividing by the cavity quality factor Q_0

$$P_{\text{diss}} = \frac{V_{\text{acc}}^2}{(R_{sh}/Q_0)_{\text{total}} Q_0}. \tag{7.2}$$

The subscript 'total' is used to indicate that, in general, a multi-cell is considered and $(R_{sh}/Q_0)_{\text{total}}$ represents that value of the normalized shunt impedance for the entire multi-cell cavity. If the cavity has N cells, then the length of the cavity $L = N(\lambda/2)$ where λ is the wavelength of the cavity resonant mode. Then Equation 7.2 can be expressed in terms of the shunt impedance per cell,

$$P_{\text{diss}} = \frac{V_{\text{acc}}^2}{(R_{sh}/Q_0)_{\text{cell}}(2L/\lambda)Q_0}. \tag{7.3}$$

Substituting $V_{\text{acc}} = E_{\text{acc}}L$ and $Q_0 = G/R_S$ gives an expression in terms of the accelerating field E_{acc}, the surface resistance R_S, and the geometry factor G,

$$P_{\text{diss}} = \frac{E_{\text{acc}}^2 L^2 R_S}{(R_{sh}/Q_0)_{\text{cell}}(2L/\lambda)G}. \tag{7.4}$$

Simplifying terms, dividing through by a factor of V_{acc}, and writing Equation 7.4 in terms of frequency gives

$$\frac{P_{\text{diss}}}{V_{\text{acc}}} = \frac{cE_{\text{acc}}}{2(R_{sh}/Q_0)_{\text{cell}}G}\left(\frac{R_S}{f}\right). \tag{7.5}$$

The above relation can be put into form useful to accelerator physicists by multiplying through by a factor of $1/e$ where e is the electron charge to obtain the dissipated power per unit beam energy

$$\frac{P_{\text{diss}}}{E_{\text{beam}}} = \frac{cE_{\text{acc}}}{2e(R_{sh}/Q_0)_{\text{cell}}G}\left(\frac{R_S}{f}\right). \tag{7.6}$$

To obtain the dissipated power, the surface resistance must first be known. The form of the surface resistance and its dependencies are discussed in the following section.

7.1.2 Surface Resistance

The surface resistance can be broken down further into the temperature dependent BCS resistance, R_{BCS}, and the temperature independent residual resistance, R_{res}, where, in general, both components will depend on field strength and frequency:

$$R_S(B_{\text{pk}}, f, T) = R_{\text{BCS}}(B_{\text{pk}}, f, T) + R_{\text{res}}(B_{\text{pk}}, f), \tag{7.7}$$

Here B_{pk} is the peak surface magnetic field and is related to E_{acc} by a geometry dependent constant, f is the resonance frequency, and T is the cryogenic bath temperature. The BCS theory predicts that $R_{\text{BCS}} \propto f^2$ for niobium cavities at low fields [MB58, PKH08]. However, the frequency dependence of R_{BCS} at higher fields is not well known and has not been investigated thoroughly. The model discussed in this chapter was created, in part, to investigate the exact frequency dependence of R_{BCS} based on experimental data. In this model, the relation between frequency and R_{BCS} is taken to follow the form

$$R_{\text{BCS}} = A_T f^x \tag{7.8}$$

where $1 \lesssim x \lesssim 2$ and is determined through fitting data of R_{BCS} at fixed temperature and field. The prefactor A_T introduces temperature dependence through

$$A_T = A_0 \left(\frac{1}{T}\right) e^{-\Delta(0)/k_B T} \tag{7.9}$$

where $\Delta(0)$ is the asymptotic value of the energy gap for $T \ll T_c$ and is taken to be independent of field and frequency to a good approximation. The field dependence of A_T and x is obtained numerically through fitting of Equation 7.8 at different fields since, in general, a closed form expression for the field dependence does not exist. In other words, there is currently no complete, established theory that can describe the field dependence of R_{BCS}.

The residual resistance is taken to vary linearly with field, consistent with observations in nitrogen doped, infused, and niobium(III)-tin coated cavities [Gon16b, Hal17, Man20] and with the square root of frequency [Pad09]. The dependence used in this model is given by

$$R_{\mathrm{res}} = (R_0 + R_1 B_{\mathrm{pk}}) f^{1/2} \tag{7.10}$$

where R_0 and R_1 are constants. This form was a convenient choice because of its tunability which allows for the study of the effect of the relative magnitude of R_{BCS} and R_{res} on the optimal cryogenic power.

7.1.3 Cryogenic Power

The theoretical minimum cryogenic power required to maintain a cavity at a helium bath temperature T_{He} with an ambient temperature $T_a = 300$ K is given by the thermodynamic relation for a Carnot refrigerator [PKH08]

$$P_{\mathrm{cryo,theo}} = P_{\mathrm{diss}} \left(\frac{T_a - T_{\mathrm{He}}}{T_{\mathrm{He}}}\right). \tag{7.11}$$

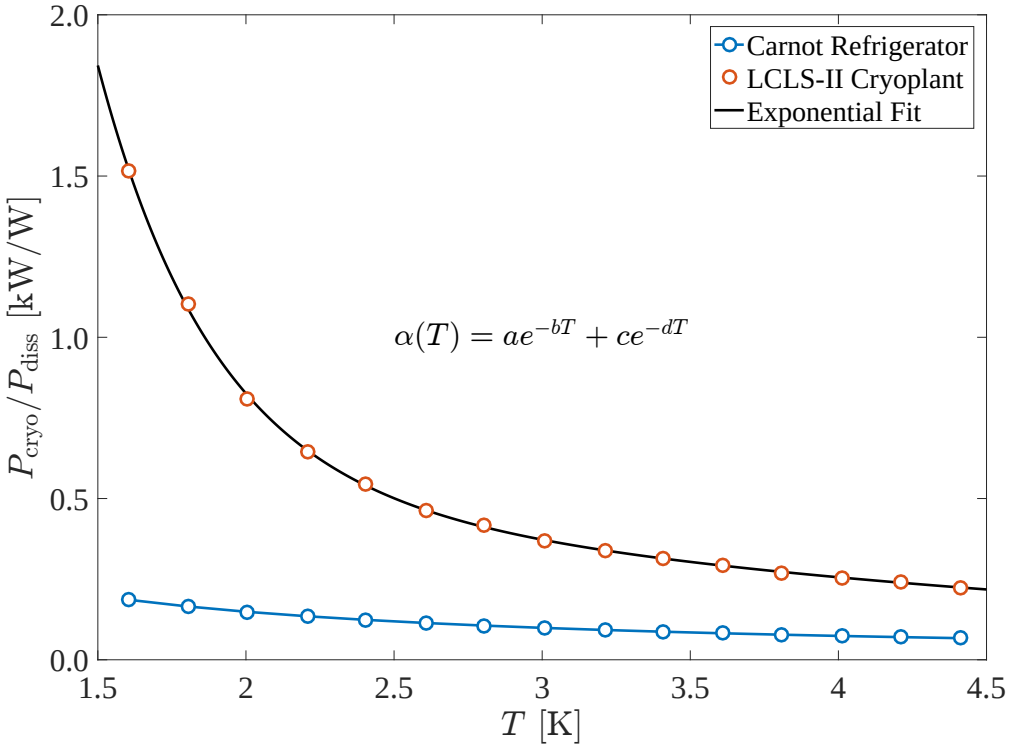

Figure 7.1: Cryogenic efficiency of a cryogenic plant with a double exponential fit used in the model. Data adapted from [Sch03].

The maximum coefficient of performance COP_{max} and the 'real-world' COP are related to the minimum cryogenic power $P_{\text{cryo,theo}}$, 'real-world' cryogenic power P_{cryo}, and the power dissipated by the cavity by

$$\text{COP}_{\text{max}} = \frac{P_{\text{diss}}}{P_{\text{cryo,min}}} = \frac{T_{\text{He}}}{T_a - T_{\text{He}}} \tag{7.12}$$

and

$$\text{COP} = \frac{P_{\text{diss}}}{P_{\text{cryo}}}. \tag{7.13}$$

where $\eta = \text{COP}/\text{COP}_{\text{max}}$ is the Carnot fraction. Finally, the 'real-world' cryogenic power can be calculated from the measured η, the maximum coefficient of performance calculated from Equation 7.12, and the modeled dissipated power from

$$P_{\text{cryo}} = \frac{P_{\text{diss}}}{\eta \text{COP}_{\text{max}}} = \alpha(T_{\text{He}}) P_{\text{diss}}. \tag{7.14}$$

The function $\alpha(T_{\mathrm{He}}) = 1/\eta \mathrm{COP}_{\mathrm{max}}$ is obtained by an exponential fit of the ratio $P_{\mathrm{cryo}}/P_{\mathrm{diss}}$ data obtained from [Sch03]. This data and fitted exponential are shown in Figure 7.1. It is important to note here that $\alpha(T_{\mathrm{He}}) \propto T_{\mathrm{He}}^{-1}$ which comes from $\mathrm{COP}_{\mathrm{max}}$ and the fact that $T_{\mathrm{He}} \ll T_a$.

7.2 Cavity Preparations

The modeling presented throughout the rest of the chapter relies primarily on data from Fermi National Accelerator Laboratory (Fermilab) [Mar18] and some from Cornell. Each cavity preparation shown in Figure 7.3 will be described in this section. All cavities in this chapter had a 100 – 150 μm post-fabrication EP and either a 800 or 900 °C vacuum de-gas bake for 3 – 5 hr followed by additional treatment, if any. The nitrogen doped (N-doped) cavities were doped immediately after the de-gas bake at 800 °C for 2 min (25–40 mTorr N_2) followed by an 800 °C vacuum anneal for 0 – 6 min and a 5 μm post-dope EP [Mar18]. The EP cavities received an additional 40 μm EP after the de-gas bake while the BCP cavities received a 40 – 50 μm post-bake BCP instead [Mar18]. Finally, the EP120 cavities were installed on the test insert and vacuum baked *in-situ* at 120 °C for 48 hr [Mar18].

The results of the model, which will be discussed in the following section, will focus only on the nitrogen-doped and 120 °C cavities for the sake of brevity. These two cavity preparations were chosen because these recipes are used in modern accelerators [Gon18, Sin16] and are of interest to the SRF community.

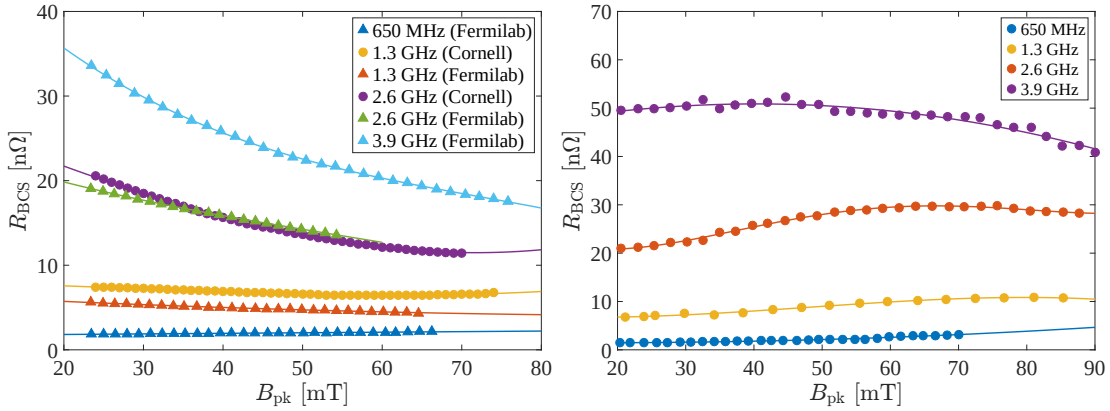

Figure 7.2: The BCS resistance at 2.0 K as a function of peak surface magnetic field for cavities at various frequencies for nitrogen-doped cavities from Fermilab and Cornell (**left**) and the 120 °C vacuum baked cavities from Fermilab (**right**). Data adapted from [Mar18].

7.3 Numerical Methods

The numerical model begins by fitting data of $R_{BCS}(B_{pk})$ at 2.0 K from cavities at different frequencies ranging from 650 MHz to 4 GHz with low-order polynomials up to third order to obtain continuous R_{BCS} curves. The choice of polynomial order for the fit is chosen to best preserve the shape and behavior of the particular curve being fit. An example of such fits are shown in Figure 7.2 for the nitrogen-doped and 120 °C recipes.

Next, the polynomial fits of R_{BCS} vs B_{pk} are fit to the natural logarithm of Equation 7.8 for each value of B_{pk},

$$\ln(R_{BCS}) = \ln\left(A_T(2.0\text{ K})\right) + x\ln(f), \tag{7.15}$$

to obtain the parameters $A_T(2.0\text{ K})$ and x as a function of field. The results of these fits for each recipe are shown in Figure 7.3. The prefactor A_0 is calculated from $A_T(2.0\text{ K})$ and Equation 7.9 with $\Delta(0)/k_bT_c = 2$, $T = 2.0$ K, and $T_c = 9.2$ K. Finally, $A_T(T)$ is calculated from the A_0 values using Equation 7.9 and the same

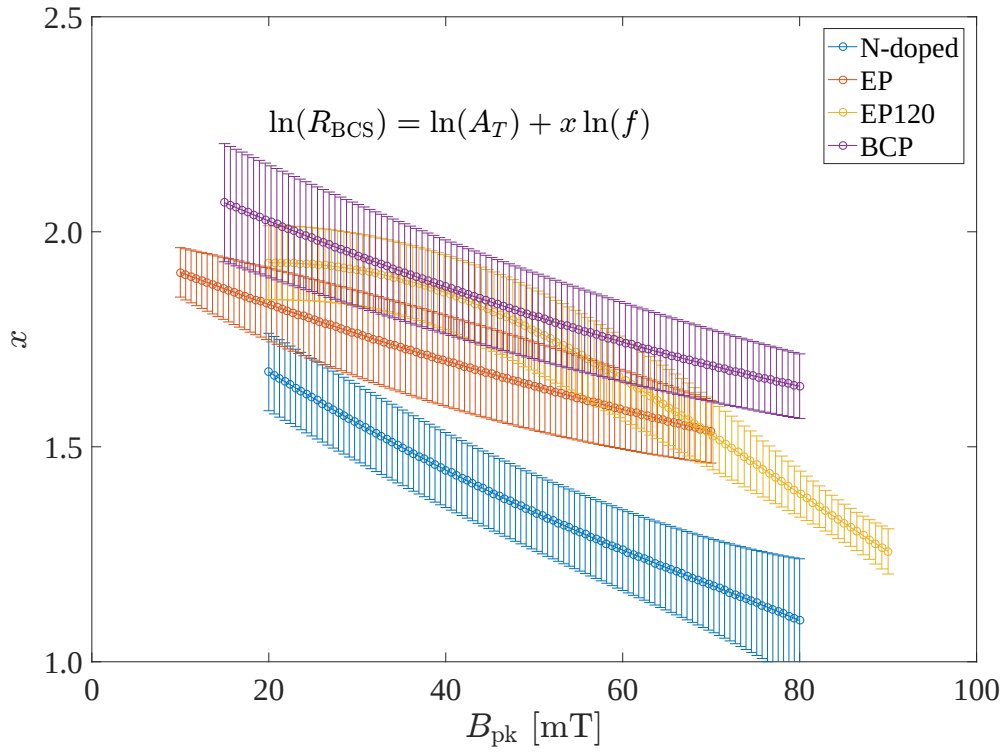

Figure 7.3: The result of the fits of R_{BCS} vs f for the parameter x at fixed B_{pk} for all cavity recipes.

values for $\Delta(0)/k_bT_c$ and T_c.

With all the necessary parameters in hand, R_{BCS} is calculated from Equation 7.8 and R_{res} from Equation 7.10. From these, the dissipated power $P_{\mathrm{diss}}/E_{\mathrm{beam}}$ is obtained from Equation 7.6 and the cryogenic power $p_{\mathrm{cryo}} = P_{\mathrm{cryo}}/E_{\mathrm{beam}}$ from Equation 7.14. Optimization begins with finding the optimal temperature, T_{opt}, that minimizes the cryogenic power as a function of B_{pk} and f. Finally, the optimal frequency, f_{opt}, is obtained as a function of field.

Before continuing on to the results of the model, it is worthwhile to examine the dependence of x with B_{pk}. At low fields, x is either ≈ 2 or is trending towards it for all cavity preparations shown Figure 7.3, as expected from the BCS theory prediction. However, x tends towards unity as the field increases

for all the recipes shown. For instance, for the nitrogen-doped cavities R_{BCS} very nearly varies linearly with f at 80 mT. This is quite remarkable behavior considering the strong deviation from the f^2 that is expected. A similar trend is observed for the 120 °C baked cavities where at high fields the dependence of R_{BCS} trends towards a linear dependence. The trends in the observed in the frequency dependence of R_{BCS} as a function of field could provide guidance for future theoretical models of the frequency dependence of the surface resistance.

7.4 Results

This section will discuss the results of the model for the nitrogen-doped and 120 °C vacuum baked cavities. The optimal temperature and minimum cryogenic power per unit beam energy, referred to as $p_{\mathrm{cryo,min}}$ from this point forward, as a function of field and frequency will be discussed first. Next, the frequency dependence of T_{opt} and $p_{\mathrm{cryo,min}}$ at $B_{\mathrm{pk}} = 68$ mT ($E_{\mathrm{acc}} \approx 16$ MV/m) will be considered. Finally, this section will conclude with a discussion of the field dependence of f_{opt} and $p_{\mathrm{cryo,min}}$.

The range of 20–80 mT for the field was chosen to confine the model to the field limits of the data. For frequency, a range of 1–8 GHz was chosen so that qualitative features of the model could be observed over an ample range while not going to such high frequencies that would correspond to cavities so small as to be unusable in application. The lower and upper limits of 1.7 and 2.1 K were chosen because, historically, niobium cavities were primarily operated in this temperature range. The lower limit was chosen precisely because operating cryogenic plants below 1.7 K is extremely unfeasible.

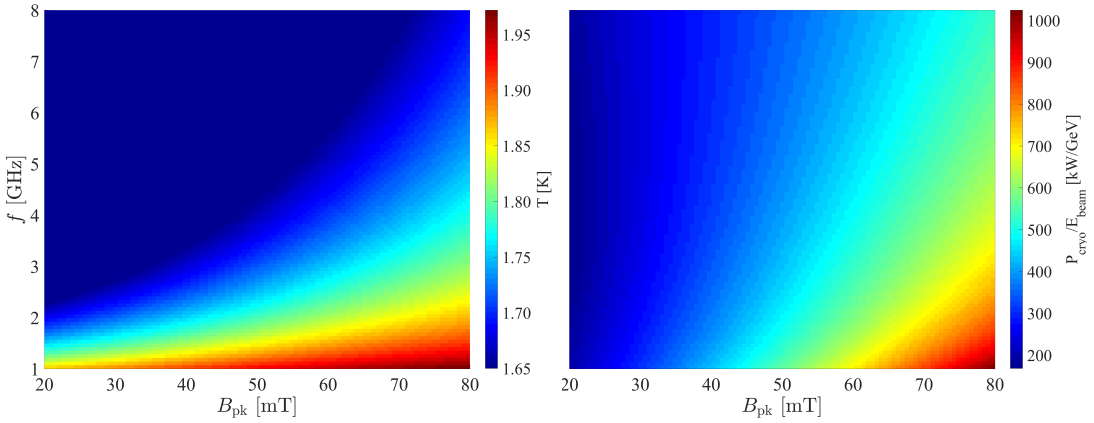

Figure 7.4: The optimal temperature (**left**) and minimum cryogenic power (**right**) as a function of field and frequency for the nitrogen doped cavities. The residual resistance parameters $R_0 = 5\ \mathrm{n\Omega}/\sqrt{\mathrm{GHz}}$ and $R_1 = 50\ \mathrm{n\Omega}/\left(\sqrt{\mathrm{GHz}} \cdot \mathrm{T}\right)$.

The optimal temperature and minimum cryogenic power as a function of field and frequency is shown in Figure 7.4 for the nitrogen doped cavities with residual resistance parameters $R_0 = 5\ \mathrm{n\Omega}/\sqrt{\mathrm{GHz}}$ and $R_1 = 50\ \mathrm{n\Omega}/\left(\sqrt{\mathrm{GHz}} \cdot \mathrm{T}\right)$. It is observed that $p_{\mathrm{cryo,min}}$ increases with field for all frequencies. Qualitatively this makes since $R_{\mathrm{BCS}} \propto B_{\mathrm{pk}}^{-1}$ and $R_{\mathrm{res}} \propto B_{\mathrm{pk}}$ resulting in a proportionality of $p_{\mathrm{cryo}} \propto B_{\mathrm{pk}}^{2}$. Because the residual resistance is temperature independent, the optimal temperature tends to be maximized since $R_{\mathrm{res}} > R_{\mathrm{BCS}}$ at higher fields and $\alpha(T) \propto T^{-1}$. In other words, when the residual resistance dominates, the optimal temperature increases to increase the cryogenic efficiency. The increase in optimal temperature is only weakly damped by the decrease of R_{BCS} with decreasing temperature since $R_{\mathrm{BCS}} < R_{\mathrm{res}}$ at higher fields.

The optimal temperature and cryogenic power generally decrease with increasing frequency except at low fields. The frequency dependence of the cryogenic power is given by $p_{\mathrm{cryo}} \propto c_1 f^{x-1} + c_2 f^{-1/2}$ where c_1 and c_2 are arbitrary constants and the first and second terms in the proportionality are due to R_{BCS} and R_{res}, respectively. As the frequency increase, the BCS term increases and

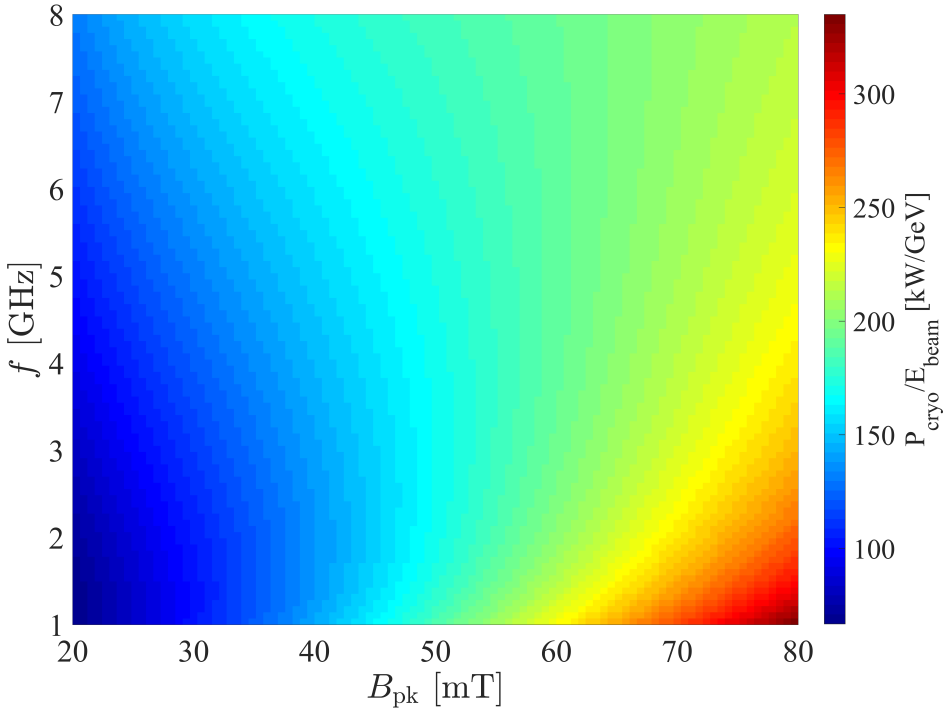

Figure 7.5: The minimum cryogenic power as a function of field and frequency for the nitrogen doped cavities. The residual resistance parameters $R_0 = 1\ \mathrm{n\Omega}/\sqrt{\mathrm{GHz}}$ and $R_1 = 10\ \mathrm{n\Omega}/\left(\sqrt{\mathrm{GHz}} \cdot \mathrm{T}\right)$.

the residual term decreases and, therefore, the optimal temperature decreases to minimize the BCS term. This effect is stronger at lower fields where x is larger causing BCS term to grow more rapidly with frequency. At high fields, the residual term tends to dominate over the BCS term such that $p_{\mathrm{cryo}} \propto c_2 f^{-1/2}$. At lower fields, however, $R_{\mathrm{BCS}} \approx R_{\mathrm{res}}$ which causes a competing effect between the two terms and the cryogenic power varies only weakly with frequency.

It is instructive to also consider the case where $R_{\mathrm{res}} \lesssim R_{\mathrm{BCS}}$. Such a case, with $R_0 = 1\ \mathrm{n\Omega}/\sqrt{\mathrm{GHz}}$ and $R_1 = 10\ \mathrm{n\Omega}/\left(\sqrt{\mathrm{GHz}} \cdot \mathrm{T}\right)$ is shown in Figure 7.5. In this scenario, the the BCS term dominates at low fields causing the cryogenic power to vary as $p_{\mathrm{cryo}} \propto c_1 f^{x-1}$ and, therefore, increase with frequency. At higher fields, the residual term begins to dominate and decreases faster with frequency than

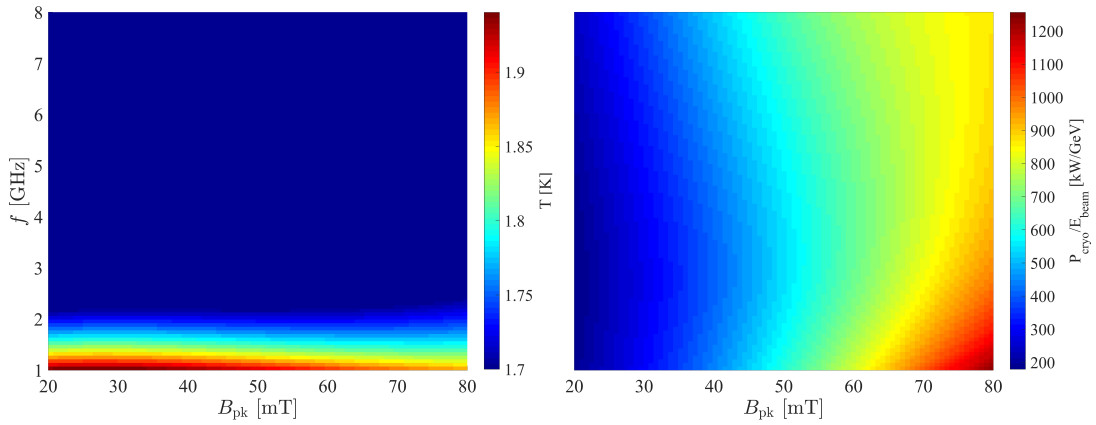

Figure 7.6: The minimum cryogenic power as a function of field and frequency for the 120 °C vacuum baked cavities. The residual resistance parameters $R_0 = 5$ nΩ/ $\sqrt{\text{GHz}}$ and $R_1 = 50$ nΩ/$\left(\sqrt{\text{GHz}} \cdot \text{T}\right)$.

the BCS term increases. Therefore, cryogenic power is mostly dominated by the behavior of the residual term and decreases with frequency as previously observed in the prior case. At moderate fields both terms compete and the power varies more weakly frequency. In this case, the optimal temperature is 1.7 K since $R_{\text{res}} \lesssim R_{\text{BCS}}$ for all fields and frequencies. The rapid increase is offset by decreasing the temperature to minimize the BCS term.

For the 120 °C baked cavities, R_{BCS} varies more weakly with field compared to the nitrogen-doped cavites as can be seen in Figure 7.2. Therefore, the cryogenic power roughly scales as $p_{\text{cryo}} \propto c_1 B_{\text{pk}} + c_2 B_{\text{pk}}^2$ and increases with field for all frequencies. The optimal temperature and minimized cryogenic power for $R_0 = 5$ nΩ/ $\sqrt{\text{GHz}}$ and $R_1 = 50$ nΩ/$\left(\sqrt{\text{GHz}} \cdot \text{T}\right)$ is shown in Figure 7.6. In this case, the cryogenic power is only weakly frequency dependent for $B_{\text{pk}} < 70$ mT because the BCS and residual terms of the frequency dependence are approximately equal. In other words, the BCS term is increasing with frequency at approximately the same rate that the residual term decreases. At higher fields (i.e., $B_{\text{pk}} > 70$ mT), the residual term dominates and, therefore, the power decreases

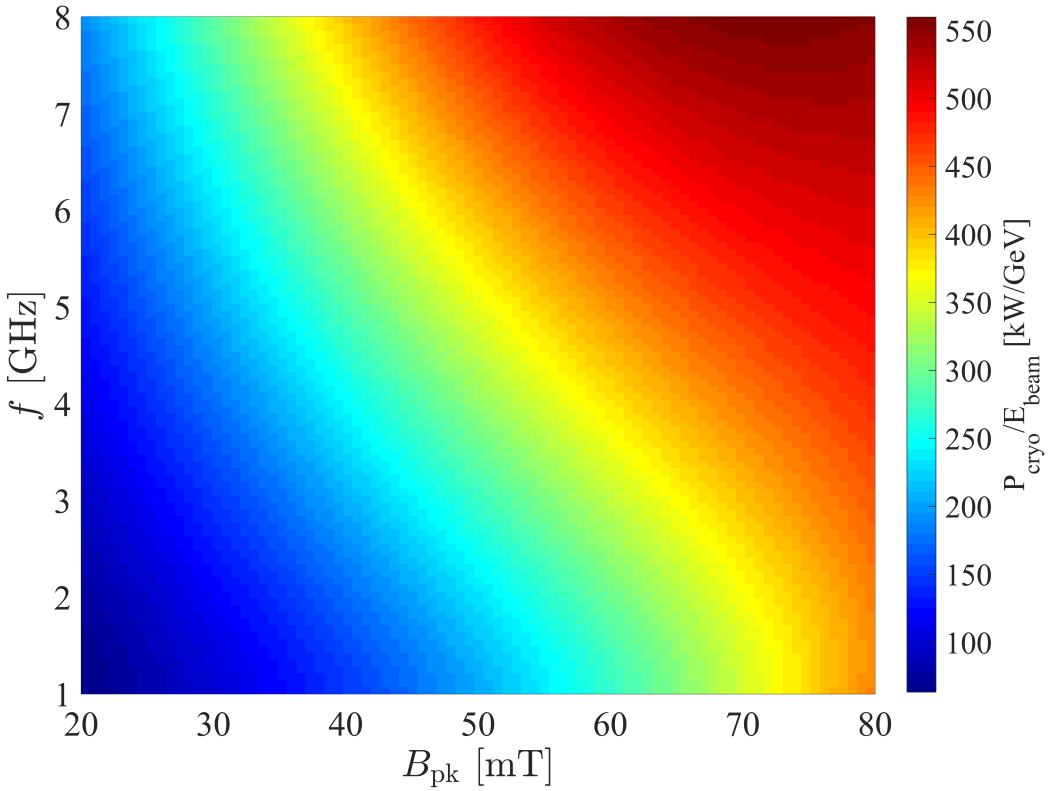

Figure 7.7: The minimum cryogenic power as a function of field and frequency for the 120 °C vacuum baked cavities. The residual resistance parameters $R_0 = 1$ n$\Omega/\sqrt{\text{GHz}}$ and $R_1 = 10$ n$\Omega/\left(\sqrt{\text{GHz}} \cdot \text{T}\right)$.

with increasing frequency. The optimal temperature rapidly decreases to the 1.7 K minimum since x is larger for the 120 °C across all fields and, therefore, the BCS term increases more rapidly with frequency than in the nitrogen-doped case.

Interesting behavior also occurs when the BCS term dominates. Such a case is shown in Figure 7.7 with $R_0 = 1$ n$\Omega/\sqrt{\text{GHz}}$ and $R_1 = 10$ n$\Omega/\left(\sqrt{\text{GHz}} \cdot \text{T}\right)$. Again, the cryogenic power increases with field, as argued previously, for all frequencies. In contrast to the previous case that had a more strongly field dependent residual resistance, the cryogenic power increases with frequency for all fields due to the dominance of the BCS term. Because of this, the optimal

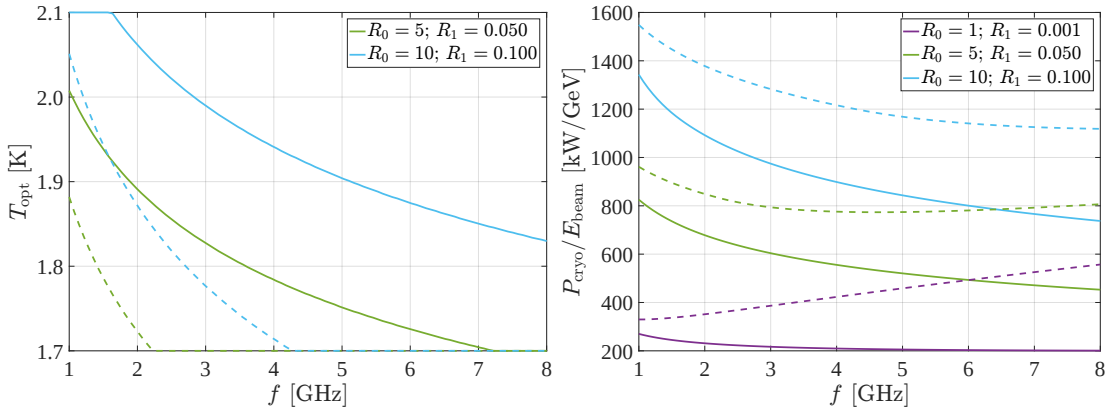

Figure 7.8: The optimal temperature (**left**) and minimum cryogenic power (**right**) as a function of frequency at $B_{\mathrm{pk}} = 68$ mT ($E_{\mathrm{acc}} \approx 16$ MV/m) for the nitrogen doped (solid lines) and 120 °C vacuum baked cavities (dashed lines). The residual resistance parameters R_0 and R_1 are given in units of nΩ/$\sqrt{\mathrm{GHz}}$ and nΩ/$\left(\sqrt{\mathrm{GHz}} \cdot \mathrm{mT}\right)$, respectively.

temperature is forced to the minimum of 1.7 K for all fields and frequencies to minimize the BCS term.

It is worthwhile to discuss the optimal temperature and minimal cryogenic power as a function of frequency at a fixed field. A value of $E_{\mathrm{acc}} = 16$ MV/m ($B_{\mathrm{pk}} \approx 68$ mT) was chosen because this is the specification of the LCLS-II accelerator which, at the time of publication, is in the process of being cooled down for the first time. Both nitrogen-doped and 120 °C recipes are examined for three different field and frequency dependencies of the residual resistance given by three sets of the parameters R_0 and R_1. These results are outlined in Figure 7.8.

For the nitrogen-doped case, the minimized cryogenic power at the optimal temperature decreases with increasing frequency. This is an interesting trend considering the history of superconducting cavities in accelerators. In the past, accelerators were always designed around cavities at ~1 GHz because of the scaling of the surface resistance with frequency and a general lack of preparation methods that could minimize the surface resistance of higher frequency cavities

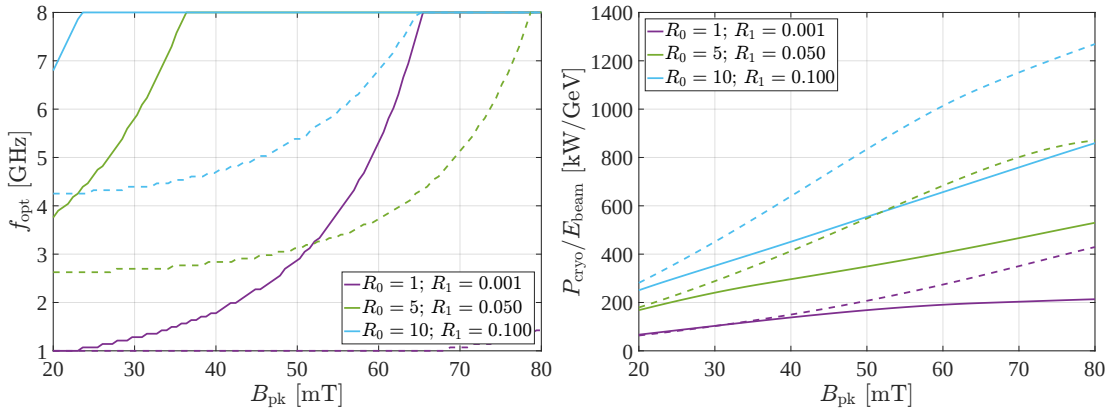

Figure 7.9: **Right:** The frequency that minimizes the cryogenic power, f_{min}, as a function of field. **Left:** The minimum cryogenic power as a function of field at f_{min} for each field value. The solid lines are the nitrogen doped cavities and the dashed lines are the 120 °C vacuum baked cavities. The residual resistance parameters R_0 and R_1 are in units of $\text{n}\Omega/\sqrt{\text{GHz}}$ and $\text{n}\Omega/\left(\sqrt{\text{GHz}}\cdot\text{mT}\right)$, respectively.

enough to be usable at the fields required for the machines. Considering the advances made through nitrogen doping and infusion in the past decade, higher frequency cavities are now viable candidates for future accelerators. Thus, the results of the model actually coincide with these recent advances and strengthen the idea that higher frequency doped or infused cavities could be the key to minimizing the cryogenic power costs of running superconducting accelerators making them more accessible to a wider audience.

On the other hand, for the 120 °C cavities, the outcome depends more so on the relative balance between the BCS and residual resistance. In the case where $R_{\text{BCS}} > R_{\text{res}}$, the cryogenic power increases with frequency whereas in the opposite case it decreases. In the intermediate regime where $R_{\text{BCS}} \approx R_{\text{res}}$, the power is more weakly dependent on frequency. Therefore, if designing an accelerator with this cavity recipe in mind, one must first know what achievable residual resistances can be obtained and their relative strength before choosing an optimal frequency.

For both recipes, the optimal temperature decays with increasing frequency to minimize the BCS term in the cryogenic power. The BCS term for 120 °C baked cavities grow with frequency more quickly than the nitrogen doped cavities since x is larger for the 120 °C cavities and, therefore, the BCS term grows more rapidly.

This section is concluded now with a discussion of the frequency that minimizes the cryogenic power, f_{opt}, and the minimized cryogenic power at f_{opt} and T_{opt} as a function of field. The same field and frequency dependencies for the residual resistance are considered for both the nitrogen doped and 120 °C baked cavities. The results are summarized in Figure 7.9. As can be seen, the optimal frequency increases when the residual resistance is larger. This follows from the $f^{-1/2}$ dependence of the residual term in the cryogenic power. The larger residual terms are minimized at higher frequencies. However, there is also the competition from the BCS term which is minimized at smaller frequencies. This competing behavior results in the observed curves.

The behavior of the minimized cryogenic power at f_{opt} and T_{opt} as a function of field is quite complex and is more difficult to explain using arguments based on proportionality since f_{opt} and T_{opt} are both field dependent. Qualitatively the trends for both cavity recipes and different field and frequency dependencies can generally be explained by the fact that the cryogenic power increases with field for all frequencies. The frequency dependence is more complicated since in some cases the power can decrease or increase with frequency depending on the parameters used for the residual resistance and the field strength. In general, however, for all scenarios considered it appears that the increase in power due to the field dependence mostly overcomes the decrease in the cryogenic power

due to the increase in frequency.

It is quite interesting to see how sensitive the cryogenic power is to even small changes in the residual resistance at high fields. The is of particular interest since, in general, higher accelerating field result in shorter accelerators which have lower capital costs. Consider, for example, the minimum cryogenic power at 80 mT for the best case scenario for the nitrogen-doped cavities ($R_0 = 1\ \mathrm{n\Omega}/\sqrt{\mathrm{GHz}}$ and $R_1 = 10\ \mathrm{n\Omega}/\left(\sqrt{\mathrm{GHz}} \cdot \mathrm{T}\right)$ and worst case scenario ($R_0 = 10\ \mathrm{n\Omega}/\sqrt{\mathrm{GHz}}$ and $R_1 = 100\ \mathrm{n\Omega}/\left(\sqrt{\mathrm{GHz}} \cdot \mathrm{T}\right)$). The cryogenic power quadrupoles implying a four-fold increase in operational cryogenic costs. Thus, it is of great importance to minimize the residual resistance in cavities built for future accelerators.

7.5 Conclusion

In this chapter, a model was proposed to take as inputs experimental data of the field dependence of the BCS resistance for different cavity recipes at multiple frequencies and give as its outputs the optimal temperature and frequencies that minimize the cryogenic power per unit of beam energy as a function of field. The results of the model for nitrogen doped and 120 °C vacuum baked cavities were discussed.

Future work to improve the model could include a more recipe specific model of the residual resistance and also data at higher frequencies for the recipes shown as well as recipes not shown (such as nitrogen infusion). Currently, the field and frequency dependence of the surface resistance for cavities at frequencies above 4 GHz has not been explored. Adding data from frequen-

cies above 4 GHz would improve the model as well as give insight into the frequency threshold at which the field and frequency dependence of the resistance begins to qualitatively change from that currently observed.

It should be also be noted that higher frequency cavities can be disadvantageous compared to lower frequency cavities. For example, higher frequency cavities have much smaller beam tube apertures which can limit transverse beam size and, in turn, achievable beam currents or higher-order mode excitations due to beam-cavity interactions [Wie15]. For these and other reasons, higher frequency cavities may not always be the optimal choice.

CHAPTER 8

CONCLUSION

This dissertation discussed the results of low temperature infusion studies on the field dependence of the surface resistance, the design and commissioning of hardware to test high frequency cavities up to 6 GHz, and a numerical model to optimize the cryogenic power required to cool superconducting cavities as a function of field, frequency, and temperature.

The low temperature infusion studies resulted in several important conclusions. Namely, the anti-Q-slope results from a near surface effect (< 50 nm), the level of the concentration of interstitial impurities matters and if the impurity concentration drops too low the anti-Q-slope disappears, the surface chemistry is important and can 'kill' the anti-Q-slope in certain instances (such as titanium surface contamination), and, perhaps most importantly, that O played the primary role in the appearance of the anti-Q-slope while C played an equal or secondary role and the N played little to no role at all. This last point is of particular significance because it demonstrates that (1) N was not responsible for the anti-Q-slope in infused cavities, and (2) that other impurities such C and O can produce the same effect.

The discussion of the design and commissioning of apparatus demonstrated the expansion of infrastructure to electropolish, high pressure rinse, and test high frequency cavities in the Cornell SRF lab. This new infrastructure can be used for many years to come to test cavities at 3.9 and 5.2 GHz while also being easily adaptable to even higher frequency cavities.

The model created for the optimization of cryogenic power showed that, for

nitrogen-doped cavities, higher frequencies were more optimal than lower frequencies, the optimal cryogenic power is very dependent on the magnitude of the residual resistance, and that optimal frequencies tended to increase with increasing accelerating gradient. These results have strong implications for future accelerators where smaller, higher frequency cavities may be used to reduce capital and operational costs.

BIBLIOGRAPHY

[ABB+00] B. Aune, R. Bandelmann, D. Bloess, B. Bonin, A. Bosotti, M. Champion, C. Crawford, G. Deppe, B. Dwersteg, D. A. Edwards, H. T. Edwards, M. Ferrario, M. Fouaidy, P.-D. Gall, A. Gamp, A. Gössel, J. Graber, D. Hubert, M. Hüning, M. Juillard, T. Junquera, H. Kaiser, G. Kreps, M. Kuchnir, R. Lange, M. Leenen, M. Liepe, L. Lilje, A. Matheisen, W.-D. Möller, A. Mosnier, H. Padamsee, C. Pagani, M. Pekeler, H.-B. Peters, O. Peters, D. Proch, K. Rehlich, D. Reschke, H. Safa, T. Schilcher, P. Schmüser, J. Sekutowicz, S. Simrock, W. Singer, M. Tigner, D. Trines, K. Twarowski, G. Weichert, J. Weisend, J. Wojtkiewicz, S. Wolff, and K. Zapfe. Superconducting TESLA Cavities. *Phys. Rev. ST Accel. Beams*, 3(092001), 2000.

[ATL12] ATLAS Collaboration. Observation of a New Particle in the Search for the Standard Model Higgs Boson with the ATLAS Detector at the LHC. *Phys. Lett. B*, 716(1), 2012.

[BCS57] J. Bardeen, L. N. Cooper, and J. R. Schrieffer. Theory of Superconductivity. *Phys. Rev.*, 108(5), 1957.

[CST] `https://www.3ds.com/products-services/simulia/products/cst-studio-suite/`.

[GL50] V. L. Ginzburg and L. D. Landau. On the Theory of Superconductivity. *Zh. Eksperim. i Teor. Fiz.*, 20(1064), 1950.

[GL14] D. Gonnella and M. Liepe. Cool Down and Flux Trapping Studies on SRF Cavities. In *Proceedings of the 27th International Linear Accelerator Conference*, page 84, Geneva, Switzerland, 2014.

[God06] Godeke, A. A Review of the Properties of Nb_3Sn and Their Variation with A15 Composition, Morphology and Strain State. *Supercond. Sci. Tech.*, 19(8), 2006.

[Gon16a] D. A. Gonnella. *The Fundamental Science of Nitrogen-Doping of Niobium Superconducting Cavities*. PhD thesis, Cornell University, 2016.

[Gon16b] Gonnella, D. and Kaufman, J. and Liepe, M. Impact of Nitrogen Doping of Niobium Superconducting Cavities on the Sensitivity of Surface Resistance to Trapped Magnetic Flux. *J. Appl. Phys.*, 119(073904), 2016.

[Gon18] Gonnella, D. and Aderhold, S. and Burrill, A. and Daly, E. and Davis, K. and Grassellino, A. and Grimm, C. and Khabiboulline, T. and Marhauser, F. and Melnychuk, O. and Palczewski, A. and Posen, S. and Ross, M. and Sergatskov, D. and Sukhanov, A. and Trenikhina, Y. and Wilson, K. M. Industrialization of the Nitrogen-Doping Preparation for SRF Cavities for LCLS-II. *Nucl. Instrum. Methods Phys. Res, A.*, 883(143), 2018.

[Gra17] Grassellino, A. and Romanenko, A. and Trenikhina, Y. and Checchin, M. and Martinello, M. and Melnychuk, O. S. and Chandrasekaran, S. and Sergatskov, D. A. and Posen, S. and Crawford, A. C. and Aderhold, S. and Bice, D. Unprecedented Quality Factors at Accelerating Gradients up to 45 MV/m in Niobium Superconducting Resonators via Low Temperature Nitrogen Infusion. *Supercond. Sci. Tech.*, 30(094004), 2017.

[GRS+13] A. Grassellino, A. Romanenko, D. Sergatskov, O. Melnychuk, Y. Trenikhina, A. Crawford, A. Rowe, M. Wong, T. Khabiboulline, and F. Barkov. Nitrogen and Argon Doping of Niobium for Superconducting Radio Frequency Cavities: A Pathway to Highly Efficient Accelerating Structures. *Supercond. Sci. Tech.*, 26(102001), 2013.

[Gur14] Gurevich, A. Reduction of Dissipative Nonlinear Conductivity of Superconductors by Static and Microwave Magnetic Fields. *Phys. Rev. Lett.*, 13(8), 2014.

[Gur17] A. Gurevich. Theory of RF Superconductivity for Resonant Cavities. *Supercond. Sci. Tech.*, 30(034004), 2017.

[Hal17] D. L. Hall. *New Insights into the Limitations on the Efficiency and Achievable Gradients in Nb_3Sn SRF Cavities*. PhD thesis, Cornell University, 2017.

[Kit05] C. Kittel. *Introduction to Solid State Physics*. John Wiley & Sons, Inc., 8th edition, 2005.

[Kne00] P. Kneisel. Preliminary Experience with In-situ Baking of Niobium Cavities. In *Proceedings of the 9th Workshop on RF Superconductivity*, page 328, Santa Fe, New Mexico, USA, 2000.

[Kou17] Koufalis, P. N. and Hall, D. L. and Liepe, M. and Maniscalco, J. T. Effects of Intersitial Carbon and Oxygen on Niobium Superconducting Cavities, 2017. arXiv:1612.08291.

[Kub19] Kubo, T. and Gurevich, A. Field-Dependent Nonlinear Surface Resistance and its Optimization by Surface Nanostructuring in Superconductors. *Phys. Rev. B*, 100(064522), 2019.

[Lec21] Lechner, E. M. and Angle, J. W. and Stevie, F. A and Kelley, M. J. and Reece, C. E. and Palczewski, A. D. RF Surface Resistance Tuning of Superconducting Niobium via Thermal Diffusion of Native Oxide. *Appl. Phys. Lett.*, 119(082601), 2021.

[Lia17] Liarte, D. B. and Posen, S. and Transtrum, M. and Catelani, G. and Liepe, M. and Sethna, J. P. Theoretical Estimates of Maximum Fields in Superconducting Resonant Radio Frequency Cavities: Stability Theory, Disorder, and Laminates. *Supercond. Sci. Tech.*, 30(033002), 2017.

[LL35] F. London and H. London. The Electromagnetic Equations of the Supraconductor. *Proc. Roy. Soc.*, A149(71), 1935.

[Man20] J. T. Maniscalco. *Studies of the Field-Dependent Surface Resistance of Nitrogen-Doped Niobium For Superconducting Accelerators*. PhD thesis, Cornell University, 2020.

[Mar18] Martinello, M. and Checchin, M. and Romanenko, A. and Grassellino, A. and Aderhold, S. and Chandrasekeran, S. K. and Melnychuk, O. and Posen, S. and Sergatskov, D. A. Field-Enhanced Superconductivity in High-Frequency Niobium Accelerating Cavities. *Phys. Rev. Lett.*, 121(224801), 2018.

[Mat79] R. A. Matula. Electrical Resistivity of Copper, Gold, Palladium, and Silver. *J. Phys. Chem. Ref. Data*, 8(4), 1979.

[MB58] D. C. Mattis and J. Bardeen. Theory of the Anomalous Skin Effect in Normal and Superconducting Metals. *Phys. Rev.*, 111(412), 1958.

[MO33] W. Meissner and R. Ochsenfeld. Ein neuer Effekt bei Eintritt der Supraleitfähigkeit. *Naturwissenschaften*, 21, 1933.

[NM75] V. Novotny and P. P. M. Meincke. Single Superconducting Energy Gap in Pure Niobium. *J. Low. Temp. Phys.*, 18(147), 1975.

[Onn11] H. Kamerlingh Onnes. Further Experiments With Liquid Helium. C. On the Change of Electric Resistance of Pure Metals at Very Low

Temperatures etc. IV. The Resistance of Pure Mercury at Helium Temperatures. *Commun. Phys. Lab. Univ. Leiden*, 120b, 1911.

[Pad09] H. Padamsee. *RF Superconductivity: Science, Technology, and Applitcations*. Wiley-VCH Verlag GmbH & Co, 1st edition, 2009.

[PCC+16] S. Posen, M. Checchin, A. C. Crawford, A. Grassellino, M. Martinello, O. Melychuk, A. Romanenko, D. A. Sergatskov, and Y. Trenikhina. Magnetic Flux Expulsion Studies in Niobium SRF Cavities. In *Proceedings of the 7th International Particle Accelerator Conference*, page 2277, Busan, South Korea, 2016.

[Pip53] A. B. Pippard. An Experimental and Theoretical Study of the Relation Between Magnetic Field and Current in a Superconductor. *Proc. Roy. Soc.*, A216(547), 1953.

[PKH08] H. Padamsee, J. Knobloch, and T. Hays. *RF Superconductivity for Accelerators*. John Wiley & Sons, Inc., 2nd edition, 2008.

[Por21] R. D. Porter. *Advancing the Maximum Accelerating Gradient of Niobium-3-Tin Superconducting Radio Frequency Accelerator Cavities: RF Measurements, Dynamic Temperature Mapping, and Material Growth*. PhD thesis, Cornell University, 2021.

[Poz12] D. M. Pozar. *Microwave Engineering*. John Wiley & Sons, Inc., 4th edition, 2012.

[Sch03] Schneider, W. J. and Kneisel, P. and Rode, C. H. Gradient Optimization for SC CW Accelerators. In *Proceedings of the 2003 Particle Accelerator Conference*, page 2863, Santa Fe, New Mexico, USA, 2003.

[Sin16] Singer, W. and Brinkmann, A. and Iversen, J. and Matheisen, A. and Moeller, W.-D. and Navitski, A. and Reschke, D. and Schaffran, J. and Sulimov, A. and Walker, N. and Weise, H. Production of Superconducting 1.3 GHz Cavities for the European X-ray Free Electron Laser. *Phys. Rev. Accel. Beams*, 19(092001), 2016.

[THS91] J. P. Turneaure, J. Halbritter, and H. A. Schwettman. The Surface Impedance of Superconductors and Normal Conductors: The Mattis-Bardeen Theory. *J. Supercond.*, 4(5), 1991.

[Tin96] M. Tinkham. *Introduction to Superconductivity*. McGraw-Hill, Inc., 2nd edition, 1996.

[VCC98] B. Visentin, J. P. Charrier, and B. Coadou. Improvements of Superconducting Cavity Performances at High Accelerating Gradients. In *Proceedings of the 6th European Particle Accelerator Conference*, page 1885, Stockholm, Sweden, 1998.

[Wan08] T. P. Wangler. *RF Linear Accelerators*. Wiley-VCH Verlag GmbH & Co, 2nd edition, 2008.

[Wie15] H. Wiedemann. *Particle Accelerator Physics*. Spinger, 4th edition, 2015.

[YZQ19] T. Z. Yuan, Z. J. Zhan, and C. N. Qian. New Frontiers in Proton Therapy: Applications in Cancers. *Cancer Commun. (London)*, 39(1), 2019.